Morphogenetic and Regulatory Mechanisms during Developmental Chondrogenesis: New Paradigms for Cartilage Tissue Engineering

Lluís Quintana, M.S.,[1] Nicole I. zur Nieden, Ph.D.,[2] and Carlos E. Semino, Ph.D.[1,3,4]

Cartilage is the first skeletal tissue to be formed during embryogenesis leading to the creation of all mature cartilages and bones, with the exception of the flat bones in the skull. Therefore, errors occurring during the process of chondrogenesis, the formation of cartilage, often lead to severe skeletal malformations such as dysplasias. There are hundreds of skeletal dysplasias, and the molecular genetic etiology of some remains more elusive than of others. Many efforts have aimed at understanding the morphogenetic event of chondrogenesis in normal individuals, of which the main morphogenetic and regulatory mechanisms will be reviewed here. For instance, many signaling molecules that guide chondrogenesis—for example, transforming growth factor-β, bone morphogenetic proteins, fibroblast growth factors, and Wnts, as well as transcriptional regulators such as the Sox family—have already been identified. Moreover, extracellular matrix components also play an important role in this developmental event, as evidenced by the promotion of the chondrogenic potential of chondroprogenitor cells caused by collagen II and proteoglycans like versican. The growing evidence of the elements that control chondrogenesis and the increasing number of different sources of progenitor cells will, hopefully, help to create tissue engineering platforms that could overcome many developmental or degenerative diseases associated with cartilage defects.

Introduction

MATURE CARTILAGE DEVELOPS from the mesodermal lineage and has multiple functions in adult organisms such as articulation capacity in joints or elastic and loading capacity in intervertebral discs. During embryogenesis, chondrogenic precursors play a key role in the formation of the two mature skeletal tissues in long bones: bone and adult cartilage.[1] Long bone formation is achieved through a sequence of events called endochondral ossification initiated from mesenchymal condensations. Briefly, this developmental progression involves the formation of cartilage tissue by mesenchymal cell (MC) differentiation and the subsequent replacement of the cartilage tissue by bone[2] and is tightly controlled by regulation of gene expression and cell–cell and cell–extracellular matrix (ECM) interactions.[3]

These regulatory events conduct a set of morphogenetic and phenotypic changes to the MC within the embryonic mesoderm, giving rise to a preskeletal tissue composed mainly of chondroblasts. Here, chondrogenesis is defined as the process through which the MCs differentiate into chondroblasts that subsequently either develop into adult chondrocytes or undergo hypertrophy and apoptosis.[4] In endochondral ossification, a part of this embryonic cartilage subsequently turns into bone.[5]

Endochondral ossification can be divided into five main stages (Fig. 1). These stages are clearly defined by specific events:

(A) Commitment of MCs to become cartilage caused by paracrine factors, such as fibroblast growth factor (FGF) and Hedgehog pathways.

(B) Differentiation of the condensed MCs into chondrocytes in the process of which the transcription factor Sox9 plays an essential role in controlling the expression of downstream genes specific for cartilage tissue development.

(C) Rapid division of chondrocytes and production of the cartilage-specific ECM.

(D) Halted proliferation of chondrocytes and a several fold increase in size entering hypertrophy. The composition of the ECM (mainly collagen type X and

[1]Tissue Engineering Division, Department of Bioengineering, IQS–Ramon Llull University, Barcelona, Spain.
[2]Molecular & Genetic Toxicology, Bayer HealthCare AG, Wuppertal, Germany.
[3]Center for Biomedical Engineering, Massachusetts Institute of Technology, Boston, Massachusetts.
[4]Translational Centre for Regenerative Medicine, Leipzig University, Leipzig, Germany.
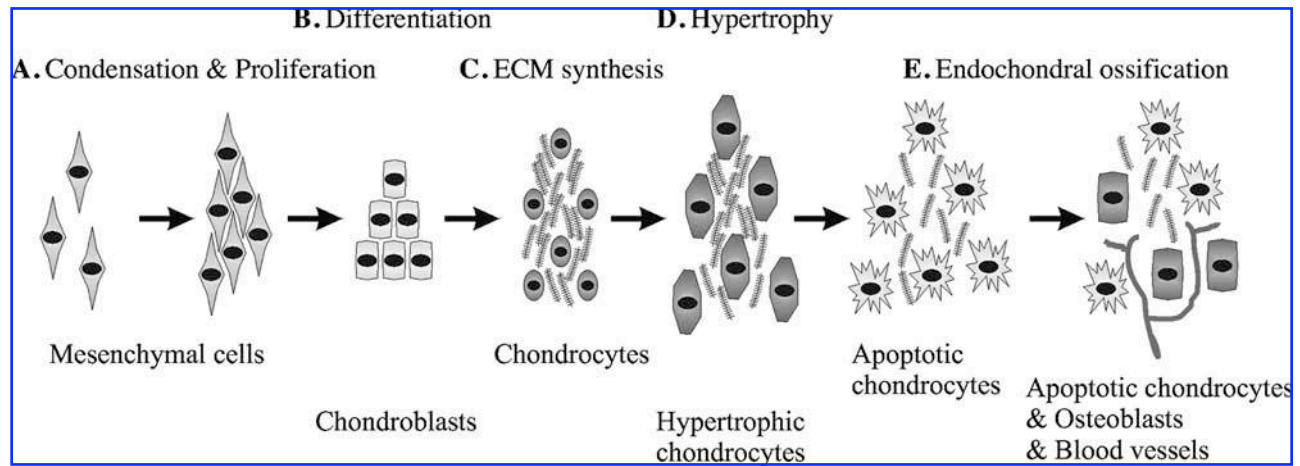
FIG. 1. Schematic representation of the chondrogenesis and endochondral ossification. (**A**) First MCs condense to form a dense cell mass. (**B**) MCs proliferate and differentiate into chondroblasts. (**C**) These cells start secreting cartilage ECM and become mature chondrocytes. (**D**) Eventually, chondrocytes grow to become hypertrophic, and if the tissue undergoes endochondral ossification, (**E**) cartilage is vascularized, ECM is degraded, hypertrophic chondrocytes become apoptotic, and osteoblasts invade the free space within the tissue.

       fibronectin) is also changed, and chondrocytes start to mineralize the environment with calcium salts.
(E) Invasion of blood vessels takes place, and the hypertrophic chondrocytes die by apoptosis. At this stage, osteoblast precursors invade the remodeling tissue and start forming bone using the cartilaginous matrix as template and replacing it by mineralized matrix.

In this review, we will focus on the morphogenetic changes, the regulatory mechanisms, and the interactions that take place during developmental chondrogenesis. In this context, a precise knowledge on the extrinsic factors (environmental) and intrinsic factors (genetic regulation) controlling chondrogenesis can be easily translated into tissue engineering research to obtain more reliable therapeutic products. Therefore, we will place special emphasis on the importance of the ECM during the development of cartilage and its biomechanical function to help recreate similar processes during the development of regenerative platforms. Moreover, we will also summarize recent descriptions of chondroblastic progenitors that are expected to mimic natural chondrogenesis and might play a key role in biomedical research in the near future. Finally, we will discuss some of the novel biomaterials and its applications currently used for cartilage and, eventually, bone repair.

Morphogenetic Changes Associated with Chondrogenesis

    Natural chondrogenesis of the different skeletal structures begins at different time points during embryonic development, but all chondrogenic events share the same cellular origin, the MCs. These MCs may arise from three different sources: (1) neural crest cells of the neural ectoderm that eventually form the craniofacial bones; (2) the sclerotome of the paraxial mesoderm, which gives rise to the axial skeleton; and (3) the somatopleure of the lateral plate mesoderm, which yields the skeleton of the long bones.[6] Under the proper signaling, these MCs begin a physical compaction called mesenchymal condensation, which begins with the

MC increasing their cellular interaction established both with the ECM and with the surrounding cells (Fig. 1A). Specifically, N-cadherin and neural cell adhesion molecule (N-CAM)–mediated cell–cell interactions are of outermost importance during mesenchymal condensation.[7]

    When the cells aggregate, MCs begin to produce collagen I, fibronectin, and proteoglycans.[8] The result of the strong interactions that cells establish with their environment is the formation of a dense mass of MCs that immediately begins to differentiate into chondroblasts (Fig. 1B). Condensed MCs start expressing mainly the transcription factor Sox9 that controls downstream genes involved in chondrogenesis, promoting these progenitor cells to secrete cartilage-specific ECM molecules (Fig. 1C).[9–12]

    The tissue then undergoes a series of morphological and physical changes during maturation, including an increase in rigidity to acquire its typical cartilage stiffness due mainly to ECM components. Moreover, if cartilage turns into bone, chondrocytes increase in size turning into hypertrophic chondrocytes and enriching the ECM mainly with collagen X (Fig. 1D).[10] Afterward, ECM is progressively degraded, and hypertrophic chondrocytes undergo apoptosis generating spaces used by blood vessels to invade the cartilage (Fig. 1E). Simultaneously, osteoblast progenitors use the blood stream to enter this vascularized tissue. The progressive death of chondrocytes and degradation of cartilage collagens and proteoglycans is synchronized with the synthesis of bone ECM and the proliferation of the osteoblast population within the tissue. In addition to this endochondral ossification that requires a cartilaginous intermediate, there is a second type of bone formation called intramembranous ossification that does not require the transitional step of chondrogenesis. This direct osteogenic process consists of the conversion of MCs into bone tissue (reviewed in Franz-Odendaal et al.[13]). Intramembranous ossification is the characteristic way in which flat bones of the skull develop. During this process, neural crest–derived MCs (NCMCs) proliferate and condense forming aggregates where some of the cells form capillaries and other differentiate into

osteoblasts that secrete a collagen–proteoglycan matrix that is able to promote calcium salt deposition.[14]

Finally, it has been noted above that expression of proteoglycans is not exclusive of the synthesis of ECM in mature cartilage formation, but is also important during mesenchymal condensation. For instance, versican, a chondroitin sulfate proteoglycan, has recently been shown to be crucial in mesenchymal condensation to the extent that the absence of the active form of this proteoglycan disrupts subsequent chondrogenesis.[15]

Onset of Chondrogenesis: Transcription Factor Sox9 and Genes Related to Its Regulation

Cartilage formation is the first step in the development of almost all skeletal elements in mammal organisms and presents two independent ontogenetic origins. As stated above, craniofacial cartilage proceeds mainly from NCMCs, while other cartilages come from MCs of mesodermal origin.[16,17] Although these origins are significantly different from each other, transition of the MC to mature cartilage or bone is very similar in both cases.

As we mentioned above, one of the first steps in chondrogenesis is the mesenchymal condensation first mediated by paracrine factors and subsequently by Sox9, a transcrip-

tion factor that belongs to the SRY family and contains the high mobility group box (HMG-box) DNA binding domain.[18] The expression of Sox9 is regulated by members of the FGF, transforming growth factor-β (TGF-β), bone morphogenetic protein (BMP), and Wnt families (Fig. 2).[8,19] The key role of the transcription factor Sox9 in skeletal development is evidenced by its tight regulation and by the fact that abnormal expression of Sox9 leads to severe skeletal disorders like campomelic dysplasia. Sox9 is responsible for the expression of some of the key genes in chondrogenesis: *Sox5*, *Sox6*, and collagen II α1 (*Col2a1*) (Fig. 2). Moreover, Sox9 regulates expression of collagen XI α2 (*Col11a2*) and CD-RAP (cartilage-derived retinoic acid-sensitive protein) before matrix deposition in the cartilage anlagen.[20–22] L-Sox5 and Sox6 in turn are required for the expression of collagen IX α1 (*Col9a1*) and aggrecan, which is the most abundant proteoglycan in cartilage (Fig. 2).[23] Moreover, Akiyama *et al.* have proven that all osteo-chondroprogenitors stem from Sox9-expressing cells, confirming the principal role of Sox9 in chondrogenesis.[24]

In the interdigital region of developing limbs, it is TGF-β that induces the expression of Sox9. This induction is a quick process as the upregulation of Sox9 has been proven to happen only 30 min after exposure of chicken limb bud cells to TGF-β.[19] Apart from regulating the expression of Sox9, TGF-β ultimately initiates the expression of cartilage oligomeric
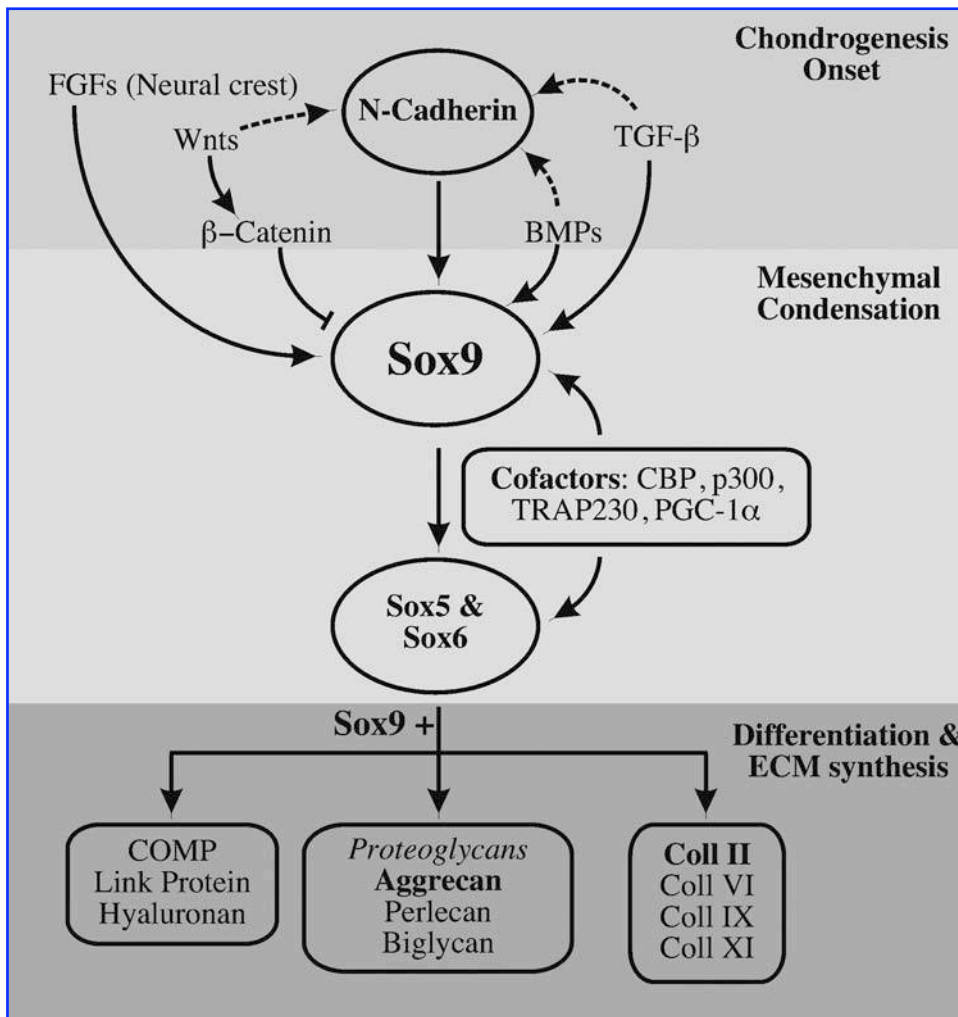

FIG. 2. Upstream and downstream regulation of Sox9. Chondrogenesis begins with the upregulation of N-cadherin and Sox9 by paracrine factors like TGF-β, FGFs, or BMPs, while Wnts downregulate the expression of Sox9. Expression of N-cadherins and Sox9 is accompanied by the condensation and proliferation of MCs, a process called mesenchymal condensation. Sox9 activates the expression of Sox5 and Sox6, and with them and the help of cofactors such as CBP, induces the MC to differentiate into chondroblasts after the condensation. Chondroblasts produce cartilage-specific ECM, including collagen II, IV, IX, and XI; proteoglycans such as aggrecan; and also link proteins and COMP.

matrix protein (COMP), aggrecan, N-cadherin, N-CAM, Coll II, Coll XI, fibronectin, and tenascin.[25] The strong chondrogenic effect of TGF-β is commonly used to induce chondrogenic commitment of mesenchymal stem cells (MSCs) *in vitro*, which will be discussed below.[26,27]

BMPs are another family of the TGF-β superfamily of growth factors that mediate important events within skeletogenesis and body patterning. BMPs induce and maintain the expression of the Hox genes *Msx-1* and *Msx-2*, which are key regulators in antero-posterior limb signaling.[28] Further, BMP-4 and BMP-7 are responsible for specification of neural plate cells to neural crest–derived cells.[29,30] In addition, the expression of Sox9 is dependent on BMP signaling via the BMP receptors 1RA and 1RB (Fig. 2).[31] Apart from these early patterning functions, BMPs are also related to the proliferation and maturation of chondrocytes.[32] Gene knockout experiments with mice have demonstrated that BMP-4 promotes the expression of the cartilage-specific (α2) collagen XI, and that BMP receptors promote the synthesis of collagen I, a type of collagen present in the ECM of MSCs throughout most of the chondrogenesis.[33]

There is considerable crosstalk between the TGF and BMP signaling pathways, which is evidenced by a synergistic effect of TGF-β and BMP-2 on collagen X α1 (*Col10a1*) and an additive effect on Col2a1 mRNA expression.[34] Activation of both pathways simultaneously seems to promote chondrogenic maturation. In summary, the members of the TGF-β superfamily (TGF-β and BMPs) promote very early events in chondrogenesis and, directly or indirectly, maintain their regulation during the differentiation and maturation of chondrocytes.

During the development of the craniofacial skeletal structure, maturation of the neural crest cells is also initiated with the expression of Sox9, as happens in all other skeletal tissues laid down through endochondral ossification. However, in craniofacial bone development, expression of Sox9 can be activated by TGF-β–related growth factors and FGFs. The TGF-β superfamily is more commonly responsible for activation of Sox9, but in certain areas like the posterior facial suture, Sox9 is under the control of FGF-2, FGF-3, FGF-8, and its receptors.[35] Further, the FGF family of growth factors is important for the proliferation and survival of cranial neural crest–derived cells.[35] Apart from being involved in the craniofacial skeletogenesis, FGFs are very important patterning growth factors in limb development and regeneration. FGF-8, FGF-4, and FGF-10 have been identified as important factors for the formation and maintenance of the apical epidermal ridge, a structure that directs proximo-distal development of limbs.[36,37]

Finally, the Wnt family of signaling molecules is also involved in chondrogenesis (Fig. 2). Wnt proteins are distinguished by their capability to activate β-catenin into canonical Wnts (i.e., Wnt3a) and noncanonical Wnts (i.e., Wnt5a). The influence of Wnts on chondrogenesis is twofold and time dependent: at low levels Wnts promote chondroprogenitor differentiation, specifically through modulating Sox9 expression, and later at high levels they promote chondrocyte hypertrophy and subsequent endochondral ossification.[38,39] CatnB controls the chondrogenic commitment of chondroprogenitors by negatively regulating Sox9 expression in particular through competing with Sox9 for the CatnB cofactor TCF, (T-cell factor) and upregulation of Wnt4.[40,41] Because CatnB is a mutual antagonist of Sox9,[19]

noncanonical Wnts, such as Wnt5a, promote early chondrogenesis *in vitro* while inhibiting terminal differentiation *in vivo*.[42] Specifically, Wnt5a misexpression delays the maturation of chondrocytes, while Wnt4 misexpression accelerates this process.[41] Further, Wnts also regulate the expression of N-cadherin, an important cell–cell adhesion protein that is directly involved in mesenchymal condensation.[43]

Fine regulation of Sox9—more specifically, the balance between Sox9 and the osteogenic transcription factor Runx2/ Cbfa1—is what drives osteo-chondroprogenitors to chondroblasts or osteoblasts. For instance, BMP-induced Smad1 and interactions between Smad1 and Runx2 regulate the transition of chondrocytes into hypertrophy[44–46] as evidenced in Runx2-deficient mice, in which the late stages of chondrocyte hypertrophy are blocked.[47,48] The expression patterns of TGF-β–related proteins, FGFs, and Wnts are responsible for regulating the balance between Sox9 and Runx2 and, therefore, the patterning of the skeletal tissue.

Events Happening after the Expression of Sox9

The expression of Sox9 is the first step toward chondrogenesis, for it induces MCs to become osteo-chondroprogenitors during mesenchymal condensation. After these events, two other Sox transcription factors, Sox5 and Sox6, are upregulated. Sox9 is required for the expression of Sox5 and Sox6, and these three Sox transcription factors (the Sox trio) are then expressed until chondrocytes enter hypertrophy.[18] The Sox trio regulates many important events throughout chondrogenesis, thanks to the different spatiotemporal expression of the transcriptional cofactors (CBP [CREB binding protein], p300, TRAP230, PGC-1α, and TCF) that bind to the Sox proteins (Fig. 2). Other members of the *Sox* genes, like *Sox10* in skull development, can also be involved in chondrogenesis, but they are less frequent.[29]

Members of the Sox family of transcription factors directly or indirectly rule the complexity and richness of the cartilaginous ECM. ECM molecules like collagens, COMP, or proteoglycans are only synthesized after the expression of Sox transcription factors, but few of the regulatory mechanisms are understood to date. One of them is the control of the expression of *Col2a1*, the gene encoding collagen II, which is regulated by Sox9, Sox5, and Sox10 in avian neural crest cells.[49] Other studies also show that Sox9 stimulates the synthesis of collagen II,[19,50,51] collagen IX,[52] and collagen XI proteins.[53] Finally, the synthesis of COMP is also regulated by the Sox trio.[54]

After the ECM of cartilage is synthesized, eventually chondrocytes enter hypertrophy to render either into a calcified cartilage tissue or into bone, via endochondral ossification as described above. Hypertrophy is enhanced by the thyroid hormone triiodothyronine,[55] but its regulation relies on Indian Hedgehog/parathyroid hormone–related protein (Ihh/PTHrP) signaling. These two proteins create negative feedback gradients that control the fate and proliferation of prehypertrophic and hypertrophic chondrocytes within the cartilage.[56] On the other hand, Sox9 inhibits chondrocytic hypertrophy, explaining why Sox9 and PTHrP regulate each other.[57,58]

ECM Influence on Mesenchymal Condensation

The tightly regulated transition of MCs to chondrocytes involves not only the time and space–dependent expression

of transcription factors, but also cell–cell and cell–matrix interactions. Cells interact with the ECM or with other cells using membrane receptors or different types of adhesion molecules, and these recognitions translate into intracellular signals affecting gene expression, cell proliferation, and migration.

During the mesenchymal condensation and differentiation, cell–matrix and cell–cell contacts have special significance. For instance, many approaches have shown that N-cadherin–mediated cell–cell interactions play a very important role in mesenchymal condensation.[7] Activation of N-cadherin is important for the expression of many chondrogenic markers like Sox9, Sox6, Sox5, aggrecan, and collagen II.[59] Nevertheless, chondrogenesis is also possible in N-cadherin–deficient limbs, thanks to other cadherins, for example, cadherin-11.[60] In any case, cadherins and cell–cell contact are necessary for the condensation of MCs. Therefore, the expression of N-cadherin is regulated by similar mechanisms to those controlling Sox9: TGF-β, BMP-2, and different Wnts influence in the overall N-cadherin expression.[43,61]

Cell–matrix interactions play an important role in establishing the mechanical strength necessary to pull the MC together in a condensed cell mass. Cells condense and subsequently migrate out from the condensation areas, which requires substantial ECM remodeling. Thus, it is not surprising that the ECM is tightly regulated throughout chondrogenesis to meet the specific mechanical needs in each step of this morphogenetic process. Before the onset of chondrogenesis, MCs are surrounded by an ECM rich in hyaluronan and collagen I.[8,62] First of all, during mesenchymal condensation, the ECM is partially degraded to enhance cell mobility and cell–cell interactions. The concentration of hyaluronan in the ECM drops at this initial step.[62] Moreover, matrix metalloproteinases (MMPs) are upregulated to reduce the protein content of the ECM.[63] Although collagen I is detected along all the mesenchymal condensation,[11] MMPs reduce the presence of structural proteins like collagen I. These changes in the protein and polysaccharide content soften the ECM and facilitate a more intimate cell–cell contact that is critical for the mesenchymal condensation to occur. The different MMPs seem to have different roles in chondrogenic development that are dependent on the developmental stage of the chondrocyte. In particular, MMP1 and MMP2 have the capacity to degrade cartilage matrix, and they are characterized as the MMPs that are involved in earlier chondrogenesis. Specifically, blockage of MMP2 function supports precartilage condensation and chondrogenesis,[64] and MMP1 knockout mice show decreased chondrocyte proliferation in the proliferative zone of the growth plates of long bones.[65] In contrast, MMP13 appears to be one of the most important MMPs in late-stage chondrogenesis in terms of cartilage remodeling and mineralization because it is characterized by a substrate specificity for collagen II, the cartilage-specific collagen.[66] Specifically, MMP13 seems to make the space for cell enlargement that goes hand in hand with hypertrophy by degradation of the cartilage matrix.

Finally, mesenchymal condensation is also affected by small proteoglycans such as versican, perlecan, or syndecan. Versican is a chondroitin sulfate proteoglycan that enhances mesenchymal condensation,[15] but the mechanism by which versican is able to trigger cellular aggregation is not fully understood. Versican can bind many structures that are present in the ECM of precartilage MCs such as fibronectin, collagen I, hyaluronan, or tenascin, and it has been shown that versican is necessary for chondrogenic gene expression.[15] Similarly, perlecan is present in very early stages of chondrogenesis (day 12.5 of gestation) during mouse embryo development, and is also capable of inducing cell aggregation, condensation, and chondrogenic differentiation of C3H10T1/2 fibroblasts *in vitro*.[67] Perlecan is a heparan sulfate proteoglycan that is known to bind other ECM molecules and basement membrane proteins, such as laminin and collagen IV, as well as growth factors, such as FGFs, especially FGF-2 or FGF-9,[68] and BMPs like BMP-2, -4, and -6.[69–71] All the interactions established by perlecan explain the importance of this proteoglycan within chondrogenesis, as shown in perlecan-deficient mouse experiments.[72] Especially strong expression of perlecan is observed in the prehypertrophic and hypertrophic zones,[72] but the exact mechanism by which perlecan regulates mesenchymal condensation and chondrogenesis remains elusive.

Finally, syndecans are transmembrane heparan sulfate proteoglycans that have different isoforms and are reported to be involved in cancers, wound healing, angiogenesis, and chondrogenesis.[73] Syndecan-3 is present in tissues undergoing chondrogenesis and shares with perlecan many binding affinities, such as BMP-2.[74]

In summary, ECM greatly affects mesenchymal condensation in two different ways: it establishes the adequate mechanical environment and moreover modulates the concentration or activity of important growth factors like BMPs or FGFs. This complex and important role of the ECM during mesenchymal condensation still remains unclear and needs further investigation.

Evolution of the ECM during Cartilage Maturation

Mature cartilage is a tissue with an ECM composed of collagenous and noncollagenous elements. The exact composition of the matrix depends on the type of cartilage, but they all share that collagen II is the main collagenous element (about 90% of the collagenous fraction) within the cartilage.[75] Collagens I, VI, IX, X, and XI are also present in the collagen fibrils with different percentages depending on the particular cartilage.[8] The noncollagenous fraction of the cartilage is basically composed of proteoglycans, hyaluronan, link protein, and interfibrillar proteins like COMP or decorin. Proteoglycans are important components of the noncollagenous cartilage matrix because they are responsible for the mechanical properties of cartilage. Aggrecan accounts for about 90% of the proteoglycan content, and the rest contains decorin, fibromodulin, lumican, biglycan, and perlecan. All the collagenous and noncollagenous components together form an interconnected elastic network surrounding chondrocytes in mature cartilaginous tissues[76] accounting for its unique rigidity and flexibility.

The complexity of the ECM of cartilage arises after the mesenchymal condensation, when cells activate all the chondrogenic machinery and gradually transform the ECM into that of a mature cartilage. Collagen I gradually disappears and is substituted by collagen II, VI, IX, and XI. Collagen II is, by far, the most abundant, and its synthesis is regulated by three members of the Sox family of transcription factors, Sox9, Sox6, and Sox5.[77] More interesting is that collagens I

and II can induce chondrogenesis in bone marrow–derived MSCs, which suggests that ECM molecules also regulate gene expression.[78] Collagen X is expressed later on, when chondrocytes acquire the hypertrophic phenotype, and either form calcified cartilage or enter endochondral ossification to become bone tissue.

The short proteoglycans that are present in the mesenchymal condensation (versican, perlecan, or syndecan-3) are gradually substituted by larger and more complex proteoglycans, mainly aggrecan.[15] Link protein, COMP, and all other components of the cartilage ECM are also synthesized to obtain mature cartilage. The regulatory mechanisms that control the synthesis of the noncollagenous elements of the cartilage remain unknown, but are probably dependent on the expression of Sox9.

Finally, if mature cartilage is to become bone or calcified cartilage, chondrocytes acquire the hypertrophic phenotype and express vascular endothelium growth factor.[79] When ossification occurs, the cartilaginous ECM is gradually degraded and invaded by blood vessels, while chondrocytes become apoptotic. Osteoblasts coming from the blood stream invade the tissue, and cartilage gradually transforms into bone. Then, collagen II is replaced by collagen I, the predominant collagen in bone.[80]

Sources of Chondroprogenitor Cells

Cartilage has two main ontogenetic origins: the mesoderm and the neural crest. In both cases, MCs are generated from less differentiated Sox9-expressing cells that start skeletogenesis with the mesenchymal condensation.[24] The NCMCs that give rise to the craniofacial skeletal structure are formed from ectodermal cells, which suggests that ectodermal and mesodermal cells are embryonic origins for chondrocytes. Because two out of the three germ layers produce chondroprogenitor cells, it is quite probable that many cells of mesodermal or ectodermal origin could turn into chondrocytes with the proper signaling mechanisms.

In vitro chondrogenesis has been described with adult multipotent cells from bone marrow,[26,81,82] muscle,[83,84] synovial or periosteal cartilage,[84] and adipose tissue.[26,82,84] To date, the results show that the best chondroprogenitors of adult MSC origin are those of the synovial or periosteal cartilage, followed by muscular MSCs and bone marrow stromal cells, which have better chondrogenic commitment than progenitor cells from adipose tissue.[84] MSCs possess a multipotent capacity that is characterized by their ability to differentiate into chondrocytes, osteoblasts, and adipocytes. Further, in their function as stem cells they are able to
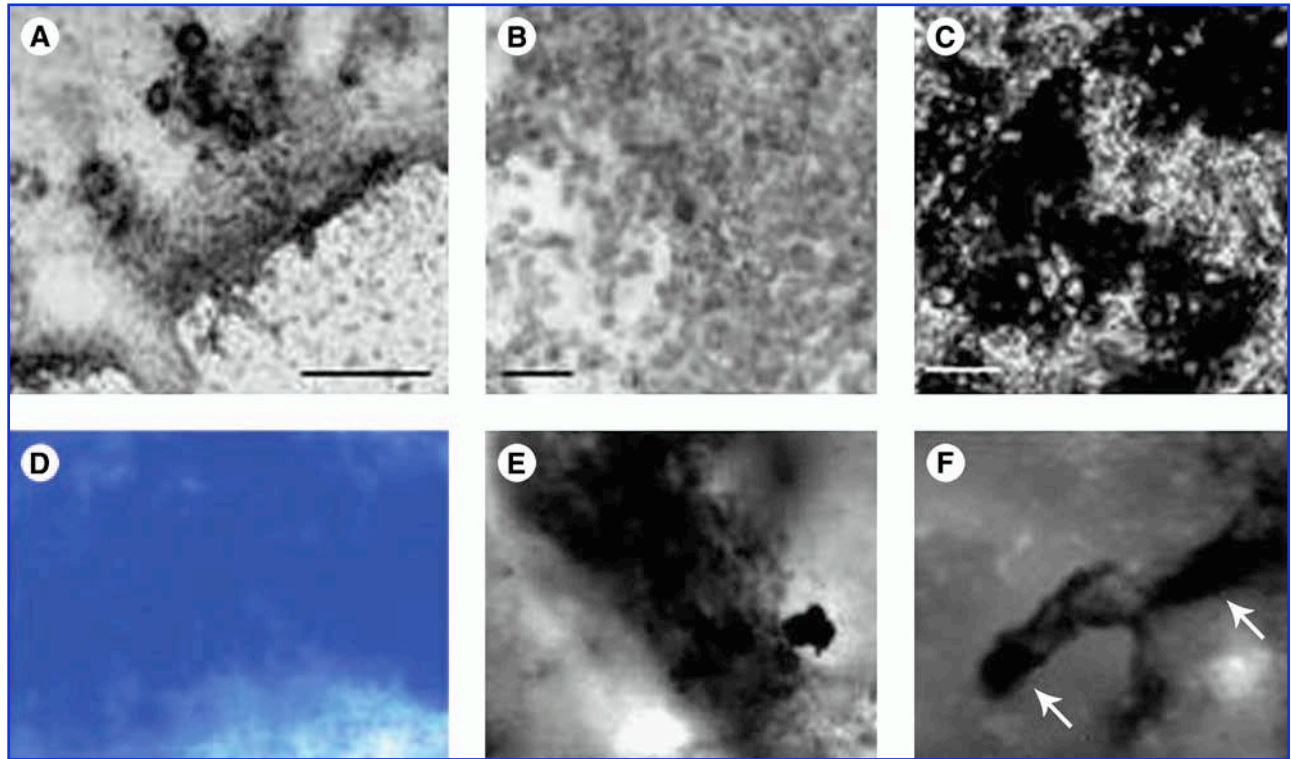

FIG. 3. *In vitro* models for chondrogenesis and osteogenesis with embryonic primitive cells (mESCs and mouse embryonic fibroblasts [MEFs]). (**A, B**) Chondrocytes were derived from mESCs with BMP-2 and TGF-β1 as described.[92] After 4 weeks of *in vitro* culture, cartilage nodules appear that contain small round cells (**B**) that secrete a grayish matrix that differs from mature mineralized osteogenic cultures shown in (**C**). (**D**) Toluidine blue staining of MEFs cultured in RAD16-I with Dulbecco's modified Eagle's medium (DMEM) supplemented with fetal bovine serum (FBS), L-Glu, and antibiotics reveals that these cells spontaneously undergo chondrogenesis and produce proteoglycans.[102] (**E**) Von Kossa staining of MEFs after 21 days cultured in RAD16-I with DMEM supplemented with FBS, L-Glu, β-glycerophosphate, dexamethasone, sodium ascorbate, and antibiotics. MEFs can also promote calcium deposition and become osteoblast-like cells.[99] (**F**) mESCs after osteogenic induction in RAD16-I hydrogels produce osteoblasts-like cells that induce calcium salts deposition, indicated by white arrows.[99] Scale bars: 100 μm. Color images available online at www.liebertonline.com/ten.

self-renew, however, only for a limited number of passages *in vitro*.[85] The best way to isolate MSCs remains elusive. Originally, isolation protocols have been described that rely on the fact that MSCs readily adhere to plastic.[86] Intermittently, the multilineage potential of MSCs has been characterized after isolation by FACS (Fluorescence-activated cell sorting) using a monoclonal antibody against STRO-1[87,88] and the low-affinity nerve growth factor receptor, also named CD271.[89] Only recently, Pittenger *et al.*[90] published a landmark paper describing surface marker expression characteristic of MSCs as being $CD29^+$, $CD44^+$, $CD71^+$, $CD90^+$, $CD106^+$, $CD120^+$, and $CD124^+$.

Chondrogenesis from embryonic stem cells (ESCs) has also been reported.[91,92] In contrast to MSCs, ESCs have to go through additional developmental stages to reach the fully differentiated chondrocyte state because they represent a pluripotent population. This is achieved through induction with BMP-2 or BMP-4 in murine and human ESCs.[91,93] Similar to the *in vivo* embryonic chondrogenic events, additional induction with TGFs can augment chondrogenesis,[92] underlining the importance of resembling stem cell differentiation systems according to *in vivo* embryonic development (Fig. 3A, B). Interestingly, these chondrocytic cultures can undergo hypertrophy, mineralize, and express bone-specific markers such as collagen I when challenged with osteogenic inducers like vitamin D_3.[92] It could therefore be hypothesized that this particular culture model represents endochondral bone formation (Fig. 3C, F, and Fig. 4). Further, overexpression of human Sox9 in murine ESCs (mESCs) leads to upregulated expression of the cartilage markers collagen IIA, aggrecan, and pax1 even in undifferentiated ESCs.[94] Upon induced differentiation, the adult form of collagen II (the isoform collagen IIB) was expressed by the Sox9 overexpressing ESCs, again emphasizing the importance of this transcriptional regulator.
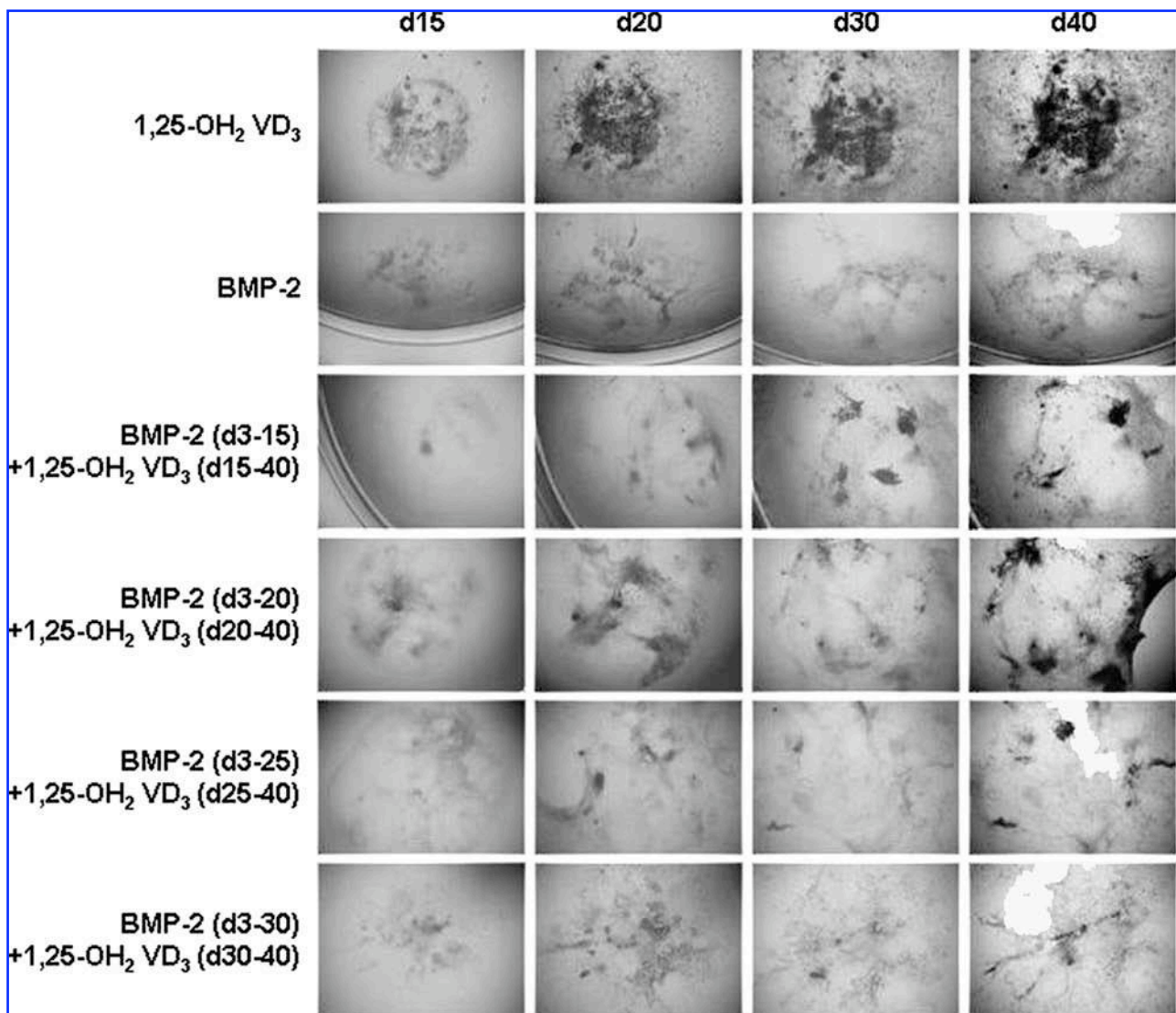

FIG. 4. Endochondral bone formation from mESCs *in vitro*. mESCs were differentiated with 1,25-OH$_2$ vitamin D$_3$ toward osteoblasts, which appear black in phase contrast microscopy. Chondrogenic cultures were treated with BMP-2 from day 3 of differentiation onward. Interestingly, chondrogenic cultures can undergo mineralization when additionally triggered with the osteogenic inducer 1,25-OH$_2$ vitamin D$_3$. However, a window of opportunity seems to exist that falls between day 15 and day 20 of differentiation.[92]

Further evidence for how critical it is to modulate stem cell differentiation according to developmental events found *in vivo* comes from two papers by Hwang *et al.*, who have utilized the supportive effects of ECM molecules to enhance chondrogenic differentiation from ESCs *in vitro*. In the presence of glucosamine, a component of glycosaminoglycans such as heparin sulfate and hyaluronan, or encapsulated in RGD-modified (arginine-glycine-aspartic acid integrim binding motif) hydrogels, neocartilage formation from ESCs could be detected accompanied by an increase in cartilage-specific gene expression.[95,96]

Usage of both ESCs and MSCs in tissue engineering and clinical application is characterized by certain caveats. Although being the stem cells with the highest differentiation potential, ESCs represent a population of cells encircled by moral and ethical dilemma. MSCs, in turn, can be harvested from the patient, however, not without invasive surgery. The search for alternative cell sources is therefore still ongoing. Other possible sources of chondroprogenitor cells appear from the natural process of the limb regeneration in amphibians. There, the first step in limb regeneration is the formation of a cell mass called blastema containing dedifferentiated chondroblasts, myoblasts, and fibroblasts.[97] Although there is evidence that myotubes can enter cellularization in mammals,[98] no chondrogenesis has been achieved with adult myotubes. On the other hand, fibroblasts have extensively shown multipotential capacity[99–101] and specifically chondrogenic capacity.[67,69] Moreover, fibroblasts can undergo spontaneous chondrogenesis in simple three-dimensional culture conditions (Fig. 3D) showing a high synthesis of proteoglycans.[102] The same chondrogenic cultures can be induced to differentiate into bone-like tissue (Fig. 3E) by inducing the system with osteogenic media.[99] This makes fibroblasts (where embryonic or adult) good and reliable candidates in future therapeutic approaches for cartilage and bone repair.

Mimicking Cell–ECM Interactions with Biomaterials

The broad incidence of the diseases related to cartilage and bone degeneration explains the emergence of a great amount of engineered tissues for cartilage repair. All of them are formed with biomaterials, cells, or a combination of both. The cells to be used vary from mature chondrocytes to any type of the previously described chondroprogenitor cells.

Polylactic acid (PLA), polyglycolic acid (PGA), and polylactic-coglycolic acid (PLGA) are U.S. Food and Drug Administration–approved materials for medical use that are extensively studied for cartilage repair applications.[103,104] PLA and PLGA have also been tested *in vivo* in combination with progenitor cells from the bone marrow[105] and also mixed with articular chondrocytes.[106] The good performance of PLA and PLGA *in vivo* makes of them one of the reference tools for the medical reconstruction of cartilage and bone defects such as Bankart's reconstruction, which is the reattachment of the capsule and glenoid labrum to the glenoid lip.[107,108]

Apart from PLA and PGA, other polymers to regenerate cartilage or bone are currently being studied, including polycaprolactones,[109,110] polyfumarates,[111] polyethyleneglycol,[112] polyvinyl alcohol,[113,114] and polyethylene oxide.[115] All of them are nontoxic, nonimmunogenic, and bioresorbable and have proven to be effective in allowing chondrocyte growth.

Apart from polymers, peptide-based matrices are the other important family of scaffolds used in regenerative medicine. Many natural ECM, such as collagen ECM or the basement membrane, have a high-protein content.[116,117] Consequently, many bioinspired engineered tissues have peptides or large proteins within their structure. A whole family of self-assembling peptides has been isolated or engineered over the last 15 years, and many of them have been tested promising for tissue engineering applications.[26,118–120] The self-assembly of peptides is driven by noncovalent interactions, such as hydrogen bonds, and polar and hydrophobic interactions giving rise to interweaving nanofibers.[121]

An example of a peptide matrix is RAD16-I, a 16–amino acid peptide that self-assembles to form a scaffold with a distribution of pore sizes between 50 and 100 nm.[122] This soft scaffold has proved to be permissive for the growth of different cell types and nontoxic to rats.[119,123,124] Recently, RAD16-I was used to recreate mesenchymal condensation *in vitro*. We have developed an assay with which embryonic fibroblasts, encapsulated in RAD16-I, proliferate and condense to form a dense cell mass with bilateral symmetry.[102] The volume reduction can be as high as 50%, but, more interestingly, bilaterality is accompanied by spontaneous chondrogenesis of the fibroblasts. This phenomenon has many similarities compared to mesenchymal condensation and limb bud regeneration. It is interesting that the condensation of fibroblasts only happens when the peptide that forms the nanofiber matrix is diluted enough to render a soft three-dimensional environment to the cells. When fibroblasts are cultured in slightly higher concentrations of the peptide, which give rise to stiffer hydrogels, they fail to condense although they form cellular networks. This work supports the previously discussed fact that cell–cell contact and a soft ECM are necessary in mesenchymal condensation.

We consider that the use of new paradigms in tissue engineering and regenerative medicine is crucial to obtain *in vitro* constructs and *in vivo* therapies with the capacity of truly regenerate damage tissues and organs. Hence, future medical standards for tissue-engineered–derived products will require not only to achieve functionality but also to be safe (nongenotoxic and nontumorigenic), to present high degree of integration with the local tissue (nonrejection and noninflammatory), and to recover natural shape and volume (esthetics). This is way the material reviewed here aims to integrate new concepts and ideas learned by looking at the natural developmental process of chondrogenesis with the hope to create more efficient therapeutic modalities.

Conclusions and Future Directions

Cartilage development is a tightly regulated morphogenetic event where many balances define the fate of chondroprogenitor cells. Much has been studied on gene regulation by different types of signaling molecules (TGF-β, BMPs, FGFs, Wnt, Ihh, and others). Moreover, the onset of the key chondrogenesis transcription factors Sox5, Sox6, and specially Sox9 is well characterized, but less is known of their downstream regulations.

The structure and changes of the ECM during cartilage formation are very well described in the literature. It is also

clear that chondrogenesis is affected by the ECM surrounding the MCs. But very little is known of this matter, and major efforts should be undertaken to achieve this goal. The control over cell fate by the ECM could be a very powerful tool for regenerative medicine. We can speculate that for a future therapeutic approach, freshly isolated progenitor cells could be implanted with an ECM analog capable of assisting differentiation and integration of these cells into the host tissue.

Finally, the last 20 years have been very prolific in obtaining mature chondrocytes out of other differentiated or multipotent cells and new biomaterials suitable for tissue regeneration. Briefly, cartilage-like tissues have been obtained from many cell types using different scaffolds. From all chondroprogenitors, fibroblasts have shown spontaneous and high chondrogenic commitment. The fact that fibroblasts can be easily extracted from the skin combined with their chondrogenic potential makes of them good candidates for cartilage repair, and eventually bone.

Acknowledgments

Disclosure Statement

No competing financial interests exist.

References

1. Newman, S.A., and Frisch, H.L. Dynamics of skeletal pattern formation in developing chick limb. Science **205,** 662, 1979.
2. Horton, W.A., Hood, O.J., Machado, M.A., Ahmed, S., and Griffey, E.S. Abnormal ossification in thanatophoric dysplasia. Bone **9,** 53, 1988.
3. Hall, B.K., and Miyake, T. Divide, accumulate, differentiate: cell condensation in skeletal development revisited. Int J Dev Biol **39,** 881, 1995.
4. Hoffman, L.M., Weston, A.D., and Underhill, T.M. Molecular mechanisms regulating chondroblast differentiation. J Bone Joint Surg Am **85-A Suppl 2,** 124, 2003.
5. Mackie, E.J., Ahmed, Y.A., Tatarczuch, L., Chen, K.S., and Mirams, M. Endochondral ossification: how cartilage is converted into bone in the developing skeleton. Int J Biochem Cell Biol **40,** 46, 2008.
6. Olsen, B.R., Reginato, A.M., and Wang, W. Bone development. Annu Rev Cell Dev Biol **16,** 191, 2000.
7. DeLise, A.M., and Tuan, R.S. Alterations in the spatiotemporal expression pattern and function of N-cadherin inhibit cellular condensation and chondrogenesis of limb mesenchymal cells *in vitro*. J Cell Biochem **87,** 342, 2002.
8. DeLise, A.M., Fischer, L., and Tuan, R.S. Cellular interactions and signaling in cartilage development. Osteoarthritis Cartilage **8,** 309, 2000.
9. Goldring, M.B., Tsuchimochi, K., and Ijiri, K. The control of chondrogenesis. J Cell Biochem **97,** 33, 2006.
10. Ichinose, S., Tagami, M., Muneta, T., and Sekiya, I. Morphological examination during *in vitro* cartilage formation by human mesenchymal stem cells. Cell Tissue Res **322,** 217, 2005.
11. Sahar, D.E., Longaker, M.T., and Quarto, N. Sox9 neural crest determinant gene controls patterning and closure of the posterior frontal cranial suture. Dev Biol **280,** 344, 2005.
12. Shibata, S., Fukada, K., Imai, H., Abe, T., and Yamashita, Y. *In situ* hybridization and immunohistochemistry of versican, aggrecan and link protein, and histochemistry of hyaluronan in the developing mouse limb bud cartilage. J Anat **203,** 425, 2003.
13. Franz-Odendaal, T.A., Hall, B.K., and Witten, P.E. Buried alive: how osteoblasts become osteocytes. Dev Dyn **235,** 176, 2006.
14. Opperman, L.A. Cranial sutures as intramembranous bone growth sites. Dev Dyn **219,** 472, 2000.
15. Kamiya, N., Watanabe, H., Habuchi, H., Takagi, H., Shinomura, T., Shimizu, K., and Kimata, K. Versican/PG-M regulates chondrogenesis as an extracellular matrix molecule crucial for mesenchymal condensation. J Biol Chem **281,** 2390, 2006.
16. Chai, Y., Jiang, X., Ito, Y., Bringas, P., Jr., Han, J., Rowitch, D.H., Soriano, P., McMahon, A.P., and Sucov, H.M. Fate of the mammalian cranial neural crest during tooth and mandibular morphogenesis. Development **127,** 1671, 2000.
17. Melnick, M., Witcher, D., Bringas, P., Jr., Carlsson, P., and Jaskoll, T. Meckel's cartilage differentiation is dependent on hedgehog signaling. Cells Tissues Organs **179,** 146, 2005.
18. Akiyama, H., Chaboissier, M.C., Martin, J.F., Schedl, A., and de Crombrugghe, B. The transcription factor Sox9 has essential roles in successive steps of the chondrocyte differentiation pathway and is required for expression of Sox5 and Sox6. Genes Dev **16,** 2813, 2002.
19. Kawakami, Y., Rodriguez-Leon, J., and Belmonte, J.C. The role of TGFbetas and Sox9 during limb chondrogenesis. Curr Opin Cell Biol **18,** 723, 2006.
20. Eames, B.F., de la Fuente, L., and Helms, J.A. Molecular ontogeny of the skeleton. Birth Defects Res C Embryo Today **69,** 93, 2003.
21. Lefebvre, V., Behringer, R.R., and de Crombrugghe, B. L-Sox5, Sox6 and Sox9 control essential steps of the chondrocyte differentiation pathway. Osteoarthritis Cartilage **9 Suppl A,** S69, 2001.
22. Ng, L.J., Wheatley, S., Muscat, G.E., Conway-Campbell, J., Bowles, J., Wright, E., Bell, D.M., Tam, P.P., Cheah, K.S., and Koopman, P. SOX9 binds DNA, activates transcription, and coexpresses with type II collagen during chondrogenesis in the mouse. Dev Biol **183,** 108, 1997.
23. Smits, P., Li, P., Mandel, J., Zhang, Z., Deng, J.M., Behringer, R.R., de Crombrugghe, B., and Lefebvre, V. The transcription factors L-Sox5 and Sox6 are essential for cartilage formation. Dev Cell **1,** 277, 2001.
24. Akiyama, H., Kim, J.E., Nakashima, K., Balmes, G., Iwai, N., Deng, J.M., Zhang, Z., Martin, J.F., Behringer, R.R., Nakamura, T., and de Crombrugghe, B. Osteochondroprogenitor cells are derived from Sox9 expressing precursors. Proc Natl Acad Sci USA **102,** 14665, 2005.
25. Derfoul, A., Perkins, G.L., Hall, D.J., and Tuan, R.S. Glucocorticoids promote chondrogenic differentiation of adult human mesenchymal stem cells by enhancing expression of cartilage extracellular matrix genes. Stem Cells **24,** 1487, 2006.
26. Kisiday, J.D., Kopesky, P.W., Evans, C.H., Grodzinsky, A.J., McIlwraith, C.W., and Frisbie, D.D. Evaluation of adult equine bone marrow- and adipose-derived progenitor cell

chondrogenesis in hydrogel cultures. J Orthop Res **26,** 322, 2008.

27. Terraciano, V., Hwang, N., Moroni, L., Park, H.B., Zhang, Z., Mizrahi, J., Seliktar, D., and Elisseeff, J. Differential response of adult and embryonic mesenchymal progenitor cells to mechanical compression in hydrogels. Stem Cells **25,** 2730, 2007.

28. Lallemand, Y., Nicola, M.A., Ramos, C., Bach, A., Cloment, C.S., and Robert, B. Analysis of Msx1; Msx2 double mutants reveals multiple roles for Msx genes in limb development. Development **132,** 3003, 2005.

29. Basch, M.L., Bronner-Fraser, M., and Garcia-Castro, M.I. Specification of the neural crest occurs during gastrulation and requires Pax7. Nature **441,** 218, 2006.

30. Liem, K.F., Jr., Tremml, G., Roelink, H., and Jessell, T.M. Dorsal differentiation of neural plate cells induced by BMP-mediated signals from epidermal ectoderm. Cell **82,** 969, 1995.

31. Yoon, B.S., Ovchinnikov, D.A., Yoshii, I., Mishina, Y., Behringer, R.R., and Lyons, K.M. Bmpr1a and Bmpr1b have overlapping functions and are essential for chondrogenesis *in vivo*. Proc Natl Acad Sci USA **102,** 5062, 2005.

32. Minina, E., Wenzel, H.M., Kreschel, C., Karp, S., Gaffield, W., McMahon, A.P., and Vortkamp, A. BMP and Ihh/PTHrP signaling interact to coordinate chondrocyte proliferation and differentiation. Development **128,** 4523, 2001.

33. Tsumaki, N., and Yoshikawa, H. The role of bone morphogenetic proteins in endochondral bone formation. Cytokine Growth Factor Rev **16,** 279, 2005.

34. Mehlhorn, A.T., Niemeyer, P., Kaschte, K., Muller, L., Finkenzeller, G., Hartl, D., Sudkamp, N.P., and Schmal, H. Differential effects of BMP-2 and TGF-beta1 on chondrogenic differentiation of adipose derived stem cells. Cell Prolif **40,** 809, 2007.

35. Hall, C., Flores, M.V., Murison, G., Crosier, K., and Crosier, P. An essential role for zebrafish Fgfrl1 during gill cartilage development. Mech Dev **123,** 925, 2006.

36. Kawakami, A., Fukazawa, T., and Takeda, H. Early fin primordia of zebrafish larvae regenerate by a similar growth control mechanism with adult regeneration. Dev Dyn **231,** 693, 2004.

37. Nye, H.L., Cameron, J.A., Chernoff, E.A., and Stocum, D.L. Regeneration of the urodele limb: a review. Dev Dyn **226,** 280, 2003.

38. Day, T.F., Guo, X., Garrett-Beal, L., and Yang, Y. Wnt/beta-catenin signaling in mesenchymal progenitors controls osteoblast and chondrocyte differentiation during vertebrate skeletogenesis. Dev Cell **8,** 739, 2005.

39. Tamamura, Y., Otani, T., Kanatani, N., Koyama, E., Kitagaki, J., Komori, T., Yamada, Y., Costantini, F., Wakisaka, S., Pacifici, M., Iwamoto, M., and Enomoto-Iwamoto, M. Developmental regulation of Wnt/beta-catenin signals is required for growth plate assembly, cartilage integrity, and endochondral ossification. J Biol Chem **280,** 19185, 2005.

40. Akiyama, H., Lyons, J.P., Mori-Akiyama, Y., Yang, X., Zhang, R., Zhang, Z., Deng, J.M., Taketo, M.M., Nakamura, T., Behringer, R.R., McCrea, P.D., and de Crombrugghe, B. Interactions between Sox9 and beta-catenin control chondrocyte differentiation. Genes Dev **18,** 1072, 2004.

41. Hartmann, C., and Tabin, C.J. Dual roles of Wnt signaling during chondrogenesis in the chicken limb. Development **127,** 3141, 2000.

42. Church, V., Nohno, T., Linker, C., Marcelle, C., and Francis-West, P. Wnt regulation of chondrocyte differentiation. J Cell Sci **115,** 4809, 2002.

43. Tuli, R., Tuli, S., Nandi, S., Huang, X., Manner, P.A., Hozack, W.J., Danielson, K.G., Hall, D.J., and Tuan, R.S. Transforming growth factor-beta-mediated chondrogenesis of human mesenchymal progenitor cells involves N-cadherin and mitogen-activated protein kinase and Wnt signaling cross-talk. J Biol Chem **278,** 41227, 2003.

44. Enomoto, H., Enomoto-Iwamoto, M., Iwamoto, M., Nomura, S., Himeno, M., Kitamura, Y., Kishimoto, T., and Komori, T. Cbfa1 is a positive regulatory factor in chondrocyte maturation. J Biol Chem **275,** 8695, 2000.

45. Leboy, P., Grasso-Knight, G., D'Angelo, M., Volk, S.W., Lian, J.V., Drissi, H., Stein, G.S., and Adams, S.L. Smad-Runx interactions during chondrocyte maturation. J Bone Joint Surg Am **83-A Suppl 1,** S15, 2001.

46. Zheng, Q., Zhou, G., Morello, R., Chen, Y., Garcia-Rojas, X., and Lee, B. Type X collagen gene regulation by Runx2 contributes directly to its hypertrophic chondrocyte-specific expression *in vivo*. J Cell Biol **162,** 833, 2003.

47. Komori, T., Yagi, H., Nomura, S., Yamaguchi, A., Sasaki, K., Deguchi, K., Shimizu, Y., Bronson, R.T., Gao, Y.H., Inada, M., Sato, M., Okamoto, R., Kitamura, Y., Yoshiki, S., and Kishimoto, T. Targeted disruption of Cbfa1 results in a complete lack of bone formation owing to maturational arrest of osteoblasts. Cell **89,** 755, 1997.

48. Otto, F., Thornell, A.P., Crompton, T., Denzel, A., Gilmour, K.C., Rosewell, I.R., Stamp, G.W., Beddington, R.S., Mundlos, S., Olsen, B.R., Selby, P.B., and Owen, M.J. Cbfa1, a candidate gene for cleidocranial dysplasia syndrome, is essential for osteoblast differentiation and bone development. Cell **89,** 765, 1997.

49. Suzuki, T., Sakai, D., Osumi, N., Wada, H., and Wakamatsu, Y. Sox genes regulate type 2 collagen expression in avian neural crest cells. Dev Growth Differ **48,** 477, 2006.

50. Hattori, T., Eberspaecher, H., Lu, J., Zhang, R., Nishida, T., Kahyo, T., Yasuda, H., and de Crombrugghe, B. Interactions between PIAS proteins and SOX9 result in an increase in the cellular concentrations of SOX9. J Biol Chem **281,** 14417, 2006.

51. Huang, W., Zhou, X., Lefebvre, V., and de Crombrugghe, B. Phosphorylation of SOX9 by cyclic AMP-dependent protein kinase A enhances SOX9's ability to transactivate a Col2a1 chondrocyte-specific enhancer. Mol Cell Biol **20,** 4149, 2000.

52. Genzer, M.A., and Bridgewater, L.C. A Col9a1 enhancer element activated by two interdependent SOX9 dimers. Nucleic Acids Res **35,** 1178, 2007.

53. Bridgewater, L.C., Walker, M.D., Miller, G.C., Ellison, T.A., Holsinger, L.D., Potter, J.L., Jackson, T.L., Chen, R.K., Winkel, V.L., Zhang, Z., McKinney, S., and de Crombrugghe, B. Adjacent DNA sequences modulate Sox9 transcriptional activation at paired Sox sites in three chondrocyte-specific enhancer elements. Nucleic Acids Res **31,** 1541, 2003.

54. Liu, C.J., Zhang, Y., Xu, K., Parsons, D., Alfonso, D., and Di Cesare, P.E. Transcriptional activation of cartilage oligomeric matrix protein by Sox9, Sox5, and Sox6 transcription factors and CBP/p300 coactivators. Front Biosci **12,** 3899, 2007.

55. Mello, M.A., and Tuan, R.S. Effects of TGF-beta1 and tri-iodothyronine on cartilage maturation: *in vitro* analysis using long-term high-density micromass cultures of chick embryonic limb mesenchymal cells. J Orthop Res **24,** 2095, 2006.

56. Shimizu, H., Yokoyama, S., and Asahara, H. Growth and differentiation of the developing limb bud from the

perspective of chondrogenesis. Dev Growth Differ **49,** 449, 2007.

57. Guimont, P., Grondin, F., and Dubois, C.M. Sox9-dependent transcriptional regulation of the proprotein convertase furin. Am J Physiol Cell Physiol **293,** C172, 2007.

58. Huang, W., Chung, U.I., Kronenberg, H.M., and de Crombrugghe, B. The chondrogenic transcription factor Sox9 is a target of signaling by the parathyroid hormone-related peptide in the growth plate of endochondral bones. Proc Natl Acad Sci USA **98,** 160, 2001.

59. Woods, A., Wang, G., Dupuis, H., Shao, Z., and Beier, F. Rac1 signaling stimulates N-cadherin expression, mesenchymal condensation, and chondrogenesis. J Biol Chem **282,** 23500, 2007.

60. Luo, Y., Kostetskii, I., and Radice, G.L. N-cadherin is not essential for limb mesenchymal chondrogenesis. Dev Dyn **232,** 336, 2005.

61. Modarresi, R., Lafond, T., Roman-Blas, J.A., Danielson, K.G., Tuan, R.S., and Seghatoleslami, M.R. N-cadherin mediated distribution of beta-catenin alters MAP kinase and BMP-2 signaling on chondrogenesis-related gene expression. J Cell Biochem **95,** 53, 2005.

62. Woitge, H.W., and Seibel, M.J. Molecular markers of bone and cartilage metabolism. Curr Opin Rheumatol **11,** 218, 1999.

63. Kondo, S., Shukunami, C., Morioka, Y., Matsumoto, N., Takahashi, R., Oh, J., Atsumi, T., Umezawa, A., Kudo, A., Kitayama, H., Hiraki, Y., and Noda, M. Dual effects of the membrane-anchored MMP regulator RECK on chondrogenic differentiation of ATDC5 cells. J Cell Sci **120,** 849, 2007.

64. Jin, E.J., Choi, Y.A., Kyun Park, E., Bang, O.S., and Kang, S.S. MMP-2 functions as a negative regulator of chondrogenic cell condensation via down-regulation of the FAK-integrin beta1 interaction. Dev Biol **308,** 474, 2007.

65. Zhou, Z., Apte, S.S., Soininen, R., Cao, R., Baaklini, G.Y., Rauser, R.W., Wang, J., Cao, Y., and Tryggvason, K. Impaired endochondral ossification and angiogenesis in mice deficient in membrane-type matrix metalloproteinase I. Proc Natl Acad Sci USA **97,** 4052, 2000.

66. Ohkubo, K., Shimokawa, H., Ogawa, T., Suzuki, S., Fukada, K., Ohya, K., and Ohyama, K. Immunohistochemical localization of matrix metalloproteinase 13 (MMP-13) in mouse mandibular condylar cartilage. J Med Dent Sci **50,** 203, 2003.

67. French, M.M., Smith, S.E., Akanbi, K., Sanford, T., Hecht, J., Farach-Carson, M.C., and Carson, D.D. Expression of the heparan sulfate proteoglycan, perlecan, during mouse embryogenesis and perlecan chondrogenic activity *in vitro*. J Cell Biol **145,** 1103, 1999.

68. Knox, S.M., and Whitelock, J.M. Perlecan: how does one molecule do so many things? Cell Mol Life Sci **63,** 2435, 2006.

69. Gomes, R.R., Jr., Joshi, S.S., Farach-Carson, M.C., and Carson, D.D. Ribozyme-mediated perlecan knockdown impairs chondrogenic differentiation of C3H10T1/2 fibroblasts. Differentiation **74,** 53, 2006.

70. Hopf, M., Gohring, W., Kohfeldt, E., Yamada, Y., and Timpl, R. Recombinant domain IV of perlecan binds to nidogens, laminin-nidogen complex, fibronectin, fibulin-2 and heparin. Eur J Biochem **259,** 917, 1999.

71. Takada, T., Katagiri, T., Ifuku, M., Morimura, N., Kobayashi, M., Hasegawa, K., Ogamo, A., and Kamijo, R. Sulfated polysaccharides enhance the biological activities of bone morphogenetic proteins. J Biol Chem **278,** 43229, 2003.

72. Arikawa-Hirasawa, E., Watanabe, H., Takami, H., Hassell, J.R., and Yamada, Y. Perlecan is essential for cartilage and cephalic development. Nat Genet **23,** 354, 1999.

73. Fears, C.Y., and Woods, A. The role of syndecans in disease and wound healing. Matrix Biol **25,** 443, 2006.

74. Fisher, M.C., Li, Y., Seghatoleslami, M.R., Dealy, C.N., and Kosher, R.A. Heparan sulfate proteoglycans including syndecan-3 modulate BMP activity during limb cartilage differentiation. Matrix Biol **25,** 27, 2006.

75. Plainfosse, M., Hatton, P.V., Crawford, A., Jin, Z.M., and Fisher, J. Influence of the extracellular matrix on the frictional properties of tissue-engineered cartilage. Biochem Soc Trans **35,** 677, 2007.

76. Poole, A.R., Kojima, T., Yasuda, T., Mwale, F., Kobayashi, M., and Laverty, S. Composition and structure of articular cartilage: a template for tissue repair. Clin Orthop Relat Res **39l Suppl,** S26, 2001.

77. Stokes, D.G., Liu, G., Dharmavaram, R., Hawkins, D., Piera-Velazquez, S., and Jimenez, S.A. Regulation of type-II collagen gene expression during human chondrocyte de-differentiation and recovery of chondrocyte-specific phenotype in culture involves Sry-type high-mobility-group box (SOX) transcription factors. Biochem J **360,** 461, 2001.

78. Bosnakovski, D., Mizuno, M., Kim, G., Takagi, S., Okumura, M., and Fujinaga, T. Chondrogenic differentiation of bovine bone marrow mesenchymal stem cells (MSCs) in different hydrogels: influence of collagen type II extracellular matrix on MSC chondrogenesis. Biotechnol Bioeng **93,** 1152, 2006.

79. Bluteau, G., Julien, M., Magne, D., Mallein-Gerin, F., Weiss, P., Daculsi, G., and Guicheux, J. VEGF and VEGF receptors are differentially expressed in chondrocytes. Bone **40,** 568, 2007.

80. Termine, J.D., and Robey, P.G. Bone matrix proteins and the mineralization process. In: Favus, M.J., ed. Primer on the Metabolic Bone Diseases and Disorders of Mineral Metabolism. Philadelphia: Lippincott-Raven, 1996, pp. 24–28.

81. Evans, J.F., Niu, Q.T., Canas, J.A., Shen, C.L., Aloia, J.F., and Yeh, J.K. ACTH enhances chondrogenesis in multipotential progenitor cells and matrix production in chondrocytes. Bone **35,** 96, 2004.

82. Huang, J.I., Kazmi, N., Durbhakula, M.M., Hering, T.M., Yoo, J.U., and Johnstone, B. Chondrogenic potential of progenitor cells derived from human bone marrow and adipose tissue: a patient-matched comparison. J Orthop Res **23,** 1383, 2005.

83. Stringa, E., Love, J.M., McBride, S.C., Suyama, E., and Tuan, R.S. *In vitro* characterization of chondrogenic cells isolated from chick embryonic muscle using peanut agglutinin affinity chromatography. Exp Cell Res **232,** 287, 1997.

84. Yoshimura, H., Muneta, T., Nimura, A., Yokoyama, A., Koga, H., and Sekiya, I. Comparison of rat mesenchymal stem cells derived from bone marrow, synovium, periosteum, adipose tissue, and muscle. Cell Tissue Res **327,** 449, 2007.

85. Stenderup, K., Justesen, J., Clausen, C., and Kassem, M. Aging is associated with decreased maximal life span and accelerated senescence of bone marrow stromal cells. Bone **33,** 919, 2003.

86. Friedenstein, A.J., Gorskaja, J.F., and Kulagina, N.N. Fibroblast precursors in normal and irradiated mouse hematopoietic organs. Exp Hematol **4,** 267, 1976.

87. Gronthos, S., Graves, S.E., Ohta, S., and Simmons, P.J. The STRO-1+ fraction of adult human bone marrow contains the osteogenic precursors. Blood **84,** 4164, 1994.

88. Simmons, P.J., and Torok-Storb, B. Identification of stromal cell precursors in human bone marrow by a novel monoclonal antibody, STRO-1. Blood **78,** 55, 1991.

89. Quirici, N., Soligo, D., Bossolasco, P., Servida, F., Lumini, C., and Deliliers, G.L. Isolation of bone marrow mesenchymal stem cells by anti-nerve growth factor receptor antibodies. Exp Hematol **30,** 783, 2002.

90. Pittenger, M.F., Mackay, A.M., Beck, S.C., Jaiswal, R.K., Douglas, R., Mosca, J.D., Moorman, M.A., Simonetti, D.W., Craig, S., and Marshak, D.R. Multilineage potential of adult human mesenchymal stem cells. Science **284,** 143, 1999.

91. Kramer, J., Hegert, C., Guan, K., Wobus, A.M., Muller, P.K., and Rohwedel, J. Embryonic stem cell-derived chondrogenic differentiation *in vitro*: activation by BMP-2 and BMP-4. Mech Dev **92,** 193, 2000.

92. zur Nieden, N.I., Kempka, G., Rancourt, D.E., and Ahr, H.J. Induction of chondro-, osteo- and adipogenesis in embryonic stem cells by bone morphogenetic protein-2: effect of cofactors on differentiating lineages. BMC Dev Biol **5,** 1, 2005.

93. Toh, W.S., Yang, Z., Liu, H., Heng, B.C., Lee, E.H., and Cao, T. Effects of culture conditions and bone morphogenetic protein 2 on extent of chondrogenesis from human embryonic stem cells. Stem Cells **25,** 950, 2007.

94. Kim, J.H., Do, H.J., Yang, H.M., Oh, J.H., Choi, S.J., Kim, D.K., Cha, K.Y., and Chung, H.M. Overexpression of SOX9 in mouse embryonic stem cells directs the immediate chondrogenic commitment. Exp Mol Med **37,** 261, 2005.

95. Hwang, N.S., Varghese, S., Theprungsirikul, P., Canver, A., and Elisseef, J. Enhanced chondrogenic differentiation of murine embryonic stem cells in hydrogels with glucosamine. Biomaterials **27,** 6015, 2006.

96. Hwang, N.S., Varghese, S., Zhang, Z., and Elisseef, J. Chondrogenic differentiation of human embryonic stem cell-derived cells in arginine-glycine-aspartate-modified hydrogels. Tissue Eng **12,** 2695, 2006.

97. Brockes, J.P., and Kumar, A. Plasticity and reprogramming of differentiated cells in amphibian regeneration. Nat Rev Mol Cell Biol **3,** 566, 2002.

98. Duckmanton, A., Kumar, A., Chang, Y.T., and Brockes, J.P. A single-cell analysis of myogenic dedifferentiation induced by small molecules. Chem Biol **12,** 1117, 2005.

99. Garreta, E., Genove, E., Borros, S., and Semino, C.E. Osteogenic differentiation of mouse embryonic stem cells and mouse embryonic fibroblasts in a three-dimensional self-assembling peptide scaffold. Tissue Eng **12,** 2215, 2006.

100. Wang, J., Li, A., Wang, Z., Feng, X., Olson, E.N., and Schwartz, R.J. Myocardin sumoylation transactivates cardiogenic genes in pluripotent 10T1/2 fibroblasts. Mol Cell Biol **27,** 622, 2007.

101. Yang, L.H., Chen, T.M., Yu, S.T., and Chen, Y.H. Olanzapine induces SREBP-1-related adipogenesis in 3T3-L1 cells. Pharmacol Res **56,** 202, 2007.

102. Quintana, L., Fernández, T., Genové, E., Olmos, M.M., Borrós, S., and Semino, C.E. Early tissue patterning is recreated by mouse embryonic fibroblasts in a three-dimensional environment. Tissue Eng 2009 (In Press).

103. Sherwood, J.K., Riley, S.L., Palazzolo, R., Brown, S.C., Monkhouse, D.C., Coates, M., Griffith, L.G., Landeen, L.K., and Ratcliffe, A. A three-dimensional osteochondral composite scaffold for articular cartilage repair. Biomaterials **23,** 4739, 2002.

104. Zwingmann, J., Mehlhorn, A.T., Sudkamp, N., Stark, B., Dauner, M., and Schmal, H. Chondrogenic differentiation of human articular chondrocytes differs in biodegradable PGA/PLA scaffolds. Tissue Eng **13,** 2335, 2007.

105. Zhou, G., Liu, W., Cui, L., Wang, X., Liu, T., and Cao, Y. Repair of porcine articular osteochondral defects in non-weightbearing areas with autologous bone marrow stromal cells. Tissue Eng **12,** 3209, 2006.

106. Sedrakyan, S., Zhou, Z.Y., Perin, L., Leach, K., Mooney, D., and Kim, T.H. Tissue engineering of a small hand phalanx with a porously casted polylactic acid-polyglycolic acid copolymer. Tissue Eng **12,** 2675, 2006.

107. Magnusson, L., Ejerhed, L., Rostgard-Christensen, L., Sernert, N., Eriksson, R., Karlsson, J., and Kartus, J.T. A prospective, randomized, clinical and radiographic study after arthroscopic Bankart reconstruction using 2 different types of absorbable tacks. Arthroscopy **22,** 143, 2006.

108. Martinez Martin, A.A., Herrera Rodriguez, A., Panisello Sebastian, J.J., Tabuenca Sanchez, A., Domingo Cebollada, J., and Perez Garcia, J.M. Use of the suture anchor in modified open Bankart reconstruction. Int Orthop **22,** 312, 1998.

109. Eyrich, D., Wiese, H., Maier, G., Skodacek, D., Appel, B., Sarhan, H., Tessmar, J., Staudenmaier, R., Wenzel, M.M., Goepferich, A., and Blunk, T. *In vitro* and *in vivo* cartilage engineering using a combination of chondrocyte-seeded long-term stable fibrin gels and polycaprolactone-based polyurethane scaffolds. Tissue Eng **13,** 2207, 2007.

110. Xie, J., Han, Z., Kim, S.H., Kim, Y.H., and Matsuda, T. Mechanical loading-dependence of mRNA expressions of extracellular matrices of chondrocytes inoculated into elastomeric microporous poly(L-lactide-co-epsilon-caprolactone) scaffold. Tissue Eng **13,** 29, 2007.

111. Park, H., Temenoff, J.S., Tabata, Y., Caplan, A.I., and Mikos, A.G. Injectable biodegradable hydrogel composites for rabbit marrow mesenchymal stem cell and growth factor delivery for cartilage tissue engineering. Biomaterials **28,** 3217, 2007.

112. Lee, S.H., and Shin, H. Matrices and scaffolds for delivery of bioactive molecules in bone and cartilage tissue engineering. Adv Drug Deliv Rev **59,** 339, 2007.

113. Bonzani, I.C., George, J.H., and Stevens, M.M. Novel materials for bone and cartilage regeneration. Curr Opin Chem Biol **10,** 568, 2006.

114. Mohan, N., and Nair, P.D. Polyvinyl alcohol-poly (caprolactone) semi IPN scaffold with implication for cartilage tissue engineering. J Biomed Mater Res B Appl Biomater **84,** 584, 2008.

115. Sharma, B., Williams, C.G., Khan, M., Manson, P., and Elisseef, J.H. *In vivo* chondrogenesis of mesenchymal stem cells in a photopolymerized hydrogel. Plast Reconstr Surg **119,** 112, 2007.

116. Engel, J. Laminins and other strange proteins. Biochemistry **31,** 10643, 1992.

117. Yurchenco, P.D., and O'Rear, J.J. Basal lamina assembly. Curr Opin Cell Biol **6,** 674, 1994.

118. Dhadwar, S.S., Bemman, T., Anderson, W.A., and Chen, P. Yeast cell adhesion on oligopeptide modified surfaces. Biotechnol Adv **21,** 395, 2003.

119. Holmes, T.C., de Lacalle, S., Su, X., Liu, G., Rich, A., and Zhang, S. Extensive neurite outgrowth and active synapse formation on self-assembling peptide scaffolds. Proc Natl Acad Sci USA **97,** 6728, 2000.

120. Nowak, A.P., Breedveld, V., Pakstis, L., Ozbas, B., Pine, D.J., Pochan, D., and Deming, T.J. Rapidly recovering

hydrogel scaffolds from self-assembling diblock copoly-peptide amphiphiles. Nature **417,** 424, 2002.

121. Kisiday, J., Jin, M., Kurz, B., Hung, H., Semino, C., Zhang, S., and Grodzinsky, A.J. Self-assembling peptide hydrogel fosters chondrocyte extracellular matrix production and cell division: implications for cartilage tissue repair. Proc Natl Acad Sci USA **99,** 9996, 2002.

122. Zhang, S., Holmes, T.C., DiPersio, C.M., Hynes, R.O., Su, X., and Rich, A. Self-complementary oligopeptide matrices support mammalian cell attachment. Biomaterials **16,** 1385, 1995.

123. Semino, C.E., Kasahara, J., Hayashi, Y., and Zhang, S. Entrapment of migrating hippocampal neural cells in three-dimensional peptide nanofiber scaffold. Tissue Eng **10,** 643, 2004.

124. Semino, C.E., Merok, J.R., Crane, G.G., Panagiotakos, G., and Zhang, S. Functional differentiation of hepatocyte-like spheroid structures from putative liver progenitor cells in three-dimensional peptide scaffolds. Differentiation **71,** 262, 2003.

Early Tissue Patterning Recreated by Mouse Embryonic Fibroblasts in a Three-Dimensional Environment

Lluís Quintana, M.S.,[1,2] Teresa Fernández Muiños, M.S.,[1,2] Elsa Genové, Ph.D.,[1,2] María Del Mar Olmos, M.S.,[1,2] Salvador Borrós, Ph.D.,[2] and Carlos E. Semino, Ph.D.[1,2]

Cellular self-organization studies have been mainly focused on models such as *Volvox*, the slime mold *Dictyostelium discoideum*, and animal (metazoan) embryos. Moreover, animal tissues undergoing regeneration also exhibit properties of embryonic systems such as the self-organization process that rebuilds tissue complexity and function. We speculated that the recreation *in vitro* of the biological, biophysical, and biomechanical conditions *similar* to those of a regenerative milieu could elicit the intrinsic capacity of differentiated cells to proceed to the development of a tissue-like structure. Here we show that, when primary mouse embryonic fibroblasts are cultured in a soft nanofiber scaffold, they establish a cellular network that causes an organized cell contraction, proliferation, and migration that ends in the formation of a symmetrically bilateral structure with a distinct central axis. A subset of mesodermal genes (*brachyury, Sox9, Runx2*) is upregulated during this morphogenetic process. The expression of brachyury was localized first at the central axis, extending then to both sides of the structure. The spontaneous formation of cartilage-like tissue mainly at the paraxial zone followed expression of Sox9 and Runx2. Because cellular self-organization is an intrinsic property of the tissues undergoing development, this model could lead to new ways to consider tissue engineering and regenerative medicine.

Introduction

CELLULAR SELF-ORGANIZATION STUDIES have been mainly focused on models such as *Volvox*, the slime mold *Dictyostelium discoideum*, and animal (metazoan) embryos. These models have something in common; their individual cells need to adhere together to form a cohesive organism. Free *Dictyostelium* cells synthesize a sticky 24-kDa glycoprotein under nutritional deficit, becoming increasingly adhesive and promoting the formation of cellular aggregates that undergo differentiation into an organized structure.[1–4] A similar mechanism occurs in early animal embryos, where cells adhere together to form tissues and organs during development. In addition, animal tissues undergoing regeneration present intrinsic properties of embryonic systems, including cell multipotential capacity and pattern expression of developmental genes by a self-organizational process to rebuild tissue complexity and function.[5–9] For instance, the process of mammal digit tip regeneration displays phases similar to those found in limb regeneration in amphibians: apical epithelial cap (AEC) formation; blastema-like formation by dermal fibroblast and myotube dedifferentiation; and regeneration or re-development, leading to scarless wound

healing.[5–9] We speculate that the recreation of a suitable microenvironment similar to that of regenerative areas (with reduced or non-inflammatory response) is possible to develop *in vitro* by recreating the biological, biophysical, and biomechanical conditions. This microenvironment would promote the intrinsic capacity of adult tissues to proceed to regeneration instead of scarring.[10] In particular, we are interested in obtaining *in vitro* systems that resemble some aspects of a regenerative blastema, in which embryonic fibroblasts not only acquire properties such as cell dedifferentiation and multipotentiality, but also, as a whole, engage in a re-development-like program.

The self-assembling peptide RAD16-I, which forms promising three-dimensional (3D) scaffolds for tissue-engineering applications, has been used to promote growth and proliferation of multiple cell types, including chondrocytes, hepatocytes, endothelial cells, osteoblasts, and neuronal cells, as well as embryonic and somatic stem cells.[11–18] In a recent work, we demonstrated that, after culturing primary mouse embryonic fibroblasts (MEFs) into a th3D self-assembling peptide scaffold for several days, they up-regulated osteopontin (OPN) and two metalloproteinases (MMP-2 and MMP-9), known as type IV and V collagenases or the 72-kDa gelatinase A and

---

[1]Center for Biomedical Engineering, Massachusetts Institute of Technology, Boston, Massachusetts.
[2]Department of Bioengineering, Institut Químic de Sarrià—Universitat Ramon Llull, Barcelona, Spain.

92-kDa gelatinase B, respectively, characteristic of an embryonic regenerative system.[19,20] Moreover, osteoinduced MEF 3D cultures were able to develop mineralized matrix according to von Kossa staining but not 2D cultures or 3D culture controls. Alkaline phosphatase activity (ALP) was highly expressed in all 3D cultures, indicating that the 3D environment promotes ALP activity independently of the osteogenic conditions. Because the RAD16-I peptide scaffold does not contain any specific peptide-signaling motif, we define this environment as "non-instructive" from the point of view of cell receptor recognition and activation (integrin- or growth factor–like receptor), suggesting that the 3D environment *per se* promotes cellular responses. Finally, the system produced collagen type I and up-regulated the expression of runt-related transcription factor 2 (Runx2), suggesting that the cells acquire an osteoblast-like phenotype.[21] Additionally, other groups have shown previously that mesenchymal cells from bone marrow origin, mouse embryonic stem cells, and mouse embryonic fibroblasts can be differentiated into cartilage-, fat- and bone-like tissue but under specific inductive medium conditions.[22–30]

The *in vitro* cellular system we describe here undergoes a process that resembles many aspects of animal development, including cell aggregation, proliferation, migration, and tissue specification and, most importantly, morphogenesis and pattern formation.

Materials and Methods

Culture of MEFs

MEFs isolated from C57BL/6 embryos at day 14 were purchased from the American Type Culture Collection (scrc-1008; ATCC, Manassas, VA). These fibroblasts (<9th passage) were cultured in 75- or 175-cm^2 flasks in fibroblast medium (FM), which contains high-glucose Dulbecco's modified Eagle medium (DMEM; 15-013-CV; Mediatech, Manassas, VA) supplemented with 15% (v/v) fetal bovine serum (FBS; 14-501F, Lonza, Allendale, NJ), 4 mM L-glutamine (82007-322, VWR, West Chester, PA), 100 μM minimum essential medium non-essential amino acids (11140-050, Invitrogen, Carlsbad, CA), 100 U/mL penicillin, and 0.1 mg/mL streptomycin (20001, JR Scientific, Woodland, CA). In some cases, the medium was supplemented with 10 to 20 nM of insulin-like growth factor (IGF)-I (I8779 Sigma-Aldrich, St Louis, MO) and 1 to 20 nM of platelet-derived growth factor (PDGF)-BB (recombinant protein from rat, P4056 Sigma-Aldrich).

3D culture technique

For experiments with RAD16-I, MEFs (<9th passage) were trypsinized from the culture flasks, suspended in 20% sucrose (S0389, Sigma-Aldrich). Commercial 1% RAD16-I (Puramatrix, Becton & Dickinson, Franklin Lakes, NJ) was diluted with water to obtain a solution of 0.5% RAD16-I. Then equal volumes of the cell suspension in 20% sucrose and RAD16-I (1% or 0.5%) were mixed to render a final cell suspension containing 2×10^6 MEFs/mL, 10% sucrose, and either 0.25% or 0.5% of RAD16-I. Alternatively, freshly isolated MEFs were suspended in 10% sucrose and mixed with 0.5% RAD16-I in 10% sucrose, to obtain a final MEF concentration of 2×10^6 cells/mL, 10% sucrose, and 0.25% RAD16-I. This suspension

(80 μL) containing cells and RAD16-I was loaded into 9-mm-diameter cell culture inserts (PICM01250, Millipore, Billerica, MA) previously placed inside 6-well culture plates (Nunc, Rochester, NY). Then 500 μL of FM was added to the wells, outside the inserts. The medium penetrates the insert from the bottom membrane, inducing a bottom-to-top self-assembly of RAD16-I and thus the formation of a gel with MEFs suspended inside the scaffold. After the gel was formed, 500 μL of FM was added on top of the hydrogel. The FM flows trough the gel, washing out the remaining sucrose (Fig. 1A). This step was repeated two more times. Finally, 500 μL of FM was loaded inside the insert and 2.5 mL of FM in the well outside the insert. Incubation was performed at 37°C with 5% carbon dioxide, and medium was changed every 2 days.

For the experiments with agarose, the same cells were suspended in FM. This cell suspension was mixed with an equal volume of 0.5% Omnipur agarose (EM Science, Gibbstown, NJ) in 10% sucrose (S0389, Sigma-Aldrich) to obtain a final cell density of 2×10^6 cells/mL in 0.25% agarose. The cell suspension was briefly cooled until the agarose rendered the gels, which were then equilibrated in FM and incubated as described above.

For the experiments with collagen type I, the same cells were suspended in FM. Isotonic collagen 0.4% was prepared by diluting commercial collagen type I (354236, Becton & Dickinson) with filtered 10× phosphate buffered saline (PBS; 14040, Invitrogen) and sterile water (Mediatech). This solution was neutralized with sterile 1 M sodium hydroxide (Sigma-Aldrich) using phenol red (P4633, Sigma-Aldrich) as an indicator. Imediately after neutralization, equal volumes of the freshly prepared collagen solution and the cell suspension were mixed, to obtain a final cell density of 2×10^6 cells/mL in 0.2% collagen, and poured inside cell culture inserts. The suspension was heated at 37°C so that the collagen fibers formed a gel inside the inserts. Gels were cultured in FM and incubated as described above.

Differentiation assays

MEFs were cultured in the 3D hydrogels with FM for 12 days, and after that, medium was changed to differentiation medium. MEFs were maintained in differentiation medium for 21 days. As controls, MEFs were cultured for 33 days in regular fibroblast medium. For osteogenic differentiation, the medium was high-glucose DMEM with 10% FBS, 1% (v/v) penicillin streptomycin, and 4 mM L-glutamine supplemented with Lonza's osteogenic factors: 0.05 mM ascorbate, 10 mM β-glycerophosphate, 0.1 μM dexamethasone, and 20 nM 1α,25-(OH)$_2$ vitamin D3 (PT-3002, Lonza).

The medium to induce chondrogenic differentiation was provided by Cambrex (Charles City, IA) and contained basal medium supplemented with R^3-IGF, transforming growth factor beta (TGF)-β, insulin, transferrin, FBS, and gentamycin/amphotericin. The concentrations of the supplements were not available from the manufacturer.

For the adipogenic differentiation, the medium was DMEM with 10% FBS, 8 μg/mL biotin, 4 μg/mL pantothenate (C8731, Sigma-Aldrich), 0.5 mM 3-isobutyl-1-methylxanthine (I7018, Sigma-Aldrich), 1 μM dexamethasone (PT-3002, Lonza), and 10 μg/mL insulin (CC-4182, Lonza).
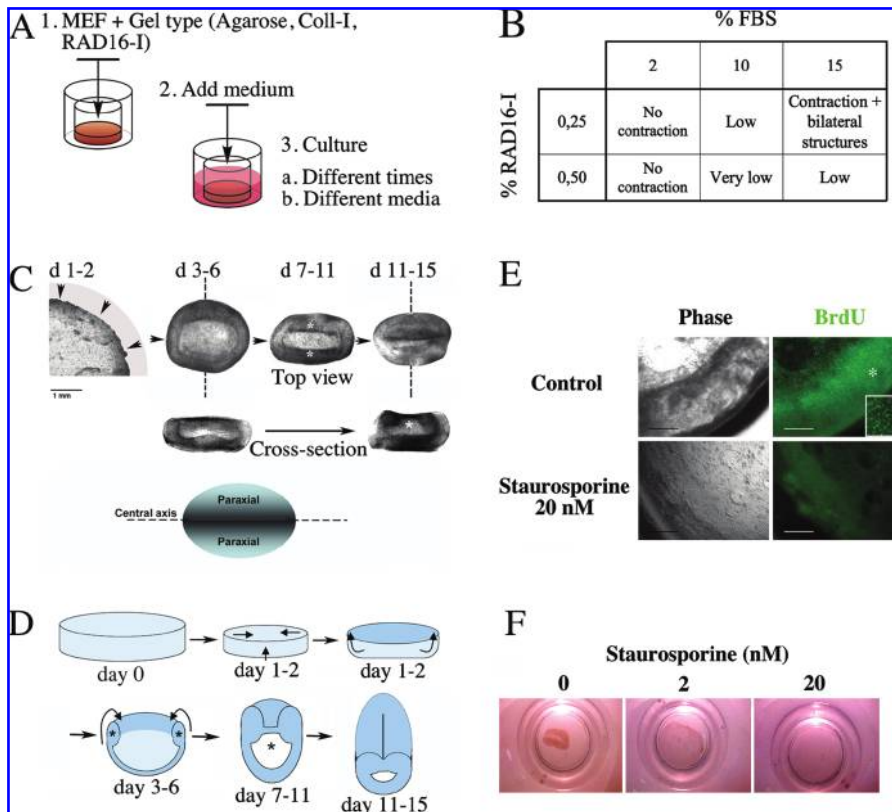
FIG. 1. Morphogenetic changes of mouse embryonic fibroblasts (MEFs) in three-dimensional (3D) cultures. (**A**) Scheme of a MEF culture and differentiation protocol. (**B**) MEFs were cultured using two different concentrations of RAD16-I to form hydrogels with different stiffness. They were cultured with three different concentrations of FBS in the fibroblast medium (FM) formulation. Rate of contraction was observed for each combination of fetal bovine serum percentage and RAD16-I concentration at day 10. Results are presented qualitatively in the table. (**C**) Main morphological process observed using visual inspection of MEFs cultured with FM in RAD16-I 0.25%. The figure shows the contraction of MEFs in the hydrogel. In 7 to 10 days a 9-mm-diameter hydrogel disk becomes a compact tissue-like cell mass of approximately 2×4 mm with bilateral patterning. Optical cross-sections depict the presence of an internal cavity. Asterisks at both sides of the structure indicate the zone of lateral contraction forces. (**D**) A model indicating the main morphological processes is presented as a guide to help understand the development of the 3D bilateral structure. The asterisks also indicate the zone of lateral force generation and the presence of a cavity developed during the morphological process and the empty cavity present in the structure. (**E**) Inhibition of the 3D bilateral structure development by cell cycle arrest induced by staurosporine. MEFs were incubated with and without staurosporine (20 nM) for 7 days. Proliferation was studied using a bromodeoxyuridine (BrdU) pulse followed by immunostaining against BrdU. Asterisk shows a close-up of the positively stained MEFs. Bar = 500 μm. (**F**) MEFs were incubated for 14 days with different concentrations of staurosporine (0, 2, 20 nM) to further analyze the effect of proliferation in the contraction phenomenon. Bar = 500 μm. Color images available online at www.liebertonline.com/ten.

Antibodies

Anti-digoxigenin (DIG) sheep polyclonal antibody (11333089001) was purchased from Roche Diagnostics (Indianapolis, IN). All other antibodies were purchased from Santa Cruz Biotechnology (Santa Cruz, CA). Anti-collagen type II (sc7764), anti-brachyury (sc17743), anti-nestin (sc21248), and anti-actin (sc1615) goat polyclonal antibodies and anti-PEBP2αA (sc10758; also known as anti-Runx2) and anti-Sox9 rabbit polyclonal antibodies were used as primary antibodies. Anti-sheep (sc2473), anti-goat (sc2020), and anti-rabbit (sc2317) donkey antibodies horseradish peroxidase (HRP)-conjugated and fluorescein isothiocyanate (FITC)-labeled chicken anti-goat (sc2988) antibodies were used as secondary antibodies.

Cell-cycle arrest assays with staurosporine

Cultures of MEFs were incubated in FM with 20 nM staurosporine (569397, Calbiochem, Gibbstown, NJ) for 7 days while controls were incubated in FM. At day 6, a pulse of bromodeoxyuridine (BrdU) was applied overnight (16 h). MEFs were fixed at day 7 and stained with an anti-BrdU FITC-conjugated mouse monoclonal antibody immunoglobulin G 1 (Becton, Dickinson and Company). To assess the dose-response effect of staurosporine on MEFs, these were

incubated with different concentrations of staurosporine (0, 2, 20 nM) for 14 days. The cell mass contraction was visually inspected during these 14 days.

Phenotype assignment

To assign osteoblastic, chondrogenic, or adipogenic phenotypes, we stained for specific elements of each phenotype. MEFs underwent the previously described differentiation protocols and were stained for calcium deposition (Von Kossa), for glycosaminoglycan (GAG) synthesis (Toluidine blue), and for lipidic accumulation (Nile Red) to assess osteogenic, chondrogenic, and adipogenic commitments, respectively. Stainings were performed as previously described. [21,31,32]

Western blot analysis

MEFs cultured in different conditions were subjected to lysis in radioimmunoprecipitation assay buffer (BP-115D, Boston Bioproducts, Worcester, MA) containing protease inhibitors (Complete-Mini, Roche Diagnostics). Two-dimensional cultured MEF lysates were used as control protein samples in osteogenic differentiation assays. Cell lysates from these cultures were subjected to NuPAGE (NP0321, Invitrogen), transferred onto a polyvinylidene

fluoride membrane (Invitrolon, Invitrogen) and blocked using tris buffered saline/Tween with 5% dry milk. PEBP2αA, collagen type II was blotted with the indicated antibodies. Actin was used as an internal protein standard.

Real-time reverse transcriptase polymerase chain reaction

mRNA was isolated from MEFs using Trizol (15596-026, Invitrogen), cultured in RAD16-I, and cultured in two dimensions (controls) at days 3, 7, 11, and 15. After degradation of cellular DNA, first-strand cDNA was synthesized from the mRNA using Taqman Reverse Transcriptase (N808-0234, Applied Biosystems, Foster City, CA). Real-time reverse transcriptase polymerase chain reaction (RT-PCR) reactions were performed in SYBR green PCR master mix (204143) using commercial primers of *Sox9* (QT00163765), Runx2 (QT00102193), Col2a1 (QT01055523), Col1a1 (QT00162204) and Col1a2 (QT01055572) (all from Qiagen, Valencia, CA). Relative gene fold variations were all determined according to the $2^{-\Delta\Delta Ct}$ method using the ribosomal unit *18S* (QT01036875, Qiagen) as a housekeeping gene.

Reverse transcriptase polymerase chain reaction

mRNA was isolated from MEFs using Trizol (15596-026, Invitrogen), cultured in RAD16-I, and cultured in two dimensions (controls), at days 3, 7, 11, and 15. After degradation of cellular DNA, 0.2 μg of mRNA was retrotranscribed with Omniscript (205111, Qiagen). The cDNA obtained was amplified using PCR (95°C 2 min, 35 cycles of 95°C 20 s, 58°C 30 s, and 68°C 30 s) using Accuprime Pfx (12344-024, Invitrogen). The primers were kindly provided by Dr David Shaywitz, Harvard University (forward: 5′-CATGTACTCTTTCTTGCTGG-3′; reverse: 5′-GGTCTCG GGAAAGCAGTGGC-3′).

GAG quantification

GAGs were quantified using 1,9-dimethyl-dimethylene blue (DMMB; 23481-50-7, Polysciences, Warrington, PA). The samples were treated overnight with pronase at 60°C and centrifuged at 14,000 g. The supernatant (40 μL) was incubated with 360 μL of a solution of DMMB (0.16% DMMB in 0.2% formic acid [251364, Sigma-Aldrich] with 2.5 mg/mL sodium formate [71541, Sigma-Aldrich]; pH 3.5) and read in a spectrophotometer with visible light ($\lambda = 535$ nm).[33] Standards for chondroitin 6 sulfate from shark cartilage (27043, Sigma-Aldrich) were used to prepare a calibration curve with values between 0 and 100 μg/mL.

Immunostaining of MEFs cultured in RAD16-I

MEFs cultured in RAD16-I for 7 to 15 days with FM were fixed with 2% PFA and washed twice with PBS 1× prepared from 10× PBS (EM-6508, VWR). Endogenous peroxidase activity was blocked with 0.3% hydrogen peroxide in PBS Tween 20 at room temperature for 30 min. Samples were blocked with 20% (v/v) FBS in PBS with 0.1% (v/v) Triton X-100 (T-9284, Sigma-Aldrich) and 1% (v/v) dimethyl sulfoxide (O81-1, Honeywell Burdick and Jackson, Morristown, NJ). Incubation with the indicated primary antibodies was per-

formed overnight at 4°C. After a 24-h washing step, samples were incubated overnight at 4°C with the secondary HRP-conjugated antibodies. Localization of proteins was finally revealed by reaction with diaminobenzidene (DAB) substrate (1718906, Roche Diagnostics).

Brachyury in situ hybridization

MEF cultures in RAD16-I were fixed at days 7, 11, and 15. *In situ* hybridization was performed whole mount and onto 14-μm slices of the tissue-like cell mass obtained after culturing. Slices were obtained by cryosectioning of the cell mass with a Leica CM 3050 S cryostat using optimal cutting temperature compound (Tissue-tek, VWR) as freezing support. The DNA probe used for the *in situ* hybridization was synthesized with the PCR DIG probe synthesis kit (11636090910, Roche Diagnostics) using primers kindly provided by D. Shaywitz (forward primer: CATGTACTCTTTCTTGCTGG; reverse primer: GGTCTCGGGAAAGCAGTGGC). The *in situ* hybridization was performed following the company's instructions for embryos and for tissue sections. After hybridization of the DIG-labeled probe, samples were immunostained for DIG using anti-DIG sheep antibody and anti-sheep HRP-conjugated antibody. Reaction with DAB substrate (1718906, Roche Diagnostics) showed the localization of brachyury mRNA.

Results

Fibroblasts suffer a morphogenetic process when cultured in RAD16-I

To understand the influence of the biomechanical and biological environments on the behavior of fibroblasts in the peptidic nanofiber scaffold RAD16-I, we varied the concentration of peptide used to form the scaffold (0.25-0.5%) and the concentration of FBS (2-15%) added to the medium (Fig. 1B). We observed that, when cultured in 0.25% RAD16-I and 15% FBS, fibroblasts engage in a morphogenetic process that renders a compact cell mass with a central axis and two thick parallel structures at each side of the central line (Fig. 1C). During the first 1 to 2 days in culture, the cells contracted the scaffold from a disk shape to a much smaller, flat, dense disk. Four to 6 days after encapsulation, the edge of the disk continued the contraction, compacting its perimeter and turning it into a wheel-like shape with a semicircular cross-section or dome shape. Next, two diametrically opposite zones at the edge of the wheel or dome started actively contracting inward, converging at the center and compressing both sides. As a consequence, the compaction of the cell masses from each side of the dome caused a merging zone that formed a "middle line." This process seemed to elongate the body along the axis, producing two large, dense paraxial structures, which resulted in a 3D bilateral assembly 11 to 15 days after encapsulation (Fig. 1C). At this point, the cell mass had gone through the main morphological changes. For better understanding, we show a schematic representation suggesting the main morphological process that the system undergoes to develop into a 3D bilateral structure (Fig. 1D). Optical cross-sections at two time points suggested the formation of an internal cavity as a result of this morphogenetic process (Fig. 1C). The final shape presents bilateral symmetry

(3D bilateral) and resembles some aspects of a vertebrate embryo undergoing axis formation. The development into a bilateral structure happened in 66% of the cases estimated after performing three independent experiments. In addition, we have found that the quality and origin of the serum affects success. To normalize those differences, we are currently testing the addition of growth factors naturally present in serum, such as PDGF and IGF-1. Preliminary results indicate that the addition of PDGF has a positive effect on the contraction and structure development (not shown). This is consistent with other investigations that show how PDGF and TGF-β enhance fibroblast-mediated collagen gel contraction.[34,35] In fact, we eventually observed the contraction of collagen type I gels mediated by MEFs (Supplemental Fig. G, H, available online at www.liebertonline.com/ten), although the formation of a bilateral structure did not accompany these contractions. Moreover, PDGF-α has been shown to promote chondrogenesis at early stages of limb development,[36] which may in some way be related to the effect that PDGF exerts on the system described here.

Proliferation is required to complete the morphogenetic changes

To further understand this phenomenon, fibroblasts, cultured as explained above, were treated with staurosporine (an inhibitor of the protein kinase C, that arrests cells in G1). Staurosporine clearly abrogated the development of the 3D bilateral structure. Figure 1E shows that no evident incorporation of BrdU was detected in staurosporine-treated samples, whereas control samples exhibited high proliferation in the outermost circle of the cell mass. Moreover, a dose-response inhibitory effect on the 3D bilateral structure development can be observed when diluted concentrations of staurosporine are added to the cultures (Fig. 1F). These results indicate that, during this morphogenetic event, the cell density increases not only because of contraction, but also because of proliferation, suggesting that the system needs to reach a critical cell mass for this phenomenon to occur.

Fibroblasts have multipotentiality and default chondrogenic commitment in RAD16-I

Fibroblasts have been shown to have multipotential capacity to differentiate into mesenchymal lineages.[21–30] To further assess the multipotentiality of MEFs, we evaluated the osteogenic, adipogenic, and chondrogenic capacities of fibroblasts cultured in the RAD16-I nanofiber scaffold, in agarose (a non-instructive 3D environment), and in collagen type I (the natural extracellular matrix (ECM) of dermal fibroblasts and bone). We questioned whether these three chemically unrelated matrices promoted the acquisition of mesenchymal potentiality, as observed before in RAD16-I.[21] Osteogenic, adipogenic, and chondrogenic phenotypes were assessed according to Von Kossa, Nile red, and toluidine blue staining, respectively. Figure 2H shows that fibroblasts undergo acute osteogenesis in all 3D environments after induction with osteogenic supplements, which the high extracellular deposition of calcium salts indicates (Fig. 2A, D and Supplemental Fig. G–K available online at www.liebertonline.com/ten). Osteogenesis occurred only with the addition of osteogenic supplements, whereas adipogenesis
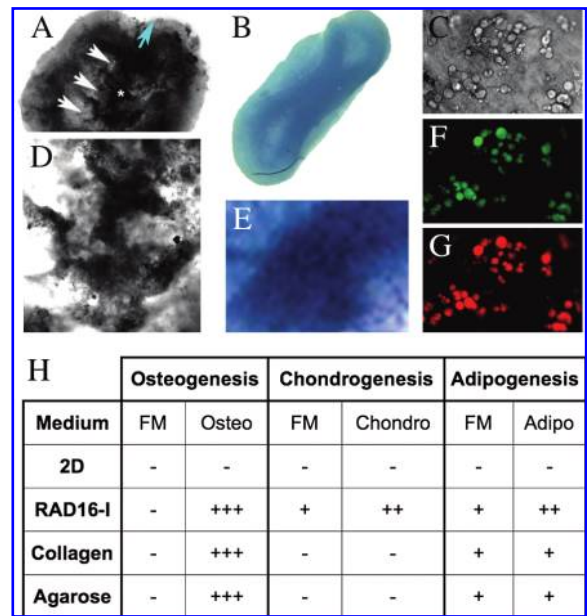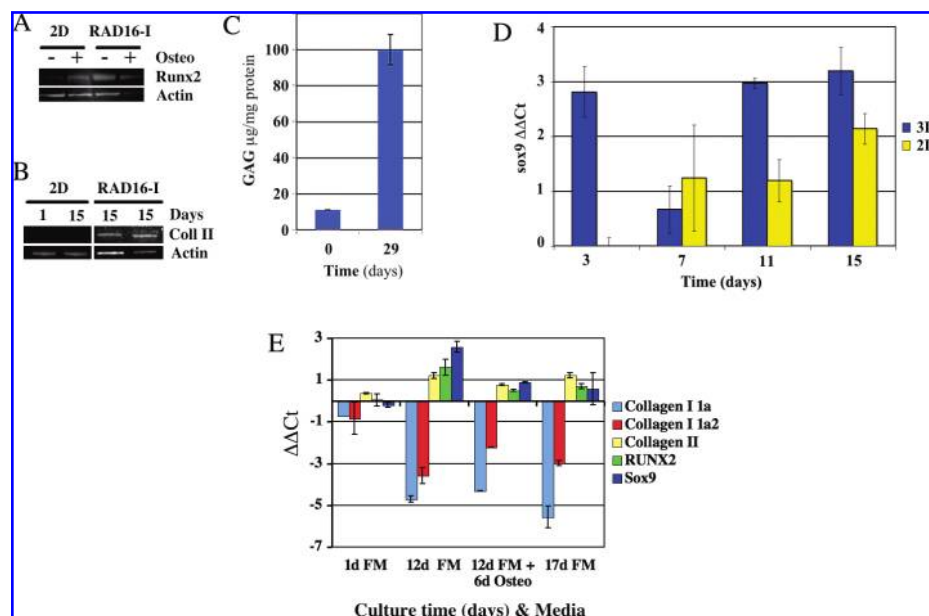

H	Osteogenesis		Chondrogenesis		Adipogenesis	
Medium	FM	Osteo	FM	Chondro	FM	Adipo
2D	-	-	-	-	-	-
RAD16-I	-	+++	+	++	+	++
Collagen	-	+++	-	-	+	+
Agarose	-	+++	-	-	+	+

FIG. 2. Multipotencial capacity of mouse embryonic fibroblasts (MEFs). (**A–J**) Phenotype of MEFs cultured in three-dimensional (3D) self-assembling peptide hydrogel. RAD16-I was assessed under different culture conditions. (**A, D**) After osteogenic induction, von Kossa staining revealed calcium deposition within the cell cultures. (**B, E**) Toluidine blue staining of MEFs showed default chondrogenic differentiation in control cultures, without need of any supplements. (**C**) Adipocytes in non-supplemented cell cultures were detectable by visual inspection. (**F, G**) Nile red staining stained the neutral lipids of these adipocytes (**F,** fluorescein filter, green; **G,** rhodamine filter, red). For space reasons, pictures of differentiation results in 2D-culture vontrols and 3D cultures in agarose and collagen type I systems are presented in the Supplemental Figure, available online at www .liebertonline.com/ten. (**H**) Osteogenic, chondrogenic, and adipogenic differentiation assays were performed as indicated on MEFs, and three different stainings were used to identify cell commitments: Von Kossa staining was used to identify osteogenic, toludine blue staining for chondrogenic, and Nile red staining for adipogenic differentiations. For reference level of differentiation: − (negative), + (slightly positive), ++ (positive), +++ (highly positive). The table shows that MEFs can acquire osteogenic and adipogenic phenotypes in three dimensions, but only in RAD16-I can they undergo natural chondrogenesis. Color images available online at www.liebertonline.com/ten.

occurred with (not shown) and without adipogenic supplements (Fig. 2C, F, G). Chondrogenesis arose only in the self-assembling peptide scaffolds, with (Supplemental Fig. C) and without chondrogenic supplements (Fig. 2B, E and Supplemental Fig. F), indicating that there is some relationship between chondrogenesis and the biomechanical and non-instructive characteristics of RAD16-I.

Western blot analysis revealed that the pre-osteogenic transcription factor Runx2 was more upregulated in MEFs cultured without inductive supplements in the nanofiber scaffold RAD16-I than expression levels of the same cells cultured in 2D (Fig. 3A). Then the addition of differentiating supplements caused an upregulation of the expression of Runx2 in 2D cultures, whereas in 3D cultures, Runx2

FIG. 3. Molecular characterization of the mesodermal induction process. (**A**) Runt-related transcription factor 2 (Runx2) expression was analyzed according to Western blot in mouse embryonic fibroblasts (MEFs) cultured in RAD16-I after the osteogenic differentiation protocol previously described. Two-dimensional (2D) cultures were used as controls. (**B**) Collagen type II was analyzed according to Western blot in MEFs cultured in flask cultures (2D) after 1 and 15 days in culture and in RAD16-I (3D) after 15 days in culture with fibroblast medium (FM). (**C**) Glycosaminoglycans (GAGs) from 3D self-assembling peptide cultures of MEF at days 0 and 29 were quantified with 1,9-dimethyl-dimethyleneblue using chondroitin sulfate as the standard. (**D**) Real-time reverse transcriptase polymerase chain reaction (RT-PCR) of Sox9 transcription factor. Total mRNA was isolated from MEFs cultured in RAD16-I with FM and from 2D controls after days 3, 7, 11, and 15. (**E**) Real-ime RT-PCR of collagen type I, collagen type II, Runx2, and Sox9. Total mRNA was isolated from MEFs cultured in FM for 1, 12, and 17 days and cultured for 12 days in FM followed by 6 days in osteogenic medium. Color images available online at www.liebertonline.com/ten.

remained constant. Runx2 is a transcription factor present in hypertrophic chondrocytes (which mineralize the ECM only when osteochondral ossification begins[37,38]) and normally during osteogenesis.[39] In our system, mineralization happens in 3D cultures only in the presence of osteogenic supplements. Moreover, the expression of Runx2 is upregulated in 3D cultures with and without osteogenic induction, suggesting that, in our system, fibroblasts develop by default all the way to hypertrophic chondrocytes but not to osteoblasts. This implies that other factors known to induce osteogenesis in hypertrophic chondrocytes are not present in our system (e.g., the vascular cross-talk signaling). two-dimensional cultures of MEFs induced with osteogenic factors upregulated the expression of Runx2 but failed to mineralize the matrix, suggesting that, in the 3D system, in addition to the upregulation of Runx2, there must be other factors that determine the osteogenic commitment.

Default chondrogenic commitment of MEFs was observed using Western blot analysis of collagen type II (Fig. 3B). Real-time RT-PCR of the transcription factor Sox9 presented a pattern of expression with two peaks of upregulation, one at day 3 and the second at day 11, separated by a down-regulation zone at day 7 (Fig. 3D). These changes in expression correlate well with the morphogenic changes previously described. For instance, at day 3, the structure contraction is isotropic, continuing until day 6 (Fig. 1C). At days 7 to 11, the structure starts bilateral contractions, suggesting a dramatic change in the morphogenic process that might affect the expression of Sox9. After several days (11-15 days), the morphogenetic changes finish, and the bilateral structure upregulates Sox9 again although localized at the paraxial zone (Fig. 4D). In 2D cultures, Sox9 upregulation was less intense, with a gradual increase over time (Fig. 3D). To further understand the gene expression of the 3D system during default

chondrogenesis and after osteogenic induction, we evaluated the expression of the transcription factors Runx2 and Sox9, as well as ECM proteins such as collagen type Ia1, collagen type Ia2 and collagen type II using real-time RT-PCR. Results show that, at day 12, when the 3D bilateral structure closes, Sox9, Runx2, and collagen type II are more over-expressed than MEFs cultured in flasks (Fig. 3E). At the same time, the synthesis of collagen type I is strongly down-regulated (Fig. 3E), meaning that MEFs cultured in RAD16-I gradually loose their fibroblastic phenotype (characterized by the synthesis of collagen type I) and become chondrocyte-like cells (expressing collagen type II, Runx2, and high levels of Sox9). Then, 5 to 6 days after osteogenic induction, the expression levels of collagen type II, Runx2, and Sox9 decrease (Fig. 3E). Collagen type II remains constant after 17 days of culture without osteogenic supplements (Fig. 3E), consistent with the Western blots (Fig. 3B) and immunohistochemistry (Fig. 4E). The down-regulation of Sox9 and Runx2 appear to be independent of the presence of osteogenic induction (Fig. 3E). In the presence of osteogenic induction, a slightly greater upregulation of collagen type I 1a2, but not collagen type I 1a, can be observed than under conditions without differentiating factors (Fig. 3E).

Finally, MEFs synthesized GAGs when cultured in RAD16-I with FM, confirming the default cartilaginous commitment of these fibroblasts (Fig. 3C). Moreover, when we stained the 3D bilateral structures with Toluidine blue for GAGs, two positive zones parallel to the central axis were detected, suggesting the formation of a paraxial cartilage-like tissue (Fig. 4C). These results confirm the presence of a glycosylated proteoglycan that could be, for example, aggrecan or perlecan or a mix of them. Perlecan is more consistent with the appearance of cartilage during early development.[40]
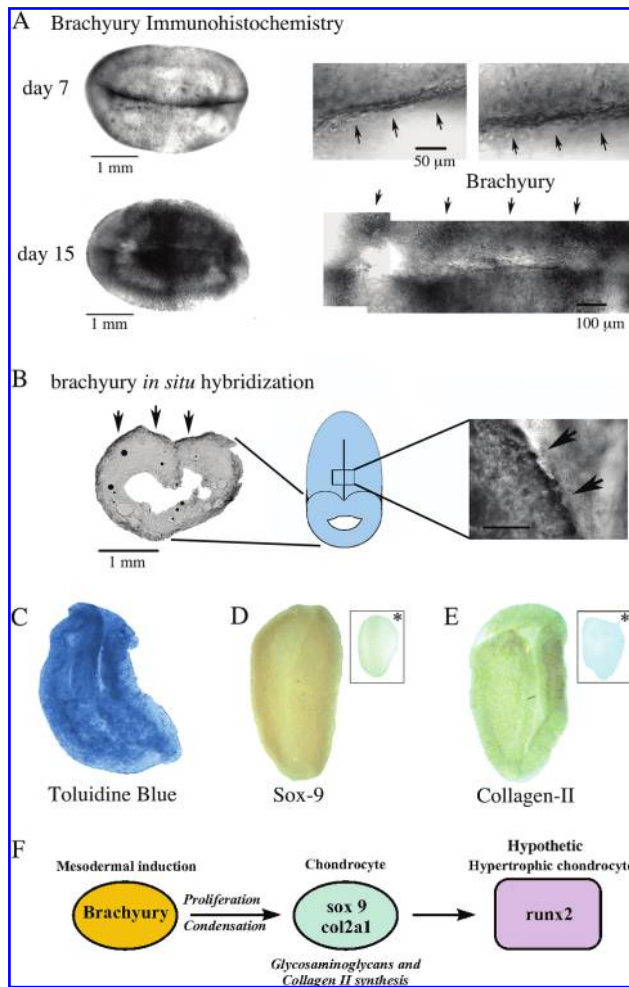
FIG. 4. Morphogenesis correlates with pattern formation. (**A**) Brachyury immunostaining of mouse embryonic fibroblasts (MEFs) cultured in RAD16-I with fibroblast medium (FM) for 7 and 15 days. Whole-mount immunostaining showed the localization of brachyury expression in the three-dimensional (3D) bilateral structures of 7 and 15 days. Pictures on the right represent a magnification of the zones where brachyury is expressed for better view of the stainings. Brachyury is first expressed in the central axis and then in the paraxial zones. Clusters of expression can be observed at this moment (day 15). (**B**) *In situ* hybridization was also performed to observe the localization of brachyury. Totally contracted samples (15 days of culture in FM) were fixed and cryosectioned as indicated. *In situ* hybridization over a 14-μm slice of the 3D bilateral structure showed that brachyury is expressed in the external paraxial zone. Shortly after closure of the central axis (11 days of culture), the cell mass was fixed. Whole-mount *in situ* hybridization showed the localization of brachyury within the cell mass. (**C–E**) Toluidine blue staining and immunostaining for Sox9 and collagen type II were performed on MEFs cultured for 15 days in FM. Asterisks show control samples immunostained using only the secondary horseradish peroxidase–conjugated antibody. These three stainings show that chondrogenesis occurs only in the two paraxial zones next to the symmetrical axis. (**F**) Finally, we propose a mesodermal commitment and cartilage-like tissue development model in our system based in the molecular markers detected. Color images available online at www.liebertonline.com/ten.

Pattern formation accompanies symmetry appearance

To provide more insight into the possible patterned chondrogenesis, we studied the expression of brachyury, one of the first mesodermal-specific transcription factors that is expressed in the presumptive notochord and in the early mesoderm.[41–43] With different culture times, brachyury stained positive according to immunohistochemistry first (day 7) in the central axis and then (day 15) in the entire paraxial zones of the 3D bilateral structure (Fig. 4A). The expression of brachyury was confirmed using regular RT-PCR (see Supplemental Fig., available online at www.liebertonline.com/ten) and its localization was visualized using *in situ* hybridization. Probes were prepared with the same primers used for regular RT-PCR, and after the staining, we observed that the brachyury mRNA was mainly expressed at the same zone detected using immunohistochemistry, confirming the expression of this early-organizer transcription factor in the 3D bilateral structures (Fig. 4B). Staining of a cross-section of this structure depicts the clear presence of an internal cavity, observed before in Figure 1, and the expression of brachyury at the external paraxial zone (Fig. 4B).

It is also known that the expression of some set of transcription factors, such as Sox9 precedes organized chondrogenic commitment. Thus, we studied the presence and localization of the transcription factor Sox9, a key transcription factor in early chondrogenesis,[44] and immunostaining showed that Sox9 is mainly expressed in the paraxial zones next to the symmetrical axis (Fig. 4D). Finally, the synthesis of the key ECM component of cartilage collagen type II was assessed by immunostaining of the 3D bilateral structures cultured for 15 days in FM. Results showed that collagen type II is also expressed at the paraxial zones next to the central symmetrical axis (Fig. 4E).

Discussion

Fibroblasts are known to be responsible for many regenerating events. A significant example is the regeneration of amputated limbs in amphibians, where fibroblasts generate a set of undifferentiated cells called a blastema that is capable of proliferating and rebuilding the new limb.[5–9] Previously, fibroblasts cultured *in vitro* have also shown multipotential capacity[21,30] and have reproduced the mesenchymal condensation in micromass cultures.[45,46] Nevertheless, it is still not clear what mechanism drives fibroblasts to this multipotential state and which is the exact phenotype of these undifferentiated fibroblasts.[6,7] We hypothesize that the biomechanical and non-instructive properties of their environment are key for fibroblasts to have the ability to acquire a less differentiated phenotype that allows them to render most of the cell types of the mesodermal germ line.

Our work suggests that any 3D environment, under the culture conditions tested, and regardless of its chemical nature (self-assembling peptide nanofiber, polysaccharide, or protein matrix), is sufficient to promote dedifferentiation of MEFs into a multipotent mesenchymal progenitor-like cell (Fig. 2). This opens the possibility that the cells "sense" the environment, reprogramming them into a multipotent progenitor. Osteogenic commitment of this progenitor cell in 3D environments occurs only after an osteogenic differentiation protocol, which is evidenced by the deposition of Ca^{2+} (Fig. 2A, D) and the expression of Runx2 (Fig. 3A) (also known as

core binding factor, Cbfa1 and Osf2), positively regulates the expression of specific genes during early osteoinduction in hypertrophyc chondrocytes, suggesting that these cells have acquired such a phenotype. Nevertheless, the specific characteristics of the 3D environment, such as the biomechanical and non-instructive properties, as well as the permissiveness toward cell-to-cell interactions, will provide cells with more or less multipotential capacity. This is clear in the case of RAD16-I, where cells acquired chondrogenic potential by default, as well as the unexpected morphogenetic process here described, suggesting that. in this case. the unique conditions obtained allowed the cells to proceed into a more-organized or *emerging* state: cellular self-organization. We cannot exclude that diffusion and oxygen gradients may play an important role in the morphogenic process. It is not casual that the final wall thickness of the 3D bilateral structure does not exceed approximately $500\,\mu m$, which is the diffusion limit of oxygen in non-vascularized tissues. Moreover, we also speculate that the low oxygen concentration at the inner-most part of the structure could favor the development of paraxial cartilage-like tissue. Notwithstanding this, the gene and protein expression profiles that accompany this morphogenetic event strongly suggest that there is a certain patterning involved.

For instance, these fibroblasts undergo spontaneous adipogenesis in three dimensions (Fig. 2C, F, G), but only in the self-assembling peptide do MEFs begin a default chondrogenic differentiation process, presumably by creating a special cell microenvironment (Fig. 2B, E, 4C). This could be due to the chemical differences between these three scaffolds. The polysacharide (agarose) has shown low interaction with fibroblasts, as well as poor contracting capacity; cells adopt a spherical shape and have little movement inside the scaffold (Supplemental Fig.). Instead, collagen type I is the natural ECM component of the dermis and bone, ensuring high interaction between the cells and the matrix. Furthermore, this material could be instructive in guiding embryonic fibroblasts into these lineages, preventing them from spontaneous differentiation into a chondrogenic lineage (Fig. 2H). Finally, viscoelastic studies with RAD16-I (at different concentrations) over the years have shown that RAD16-I peptide concentrations between 1.7 and 2.8 mg/mL have a G′ (elastic modulus) of 120 and 400 Pa, respectively. In our system, we used final peptide concentrations of approximately 2.5 mg/mL, with a G′ close to 370 Pa, a similar G′ to that of extracellular collagen type I matrices, suggesting that the microenvironment in RAD16-I gels is mechanically similar to the natural ECM of fibroblasts. Therefore, because self-assembling peptide scaffolds lack inherent instructive capacity and have the same biomechanical properties as natural fibroblast ECMs, the default chondrogenesis here described could mean that mouse embryonic fibroblasts can naturally undergo chondrogenic lineage differentiation under the mentioned culture conditions (Fig. 2H). Not only does the self-assembling peptide allow spontaneous chondrogenesis, but it also promotes, under certain conditions, a unique *in vitro* cellular self-organization that resembles early embryonic stages (Fig. 1C). Furthermore, similar to what has been observed in animal development, the progression of this morphogenesis is dependent on proliferation, as evidenced by the effects of staurosporine on system contraction (Fig. 1E, F). It was also noticed that less initial concentration of MEFs (5×10^5 cells/mL) within the RAD16-I resulted in

three fold the contraction time of the cell mass and failed to render bilaterality (results not shown). These results indicate that proliferation seems to have a close relationship with the spontaneous chondrogenic differentiation of MEFs, similar to the relationship between embryonic mesenchymal condensation and chondrogenesis within the pre-skeletal tissue. Altogether, as a consequence of the biomechanical and non-instructive properties of RAD16-I scaffolds, we can speculate that the contraction produced during the morphogenetic process could reproduce a mesenchymal condensation phenomenon that explains the default chondrogenic pathway. Hence, the localized natural chondrogenic induction could be the result of mesenchymal condensation and differentiation under the control of an organized process that directs tissue-like patterning. This is a significant difference from the mesenchymal potential of fibroblasts in high-density micromass cultures, because in these cultures, although fibroblasts reproduce mesenchymal condensation and show default chondrogenic commitment, no self-organization is observed.[45,46]

We have also showed, using immunohistochemistry and *in situ* hybridization, that the expression of brachyury, and its localization in this system, is highly related to the formation of the 3D bilaterality (Fig. 4A, B). First, brachyury is expressed in a mid-line zone of the structure, to further spread to both sides of the central axis, suggesting that mesodermal commitment continues advancing toward both sides of the cell mass.

The expression of Sox9 and the synthesis of collagen type II and GAGs also indicated tpontaneous chondrogenesis during this morphogenic development (Fig. 3C, D and 4C–E). Sox9, Runx2, and collagen type II, like brachyury, showed a profile of expression strongly related to morphogenic development, although it remains unknown how the morphological changes proceeded as function of the expression of these genes. Loss-of-function experiments would elucidate the exact relationship between gene expression and the morphogenic process. Sox9 was strongly over-expressed at two time-points during the morphogenetic event related to physical changes: strong isotropic contraction (day 3) and closure of the 3D bilaterality (day 11). The over-expression of Sox9 could be explained as a requirement for the cells to condense, as happens in mesenchymal condensation. Then, after closure of the cellular structure, the expression of Sox9 is upregulated again and correlates with the synthesis of collagen type II, meaning that, at this moment, chondrogenesis is taking place. Runx2 and Collagen type II expression levels are upregulated after closure of the structure and are maintained thereafter.

From the mechanical point of view, from the experiments with different concentrations of RAD16-I (Fig. 1B), it seems clear that the biomechanics in early stages govern the process, at least in the first days of isotropic contraction, when cells form a network and contract the system. It is likely that, at early stages of this phenomenon, some genetic programs start taking control of the evolution of the system. At the time when the lateral contractions start to happen, some genetic programs are already "ruling" the process. We are now focusing on early organizer genes to see whether they are co-localized where and when bilateral contractions take place.

Altogether, we observed that the system undergoes organized contraction, developing into a bilateral shape structure

with a central axis, called 3D bilateral structure, resembling an early vertebrate embryonic stage. These remarkable morphological changes suggest that the system might be engaging in a cellular self-organization process. We speculate that the initial conditions we provide to the cells (3D culture of MEFs in self-assembling peptide scaffolds) recapitulates cellular and morphological changes of tissues undergoing development (proliferation, migration, and condensation) and the expression pattern of early embryonic genes (organizers and tissue-specific genes) (Fig. 4F). Moreover, the process ends in the production of specific tissues, such as patterned paraxial cartilage-like tissue. Most importantly, a group of differentiated cells under special "environmental conditions" can proceed to a self-organization process, characteristic of systems undergoing development.

In conclusion, the system we described here can be used to culture cells carrying specific mutations or transgenic genes and to obtain 3D bilateral structures that recreate certain morphogenetic processes without the use of pregnant females and their embryos. In future work, other cell sources such as dermal fibroblasts from amphibians and other mammals, including adult humans, will be tested to see whether this particular self-organization phenomenon is common in other metazoans.

Acknowledgments

References

1. Raper, K.B. Pseudoplasmodium formation and organization of Dictyostelium discoideum. J Elisha Mitchell Sci Soc **56,** 241, 1940.

2. Knecht, D.A., Fuller, D.L. and Loomis, W.F. Surface glycoprotein, gp24, involved in early adhesion of Dictyostelium discoideum. Dev Biol **121,** 277, 1987.

3. Hallmann, A. Morphogenesis in the family Volvocaceae: different tactics for turning an embryo right-side out. Protist **157,** 445, 2006.

4. Michod, R.E. Evolution of individuality during the transition from unicellular to multicellular life. Proc Natl Acad Sci U S A **104 Suppl 1,** 8613, 2007.

5. Gardiner, D.M. and Bryant, S.V. The tetrapod limb. In: Ferretti P, and Géraudie J. Cellular and Molecular Basis of Regeneration: From Invertebrates to Humans Chichester, UK: John Wiley & Sons, Ltd., 1998, pp. 187-205.

6. Endo, T., Bryant, S.V. and Gardiner, D.M. A stepwise model system for limb regeneration. Dev Biol **270,** 135, 2004.

7. Brockes, J.P. and Kumar, A. Appendage regeneration in adult vertebrates and implications for regenerative medicine. Science **310,** 1919, 2005.

8. Mullen, L.M., Bryant, S.V., Torok, M.A., Blumberg, B. and Gardiner, D.M. Nerve dependency of regeneration: the role of distal-less and FGF signaling in amphibian limb regeneration. Development **122,** 3487, 1996.

9. Zenjari, C., Boilly, B., Hondermarck, H. and Boilly-Marer, Y. Nerve-blastema interactions induce fibroblast growth factor-1 release during limb regeneration in Pleurodeles waltl. Dev Growth Differ **39,** 15, 1997.

10. Hopkinson-Woolley, J., Hughes, D., Gordon, S. and Martin, P. Macrophage recruitment during limb development and wound healing in the embryonic and fetal mouse. J Cell Sci **107,** 1159, 1994.

11. Zhang, S., Holmes, T.C., DiPersio, C.M., Hynes, R.O., Su, X. and Rich, A. Self-complementary oligopeptide matrices support mammalian cell attachment. Biomaterials **16,** 1385, 1995.

12. Zhang, S. and Rich, A. Direct conversion of an oligopeptide from a beta-sheet to an alpha-helix: a model for amyloid formation. Proc Natl Acad Sci U S A **94,** 23, 1997.

13. Kisiday, J., Jin, M., Kurz, B., Hung, H., Semino, C., Zhang, S. and Grodzinsky, A.J. Self-assembling peptide hydrogel fosters chondrocyte extracellular matrix production and cell division: implications for cartilage tissue repair. Proc Natl Acad Sci U S A **99,** 9996, 2002.

14. Semino, C.E., Merok, J.R., Crane, G.G., Panagiotakos, G. and Zhang, S. Functional differentiation of hepatocyte-like spheroid structures from putative liver progenitor cells in three-dimensional peptide scaffolds. Differentiation **71,** 262, 2003.

15. Semino, C.E., Kasahara, J., Hayashi, Y. and Zhang, S. Entrapment of migrating hippocampal neural cells in three-dimensional peptide nanofiber scaffold. Tissue Eng **10,** 643, 2004.

16. Narmoneva, D.A., Vukmirovic, R., Davis, M.E., Kamm, R.D. and Lee, R.T. Endothelial cells promote cardiac myocyte survival and spatial reorganization: implications for cardiac regeneration. Circulation **110,** 962, 2004.

17. Genove, E., Shen, C., Zhang, S. and Semino, C.E. The effect of functionalized self-assembling peptide scaffolds on human aortic endothelial cell function. Biomaterials **26,** 3341, 2005.

18. Bokhari, M.A., Akay, G., Zhang, S. and Birch, M.A. The enhancement of osteoblast growth and differentiation *in vitro* on a peptide hydrogel-polyHIPE polymer hybrid material. Biomaterials **26,** 5198, 2005.

19. Werb, Z. ECM and cell surface proteolysis: regulating cellular ecology. Cell **91,** 439, 1997.

20. Gourevitch, D., Clark, L., Chen, P., Seitz, A., Samulewicz, S.J. and Heber-Katz, E. Matrix metalloproteinase activity correlates with blastema formation in the regenerating MRL mouse ear hole model. Dev Dyn **226,** 377, 2003.

21. Garreta, E., Genove, E., Borros, S. and Semino, C.E. Osteogenic differentiation of mouse embryonic stem cells and mouse embryonic fibroblasts in a three-dimensional self-assembling peptide scaffold. Tissue Eng **12,** 2215, 2006.

22. Ducy, P., Zhang, R., Geoffroy, V., Ridall, A.L. and Karsenty, G. Osf2/Cbfa1: a transcriptional activator of osteoblast differentiation. Cell **89,** 747, 1997.

23. Stein, G.S. and Lian, J.B. Molecular mechanisms mediating proliferation/differentiation interrelationships during progressive development of the osteoblast phenotype. Endocr Rev **14,** 424, 1993.

24. Jaiswal, N., Haynesworth, S.E., Caplan, A.I. and Bruder, S.P. Osteogenic differentiation of purified, culture-expanded human mesenchymal stem cells *in vitro*. J Cell Biochem **64,** 295, 1997.

25. Pittenger, M.F., Mackay, A.M., Beck, S.C., Jaiswal, R.K., Douglas, R., Mosca, J.D., Moorman, M.A., Simonetti, D.W., Craig, S. and Marshak, D.R. Multilineage potential of adult human mesenchymal stem cells. Science **284,** 143, 1999.

26. Buttery, L.D., Bourne, S., Xynos, J.D., Wood, H., Hughes, F.J., Hughes, S.P., Episkopou, V. and Polak, J.M. Differentiation of osteoblasts and *in vitro* bone formation from murine embryonic stem cells. Tissue Eng **7,** 89, 2001.

27. Tai, G., Polak, J.M., Bishop, A.E., Christodoulou, I. and Buttery, L.D. Differentiation of osteoblasts from murine embryonic stem cells by overexpression of the transcriptional factor osterix. Tissue Eng **10,** 1456, 2004.

28. Bielby, R.C., Boccaccini, A.R., Polak, J.M. and Buttery, L.D. *In vitro* differentiation and *in vivo* mineralization of osteogenic cells derived from human embryonic stem cells. Tissue Eng **10,** 1518, 2004.

29. Cao, T., Heng, B.C., Ye, C.P., Liu, H., Toh, W.S., Robson, P., Li, P., Hong, Y.H. and Stanton, L.W. Osteogenic differentiation within intact human embryoid bodies result in a marked increase in osteocalcin secretion after 12 days of *in vitro* culture, and formation of morphologically distinct nodule-like structures. Tissue Cell **37,** 325, 2005.

30. Lengner, C.J., Lepper, C., van Wijnen, A.J., Stein, J.L., Stein, G.S. and Lian, J.B. Primary mouse embryonic fibroblasts: a model of mesenchymal cartilage formation. J Cell Physiol **200,** 327, 2004.

31. Tchoukalova, Y.D., Harteneck, D.A., Karwoski, R.A., Tarara, J. and Jensen, M.D. A quick, reliable, and automated method for fat cell sizing. J Lipid Res **44,** 1795, 2003.

32. Geyer, G. and Linss, W. Toluidine blue staining of cartilage proteoglycan subunits. Acta Histochem **61,** 127, 1978.

33. zur Nieden, N.I., Kempka, G., Rancourt, D.E. and Ahr, H.J. Induction of chondro-, osteo- and adipogenesis in embryonic stem cells by bone morphogenetic protein-2: effect of cofactors on differentiating lineages. BMC Dev Biol **5,** 1, 2005.

34. Tingstrom, A., Heldin, C.H., and Rubin, K. Regulation of fibroblast-mediated collagen gel contraction by platelet-derived growth factor, interleukin-1 alpha and transforming growth factor-beta 1. J Cell Sci **102 (Pt 2),** 315, 1992.

35. Liu, X., Wen, F.Q., Kobayashi, T., Abe, S., Fang, Q., Piek, E., Bottinger, E.P., Roberts, A.B., and Rennard, S.I. Smad3 mediates the TGF-beta-induced contraction of type I collagen gels by mouse embryo fibroblasts. Cell Motil Cytoskeleton **54,** 248, 2003.

36. Ataliotis, P. Platelet-derived growth factor A modulates limb chondrogenesis both *in vivo* and *in vitro*. Mech Dev **94,** 13, 2000.

37. Shen, G. and Darendeliler, M.A. The adaptive remodeling of condylar cartilage—a transition from chondrogenesis to osteogenesis. J Dent Res **84,** 691, 2005.

38. Goldring, M.B., Tsuchimochi, K. and Ijiri, K. The control of chondrogenesis. J Cell Biochem **97,** 33, 2006.

39. Olsen, B.R., Reginato, A.M. and Wang, W. Bone development. Annu Rev Cell Dev Biol **16,** 191, 2000.

40. French, M.M., Smith, S.E., Akanbi, K., Sanford, T., Hecht, J., Farach-Carson, M.C. and Carson, D.D. Expression of the heparan sulfate proteoglycan, perlecan, during mouse embryogenesis and perlecan chondrogenic activity *in vitro*. J Cell Biol **145,** 1103, 1999.

41. Technau, U. Brachyury, the blastopore and the evolution of the mesoderm. Bioessays **23,** 788, 2001.

42. Stemple, D.L. Structure and function of the notochord: an essential organ for chordate development. Development **132,** 2503, 2005.

43. Kispert, A., Ortner, H., Cooke, J. and Herrmann, B.G. The chick Brachyury gene: developmental expression pattern and response to axial induction by localized activin. Dev Biol **168,** 406, 1995.

44. Kawakami, Y., Rodriguez-Leon, J. and Belmonte, J.C. The role of TGFbetas and Sox9 during limb chondrogenesis. Curr Opin Cell Biol **18,** 723, 2006.

45. Denker, A.E., Haas, A.R., Nicoll, S.B. and Tuan, R.S. Chondrogenic differentiation of murine C3H10T1/2 multipotential mesenchymal cells: I. Stimulation by bone morphogenetic protein-2 in high-density micromass cultures. Differentiation **64,** 67, 1999.

46. Gomes, R.R.J., Joshi, S.S., Farach-Carson, M.C. and Carson, D.D. Ribozyme-mediated perlecan knockdown impairs chondrogenic differentiation of C3H10T1/2 fibroblasts. Differentiation **74,** 53, 2006.

The effect of self-assembling peptide nanofiber scaffolds on mouse embryonic fibroblast implantation and proliferation

Irene R. Dégano [a,b,1], Lluís Quintana [c,1], Marta Vilalta [a,b], David Horna [c], Nuria Rubio [a,b],
Salvador Borrós [c], Carlos Semino [c,d,e], Jerónimo Blanco [a,b,*]

[a] CIBER de Bioingeniería, Biomateriales y Nanomedicina (CIBER-BBN), Spain
[b] Cardiovascular Research Center (CSIC-ICCC), Hospital de la Santa Creu i Sant Pau, Pavelló del Convent, Barcelona 08025, Spain
[c] Departamento de Bioingeniería, Institut Químic de Sarrià, Universitat Ramon Llull, Barcelona, Spain
[d] Center for Biomedical Engineering, Biological Engineering Division, Massachusetts Institute of Technology, NE47-383, Cambridge, MA, USA
[e] Translational Centre for Regenerative Medicine, Leipzig University, Germany

ARTICLE INFO

ABSTRACT

Development of new materials for tissue engineering can be facilitated by the capacity to efficiently monitor in vivo the survival, proliferation and differentiation behaviour of cells implanted in different target tissues. We present here the application of a previously developed platform that allows to monitor in real time the survival and proliferative behaviour of implanted cells in two anatomical sites: subcutaneous and intramuscular. Basically, the system is based on the use of a non-invasive bioluminescence imaging (BLI) technique to detect luciferase expressing C57BL/6 cells, mouse embryonic fibroblasts, seeded in two sets of scaffolds: 1, a RAD16-I self-assembling peptide nanofiber matrix and 2, a composite consisted of the same RAD16-I nanofibers contained into a microporous biorubber scaffold. Interestingly, our results indicated considerable differences in the behaviour of implanted cells in each scaffold type. We observed that the self-assembling peptide scaffold alone foster cell survival and promotes cell proliferation where the composite scaffold not. Since self-assembling peptide scaffolds presents value stiffness proximal to the implanted tissues it is suggestive to think that harder materials will provide a physical constriction for cells to proliferate as well as mechanical discontinuity. We therefore propose that it is important to close match the implantation environment with the cell/material constructs in order to obtain the best response of the cells, illustrating the convenience of this strategy for the development of new tissue engineering platforms.

© 2008 Elsevier Ltd. All rights reserved.

1. Introduction

Tissue engineering focuses on the use of cells, biomaterials and combinations of both [1] to repair and replace damaged tissues. Beginning in 1950s, surgeons have been using a wide variety of materials for medical applications [2]. Many researchers have developed scaffolds that attempt to mimic natural cell environments in combination with suitable cell types for tissue regeneration. To date, a vast spectrum of biomaterials has been developed using polysaccharides, polypeptides, proteoglycans, lipids, ceramics, biopolymers, as well as complex extracellular matrix components, also in combination with the above [2].

Since in most of the tissues cells are in three-dimensional (3D) environments subjected to special biophysical and biomechanical conditions it is likely that scaffolds mimicking the natural milieu would enhance cell growth and differentiation and therefore they could be a better choice for biomedical applications. For instance, calcium phosphates have attracted much attention as biomaterials within the past 20 years due to their ability to facilitate interfacial bonding with bone. In particular, crystalline and semi-crystalline hydroxyapatite (HA) have been recognized as a good bone substitute candidate due to its chemical similarity with naturally calcified tissues, good bioactivity and osteoconductivity [3–7]. Self-assembly of collagen I molecules generates the dermal matrix-equivalent, a soft natural scaffold with pore sizes in the range of 50–200 nm [8]. Engineering of biomaterials for soft tissue regeneration are taking advantage of self-assembling peptides with similar mechanical behaviour to those of natural collagen scaffolds [9–11] and has provided commercially available synthetic self-assembling peptides for tissue culture. RAD16-I [12], one of such materials, is a AcN-(RADA)$_4$-CONH$_2$ peptide that self-assembles to form

* Corresponding author. Cardiovascular Research Center (CSIC-ICCC), Hospital de la Santa Creu i Sant Pau, Pavelló del Convent, Barcelona 08025, Spain. Tel.: +34 935565905; fax: +34 935565559.
E-mail address: jblancof@csic-iccc.org (J. Blanco).
[1] Both authors contributed equally to the manuscript.

a three-dimensional hydrogel structure mimicking the extracellular matrix. This peptide has been successfully used to grow hepatocytes, neuronal tissue, chondrocytes, endothelial cells, mesenchymal stem cells, fibroblasts and other cell types [13–18]. The material has also been shown to be non-toxic *in vivo* and to promote the regeneration of bone tissue in calvarial bone defects [19,20]. However, an important drawback of RAD16-I is its tendency to break under mechanical stress. In order to improve the mechanical strength of RAD16-I, we have used a composite material consisting of RAD16-I and a previously described porous biorubber scaffold [21]. Biorubbers are elastomeric, rubber like polymers, with additional biocompatible features [22]. The distinctive characteristic of the proposed composite material is a three-dimensional RAD16-I nanofiber scaffold environment for cells supported in a microporous biorubber scaffold that provides mechanical strength.

Bioluminescence imaging (BLI) procedures [23,24], based on the detection of visible light photons generated by luciferase reporters expressed by implanted cells, provide an excellent method to asses the viability of cell-scaffold combinations [25,26]. *Photinus pyralis* luciferase (PLuc) catalyzes the oxidation of luciferin in the presence of ATP and coenzyme A, producing light and CO_2. Due to an almost total absence of competing luminescent reactions in mammalian tissues [27], the existence of highly sensitive light measuring instruments and the lack of requirement for post-translational modifications, PLuc is a very convenient and quantifiable cell reporter.

In the present work we use BLI to study the proliferation behaviour of PLuc expressing mouse embryonic fibroblasts, seeded on RAD16-I hydrogels and RAD16-I/biorubber composites to assess the biocompatibility of these scaffold materials.

2. Materials and methods

2.1. Scaffolds

Two different materials were used to carry out the experiments: a 16-amino acid peptidic nanofiber scaffold (RAD16-I) [13–19] (Puramatrix®, BD, Erembodegem, Belgium) and a composite material consisting of RAD16-I with a synthetic biorubber [21], a porous structure of poly (diol citrate). The porous biorubber was produced in four steps: synthesis of a pre-polymer, preparation of a porogen mask, curing the pre-polymer and porogen extraction using an apolar solvent. The pre-polymer was obtained by mixing in a vial 1.3 g of citric acid (Sigma) (6.8 mM) and 1 g of 1,8-octanediol (Sigma) (6.8 mM). The sealed vial was then introduced in a microwave (CEM Discovery, Mathews, NC, USA) and melted at 100 °C for 6 min, with stirring, to create a pre-polymer. The porogen structure responsible of conferring porosity to the final polymer consisted of 200 μm polystyrene beads (Goodfellow, Huntington, UK), previously sintered by heating for 2 min in a microwave oven. Following, 10 ml of pre-polymer was poured onto the previously obtained porogen mask, a 13.5 mm diameter, 50 mm high disk, and the mixture was allowed to cure at 120 °C, under vacuum, for 4 days to cross-link the biorubber. Finally, the polystyrene mask was extracted using toluene (Sigma) and cut to the desired final size. The microstructure of the obtained biorubber was characterized using a Scanning Electron Microscopy (SEM). First, the biorubber was frozen in liquid nitrogen and crushed without deforming the structure. The biorubber was gold coated and imaged using a JEOL scanning electron microscope (JSM-5310).

2.2. Material characterization

Rheometry. RAD16-I hydrogel, prepared as explained in Section 2.5, was analyzed using a standard rotational shear stress vs. shear rate experiment, in an AR 550 Rheometer (TA Instruments, West Sussex, UK). The conditions used were the following: ramp of shear stress from 0 to 10 Pa in 10 min and constant temperature at 35 °C.

Mechanical properties. To analyze the biorubber and the RAD16-I/biorubber composite (prepared as explained in Section 2.5), the materials were characterized using a Dynamical Mechanical analyzer DMA Q800 (TA Instruments). A compression clamp and a constant temperature of 35 °C were used in all experiments. Two different sets of experiments were carried out using the instrument methods of: I) strain rate method; a strain ramp from 0 to −35% (compressive behaviour) was applied, and the compressive stress was recorded. II) creep method: a constant compressive force of 0.05 N was applied to the samples during 15 min and the deformation vs. time was recorded.

2.3. Lentivirus production and cell labeling

The lentiviral vector containing the enhanced green fluorescent protein (EGFP) gene under the control of the simian virus SV40 promoter and the *P. pyrallis* luciferase (Luc) gene (Promega Corporation, Madison, WI) under the control of the cytomegalovirus promoter, was constructed by cloning the cassette between the ClaI and BamHI sites of the lentiviral vector Plox/Twgfg provided by Dr. D. Trono (Ecole Polytechnique Fédérale de Lausanne, Lausanne, Switzerland).

Human embryonic kidney cells 293T, obtained from the ATCC (Rockville, Maryland, USA), were used for viral production as previously described [26]. Viral particles were resuspended with PBS 1× and kept at −80 °C. Viral titration was performed using the HIV-1 p24 antigen EiA (Beckman Coulter) 96 test kit.

Mouse embryonic fibroblasts (C57BL/6 cell line, ATCC) were cultured in Dulbecco's Modified Eagle Media-high glucose (DMEM-Hg) (Sigma, Steinheim, Germany) supplemented with 10% heat-inactivated foetal bovine serum (FBS) (Sigma), 50 units/ml penicillin/streptomycin (Sigma) and 4 mM L-glutamine (Sigma). At passage 2 cells were plated at 6500 cells/cm^2 in 12-well plates. The following day an aliquot of viral particles (MOI = 21 infectious viral particles/cell) was diluted in 1 ml of growth medium containing 10 μg/ml polybrene (Sigma) and added to the cells. After 48 h in culture, virus-containing medium was replaced by fresh medium and cells were allowed to grow. The highest 30% eGFP expressing cells (G·Luc-C57BL/6) was selected by FACS, expanded and used for seeding the scaffolds.

2.4. Luciferase assays and DNA quantification

An aliquot of G·Luc-C57BL/6 cells was maintained in culture to monitor luciferase expression during the course of the experiment. Every 15 days cells were trypsinized, counted and an aliquot containing 2×10^5 cells was suspended in reporter lysis buffer (RLB) 1× (Promega) and frozen at −80 °C (cell lysate). At the end of the experiment the collected samples were used to determine luciferase activity and DNA concentration as detailed previously [26].

2.5. Cell seeding

G·Luc-C57BL/6 cells were trypsinized, suspended in a solution of sucrose 10% in deionized water (pH 6.1) (Sigma) and mixed with RAD16-I peptide (BD) to attain a final concentration of 2×10^6 cells/ml in 0.25% RAD16-I peptide solution. Plastic inserts (Millipore, Billerica, MA, USA) were placed in 12-well tissue culture plates leaving a space between the well and the insert. Biorubber pieces were placed in the plastic inserts to create the RAD16-I/biorubber composite. Then, the cell suspension in RAD16-I peptide was pipetted into the insert (with or without biorubber) and 250 μl of growth media were added to the space between each insert and well. The material was allowed to gel at 37 °C for 5 min and 400 μl of growth media were layered onto the hydrogel. The construct pH was equilibrated by changing 2/3 of the media after 30, 60 and 120 min post gelling. RAD16-I hydrogels and RAD16-I/biorubber scaffolds were also prepared without cells to analyze the materials biocompatibility. However, as RAD16-I is transparent, to facilitate histological detection of *in vivo* implants, a mixture of RAD16-I and biotinylated RAD16-I (RAD16-Ib) (3:7), respectively, was used.

In vitro cultivation of RAD16-I and RAD16-I/biorubber seeded scaffolds was performed at 37 °C with 5% CO_2 and medium was changed every 2 days. Scaffolds were cultured *in vitro* during 15 days before being implanted. At this cultivation stage the stiffness of these constructs could match the tissue implanted and allow cells to proliferate due to the new vascular-rich environment, the muscle.

2.6. Mice

Six-week-old BALB/cAnNCrI mice were used to test scaffold biocompatibility and six-week-old BALB/c homozygous nude (nu/nu) mice were used to monitor the *in vivo* behaviour of G·Luc-C57BL/6 cells injected with or without scaffolds. All animals were purchased from Charles-River (Wilmington, MA); BALB/c nu/nu mice were maintained in a specific pathogen-free environment. Animal procedures were performed with the approval of the animal care committee of the Cardiovascular Research Centre and the Government of Catalonia.

2.7. Scaffold implantation

Animals were anesthetized by intraperitoneal injection of 100 mg/kg ketamine (Merial, Duluth, GA) and 3.3 mg/kg xilacine (Henry Schein, Melville, NY), and additionally received a subcutaneous analgesic injection of 0.05 mg/kg buprenorphine (Schering-Plough, Kenilworth, NJ). The inoculation place was shaved (BALB/c mice) and cleaned with povidone-iodine (Braun, Melsungen, Germany). Four implantations were performed in each animal: two subcutaneous (SC) on the back and one intramuscular (IM) in each thigh. Animals received RAD16-Ib hydrogel (BALB/c) or RAD16-I hydrogel + G·Luc-C57BL/6 (BALB/c nu/nu) on the right side and RAD16-Ib/biorubber composite (BALB/c) or RAD16-I/biorubber + G·Luc-C57BL/6 composite (BALB/c nu/nu) on the left side.

For each implantation, an incision was performed on the skin and a small pocket was formed subcutaneously (SC implants) or in the thigh muscle (IM implants). Then, 30 μl of the gelled material were implanted using a syringe fitted with a bevel

ended pipette tip. The incision was closed using absorbable sutures. The control group for the in vivo evaluation of G.Luc-C57GL/6 cells comprised three mice (BALB/c nu/nu) each one receiving four injections (two SC and two IM, in each thigh) of 1.5×10^5 G·Luc-C57BL/6 cells suspended in medium without FBS.

2.8. Bioluminescence imaging

In vivo optical imaging of implanted nude mice was performed as described previously [26]. Mice were anesthetized with ketamine/xilacine and immobilized. Following the inoculation of 50 μl of D-luciferin (100 mg/kg, Promega) in situ (SC or IM) the mice were placed in the detection chamber of a high-efficiency ORCA-2BT Imaging system (Hamamatsu Photonics, Hamamatsu City, Japan) provided with a C4742-98-LWG-MOD camera and a 512×512 pixel, charge couple device (CCD) cooled at $-80\,^{\circ}$C at a distance of 247 mm from the camera objective (HFP-Schneider Xenon 0.95/25 mm). Two images were acquired of each mouse, one using a white light source inside the chamber to register the animal position and a second one, in total darkness, during a 5 min period to acquire photons (PHCs) from the light emitting cells. Images were taken at 0, 7, 15, 30, 45 and 90 days post-implantation. Quantification and analysis of recorded PHCs were done using the Wasabi image analysis software (Hamamatsu Photonics).

To establish the cell detection sensitivity in vivo, a standard curve was generated by imaging predetermined numbers of cells (10^3, 5×10^3, 10^4, 5×10^4, 10^5, 2.5×10^5) grafted IM in BALB/c nu/nu mice.

2.9. Cell migration

To determine if cells from the implants had migrated to other organs, at the end of the 3-month in vivo implantation period, one control (no scaffold) and two scaffold implanted mice (the ones producing most light at the implantation site) were sacrificed, dissected and target organs (brain, liver, spleen, lungs, ribs and lymph nodes) harvested. Luciferase activity, indicative of the presence of cells from the implants, was determined on tissue homogenates using a sensitive lumino-metric procedure as described [28].

2.10. Histology

In vitro cultured gels were washed, fixed with 4% paraformaldehyde (PFA) for 2 h and embedded in paraffin. 5 μm thick sections of the embedded scaffolds were stained with hematoxylin-eosin. To detect RAD16-Ib, sections were deparaffinized, rehydrated and washed in PBS 1×. Then the sections were incubated with the ABC reagent (Dako, Glostrop, Denmark) for 30 min in darkness and processed for dia-minobenzidine (DAB) staining (Roche, Basel, Switzerland) following the manufac-turer instructions. Sections were also counterstained with hematoxylin-eosin (Sigma) as previously described [29].

After the 90 days in vivo period, animals were sacrificed by cervical dislocation and IM and SC implanted samples were harvested when present. Samples were washed with PBS 1× and fixed with 4% PFA (Sigma) for 24 h at 4 °C. IM samples were then placed over an ion-exchange resin (Amberlite IR-120(plus) ion-exchange resin, sodium form, Sigma) and decalcified with formic acid 10% for 24 h at room temperature. Then all samples were embedded in paraffin and serially sectioned (10–14 μm thick).

BALB/c sections were stained with hematoxylin–eosin or with the ABC staining. BALB/c nu/nu sections were stained with hematoxylin–eosin or with the Mas-son-trichrome method [30], which reduces fluorescent background of the muscular tissue, improving the detection of the implanted G·Luc-C57BL/6 cells.

2.11. Statistical analysis

Statistical analysis was performed using the StatView version 5.0. A two-way ANOVA test was performed to compare proliferation of injected G·Luc-C57BL/6 cells, G·Luc-C57BL/6 cells seeded in RAD16-I hydrogel and G·Luc-C57BL/6 cells seeded in RAD16-I/biorubber composite. Statistical significance was considered when $p < 0.05$.

3. Results

3.1. Mechanical and structural characteristics of the scaffold materials

Shear stress analysis of RAD16-I hydrogels (Fig. 1A) showed that the material retains its structure up to a shear stress value of 9 Pa after which shear rate increases dramatically, a typical behaviour of non-cross-linked hydrogels. In order to protect the structural integrity of the RAD16-I hydrogel against mechanical deformation, we generated a porous RAD16-I/biorubber composite that would combine the cell growth characteristics of RAD16-I and the mechanical resilience of elastomers. Analysis of the degree of deformation under stress–strain conditions (Fig. 1B) showed that

both, biorubber and RAD16-I/biorubber behave as typical elasto-mers, with the presence of RAD16-I resulting in a small reduction of elastic modulus and compression strength, likely due to the plas-tificant effect of RAD16-I. The compressive strength of the composite is considerably higher (25,000 Pa) than that of RAD16-I alone (9 Pa). Further creep analysis showed compression defor-mation behaviour also characteristic of elastomeric materials (Fig. 1C), having the RAD16-I/biorubber a slightly reduced resis-tance to deformation.

Structural characterization of the biorubber material by SEM showed (Fig. 3E,F) a reasonably uniform 100–150 μm pore size distribution within the range size of cells, but weak pore connectivity.

3.2. Light production capacity and stability of G·Luc-C57BL/6 cells in vitro

The amount of light generated by the G·Luc-C57BL/6 cells in vitro was determined by measuring the luciferase activity in lysates from predetermined numbers of cells. A standard plot of light production, expressed as relative light units (RLUs) vs. the number of cells in the lysates was generated (Supplementary Fig. 1A) The number of RLUs produced by a single cell is the slope of the linear regression plot, 7.6 RLUs/cell ($R^2 = 0.983$). Luciferase activity was also measured in cell lysates from in vitro cultures collected every 15 days until the end of the experiment (3 months) to determine the stability of luciferase expression. It was shown that light production capacity, expressed as the RLUs/ng DNA vs. cultivation time, was stable during the 3 months tested (Supplementary Fig. 1B).

3.3. Detection sensitivity for G·Luc-C57BL/6 cells in vivo

To correlate the number of cells with the number of PHCs detected in vivo, predetermined numbers of G·Luc-C57BL/6 cells were inoculated IM in the thighs of nude mice and imaged as previously described. Recorded PHCs were extracted from the images using the Wasabi Software and plotted vs. the number of inoculated cells. The images show that a minimum of 10^3 G·Luc-C57BL/6 cells could be detected using the high-efficiency ORCA-2BT Imaging System. Moreover, there was a highly linear relationship between cell number and PHCs ($R^2 = 0.9873$) with a slope of 24.8 PHCs/cell (Fig. 2). Thus it is possible to correlate PLuc activity with the number of G·Luc-C57BL/6 cells in the implants.

3.4. In vitro growth of G·Luc-C57BL/6 cells seeded in a RAD16-I hydrogel and RAD16-I/biorubber composite

Cell seeded RAD16-I and RAD16-I/biorubber composites main-tained their structure during the three months in vitro. The distri-bution of cells within the two scaffold materials was evidenced by hematoxylin–eosin staining of histology sections (10 μm thick). Fig. 3A–D shows that, while G·Luc-C57BL/6 cells seeded in the RAD16-I hydrogel retained a round morphology and grew forming clusters within the biomaterial (Fig. 3C), the same cells seeded in the RAD16-I/biorubber composite neither penetrated into the bio-rubber nor attached to the material surface, but colonized only the RAD16-I hydrogel structure (Fig. 3A,B). Thus, the biorubber appeared to play an exclusively structural role. G·Luc-C57BL/6 cells were also able to grow in the RAD16-Ib (Fig. 3D). Scanning Electron Microcopy (Fig. 3E,F) of the biorubber material shows a micropo-rous structure with pore size ranging from 100 to 150 μm.
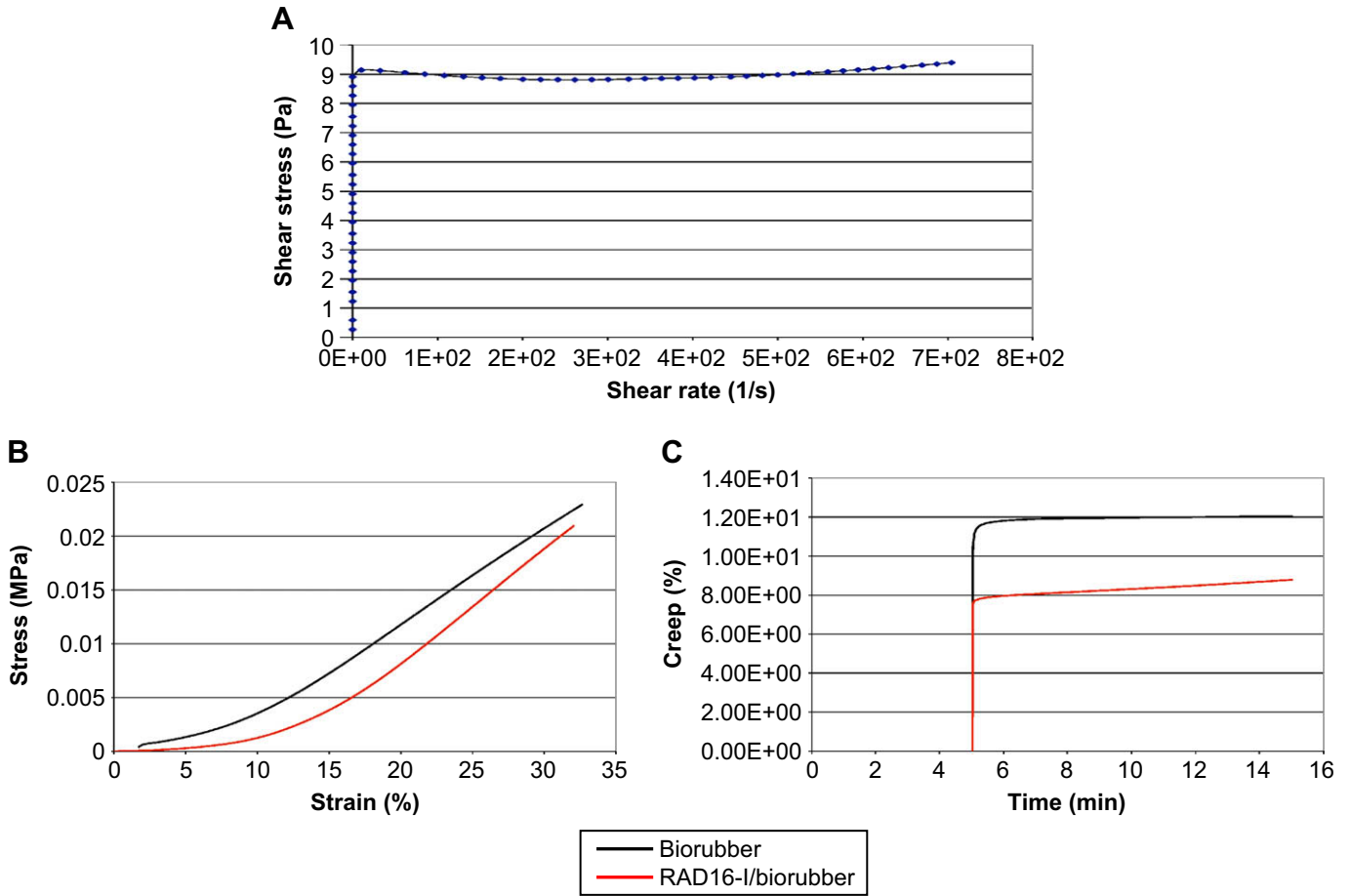
Fig. 1. Mechanical properties of RAD16-I and RAD16-I/biorubber. (A) Rheometric curve, shear stress vs. shear rate, of RAD16-I hydrogel. (B) Compression stress vs. compression strain (absolute value) for biorubber and RAD16-I/biorubber composite. (C) Creep behaviour at compression for biorubber and RAD16-I/biorubber composite.
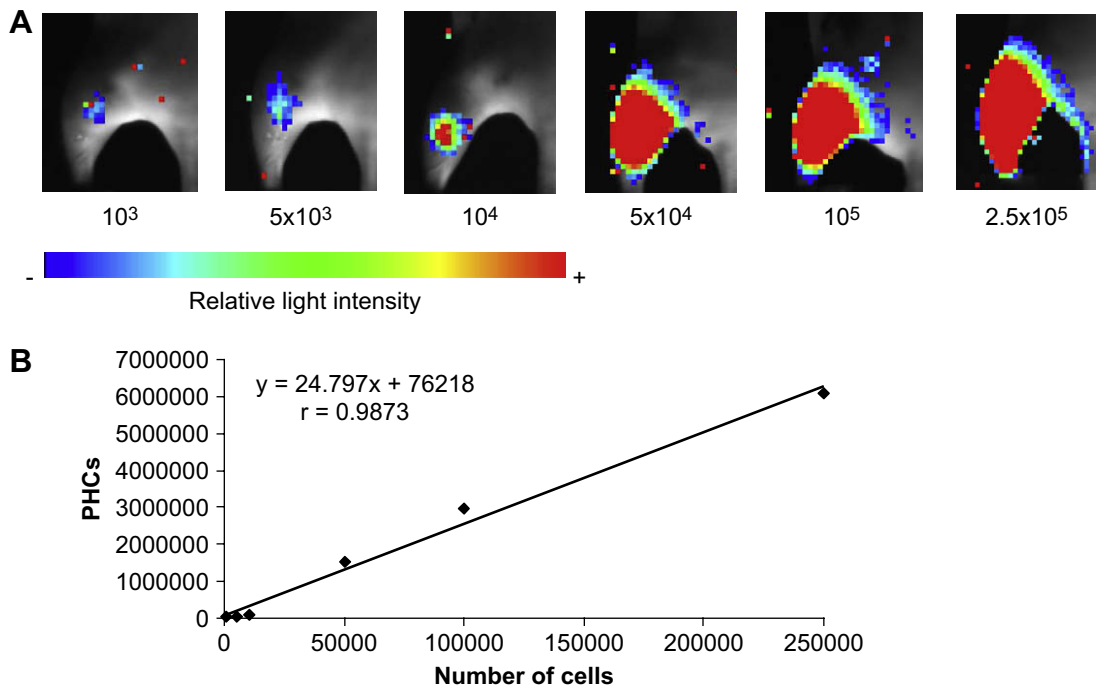

Fig. 2. *In vivo* detection of G·Luc-C57BL/6 cells. (A) BLI images of predetermined numbers of G·Luc-C57BL/6 cells (1×10^3, 5×10^3, 1×10^4, 5×10^4, 1×10^5, 2.5×10^5) inoculated intramuscularly in the thighs of nude mice. Pseudo-colour images represent light intensity levels superimposed on white light images of the mice. Arbitrary colour bar: lowest intensity = blue, highest intensity = red. (B) Standard plot of photon counts (PHCs) recorded in the images plotted, after background subtraction, vs. the number of inoculated cells. The slope of the regression plot is the number of PHCs/cell, r = correlation coefficient.
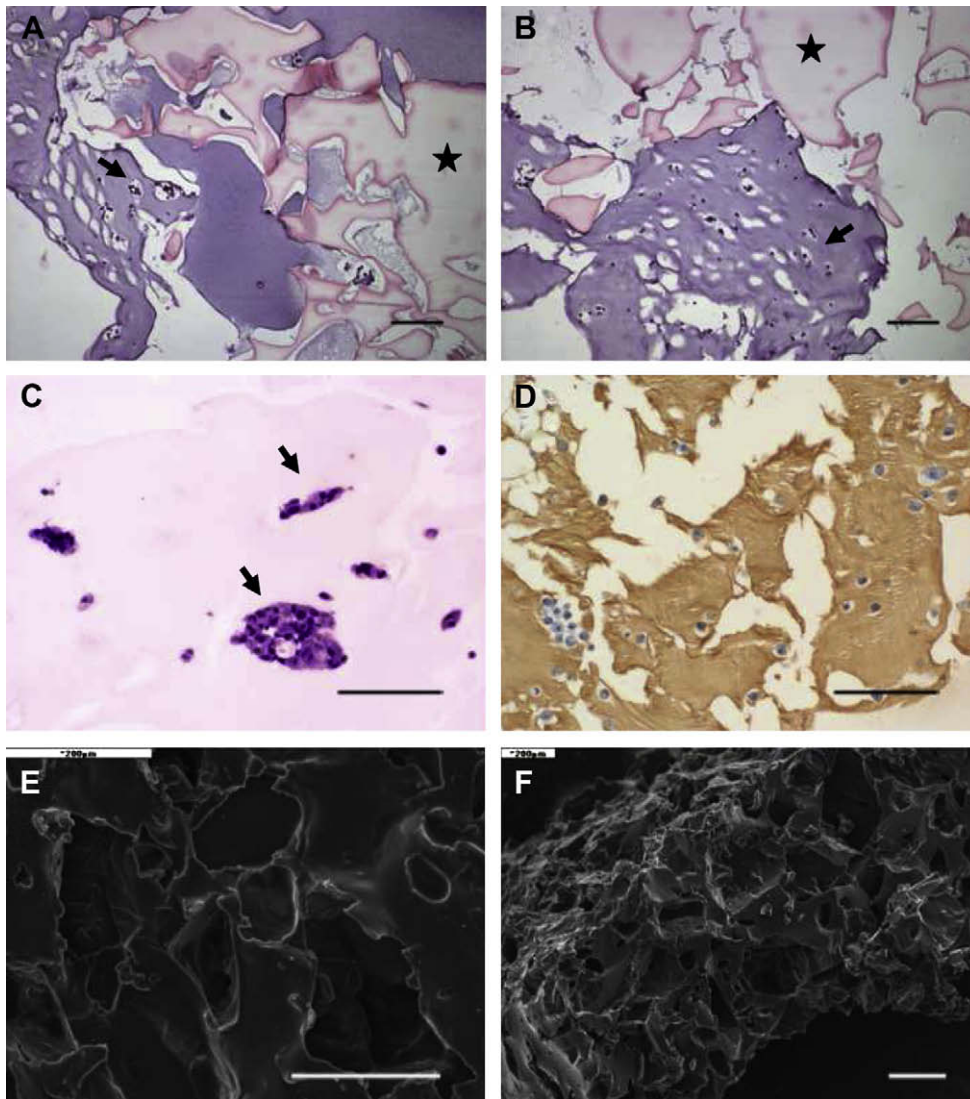
Fig. 3. *In vitro* culture of cells in RAD16-I hydrogel and RAD16-I/*biorubber* composite. (A,B) G·Luc-C57BL/6 cells suspended in RAD16-I peptide were added to *biorubber* and then mixed with growth medium to induce gelling of RAD16-I. Once cured, samples were fixed, dehydrated and embedded in paraffin for sectioning. Hematoxylin–eosin stained sections show cells in the RAD16-I nanofiber hydrogel (arrows) but not in the biorubber (star). (C) Cell clusters (arrows) in sections from RAD16-I hydrogels seeded with G·Luc-C57BL/6 cells stained with hematoxylin–eosin. (D) Sections from RAD 16-Ib hydrogel seeded with G·Luc-C57BL/6 cells and cultivated *in vitro*. Biotinilated RAD 16-Ib was detected with the ABC staining, and cells by counterstaining with hematoxylin–eosin. (E,F) Scanning electron microscope images of freeze-fractured biorubber sputter-coated with gold. Bars: A–D = 100 μm; E, F = 200 μm.

3.5. Bioluminescence imaging

G·Luc-C57BL/6 cells were either, directly SC and IM implanted in BALB/c nu/nu mice, or seeded in RAD16-I hydrogel and RAD16-I/biorubber composites and then SC and IM implanted in BALB/c nu/nu mice. BLI monitoring at days 0, 7, 15, 30, 45 and 90 post-implantation was used to analyze cell proliferative behaviour. The captured images (Figs. 4 and 5) show the presence of G·Luc-C57BL/6 cells at day 0 (implantation) in implants without scaffolds and with RAD16-I hydrogel scaffold, in all the animals. However, in agreement with the previous *in vitro* results, only 2 of 5 SC and in 4 of 5 IM RAD16-I/biorubber implants had G·Luc-C57BL/6 cells (Fig. 5A), suggesting that cells had difficulties penetrating and colonizing the biorubber material during the seeding period.

All SC implants of G·Luc-C57BL/6 cells, regardless of whether they had been implanted with or without scaffold, tended to disappear with time, as previously reported for other cell types [25], and only one of the SC RAD16-I implants retained some cells by the end of the experiment.

G·Luc-C57BL/6 cells implanted IM without scaffold suffered a growth crisis 7 days post-implantation, following which the number of cells recovered to approximately that originally implanted, to then begin declining again by day 45 (Figs. 4 and 6B,D).

G·Luc-C57BL/6 cells seeded in RAD16-I/biorubber composites disappeared rapidly from 4 of the 5 animals with IM implants but grew well in the remaining one (Fig. 5A).

Conversely, G·Luc-C57BL/6 cells seeded in RAD16-I hydrogel, IM implanted, tended to grow from the beginning of the experiment in 4 of the 5 implantation sites. The difference in growth capacity between G·Luc-C57BL/6 cells seeded in the RAD16-I hydrogels and those implanted alone or in the RAD16-I/biorubber composites was statistically significant ($p < 0,05$) (Fig. 6D).

3.6. Biocompatibility of the cell constructs implanted

To determine the possible generation of immunoresponses to the biomaterials under study, RAD16-Ib hydrogel and the
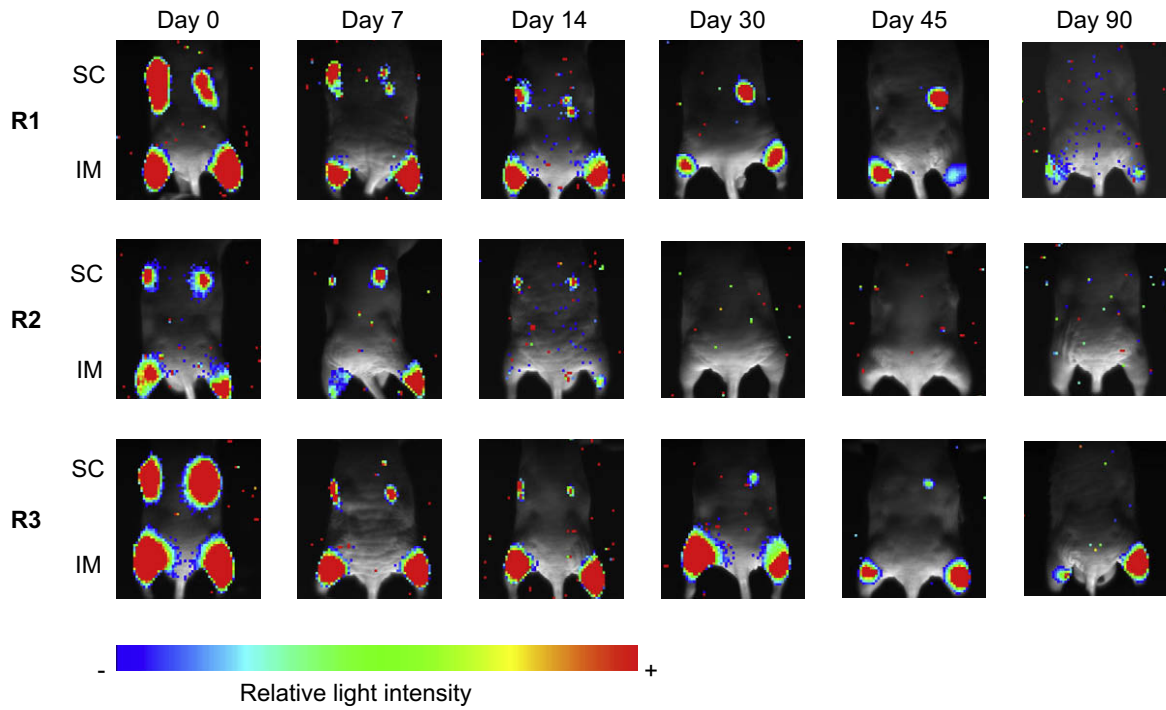
Fig. 4. Proliferation of G·Luc-C57BL/6 cells *in vivo* without scaffolds. BLI composite pseudo-colour images showing light intensity levels from SC and IM implanted G·Luc-C57BL/6 cells without scaffolds, overlaid on the corresponding white light images of mice. Colour bar shows the relative light intensity (lowest intensity = blue, highest intensity = red).
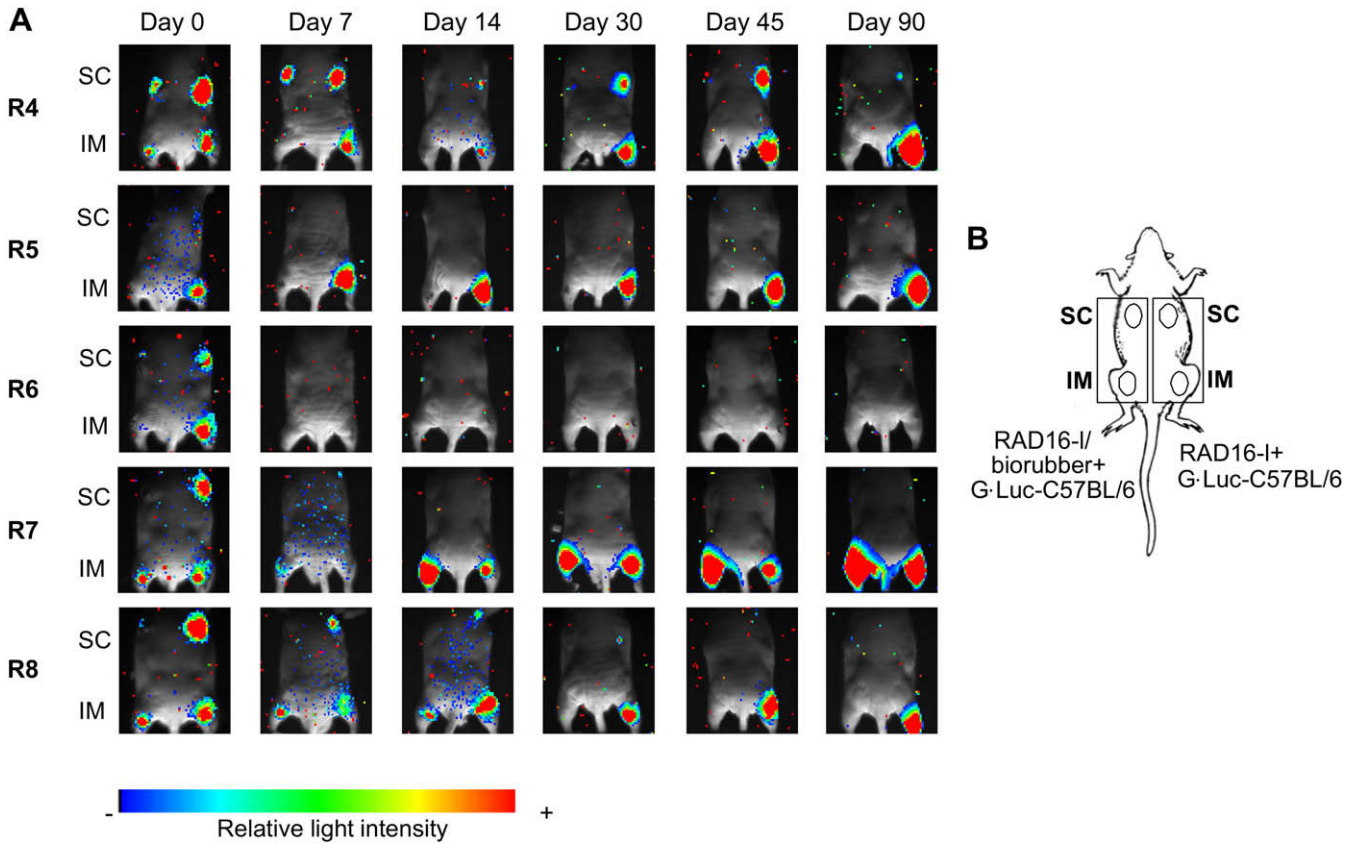

Fig. 5. Proliferation of G·Luc-C57BL/6 cells seeded on RAD16-I hydrogels or RAD I/biorubber scaffolds. (A) BLI composite pseudo-colour images showing light intensity levels of IM and SC implanted G·Luc-C57BL/6 cells seeded in RAD 16-I or RAD 16-I/*biorubber* overlaid on the corresponding white light images of mice. Colour bar shows the relative light intensity (lowest intensity = blue, highest intensity = red). (B) Diagram showing the location of the SC and IM implants of seeded RAD16-I and RAD16-I/biorubber composites.
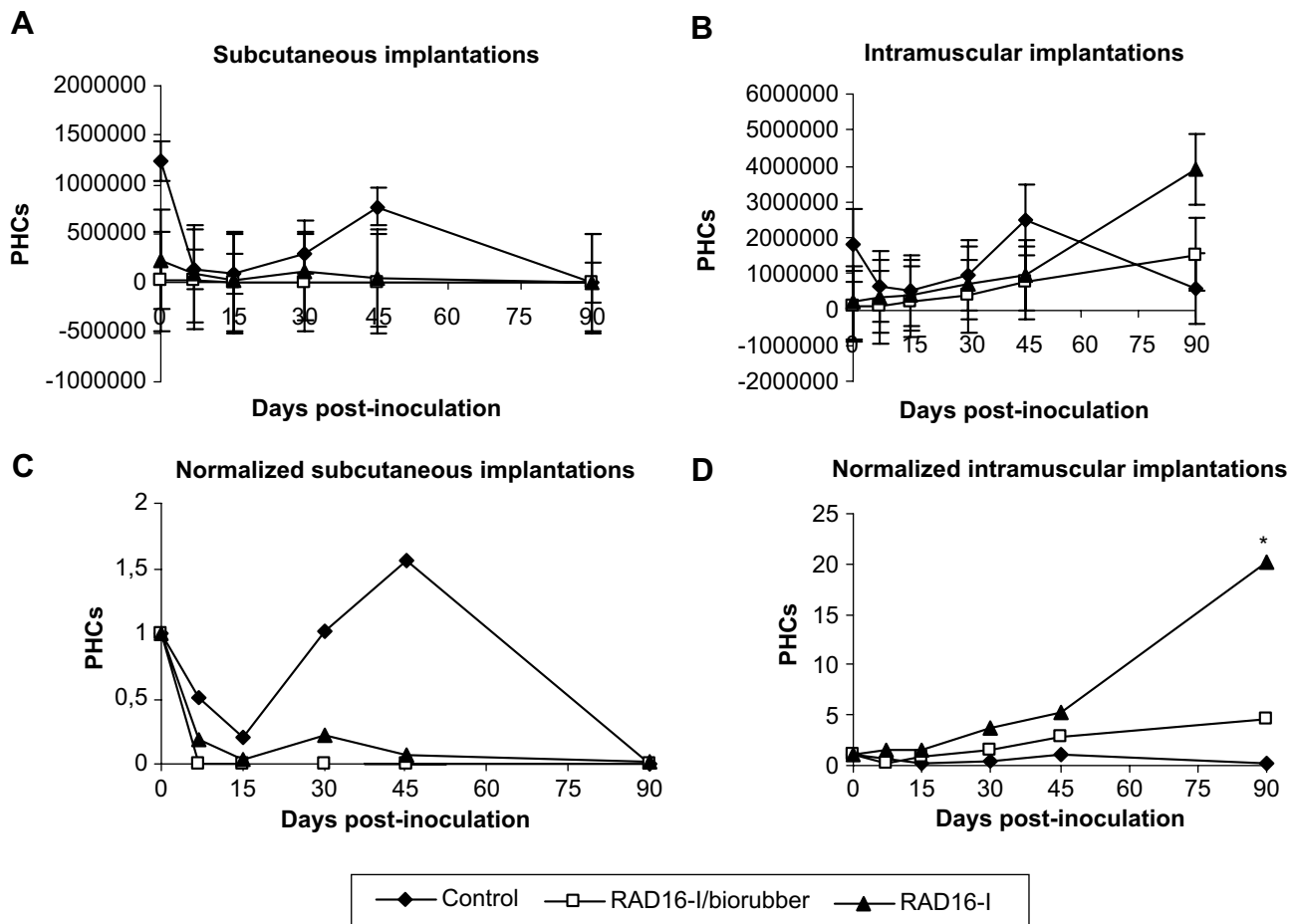
Fig. 6. Quantitative analysis of BLI data. After background subtraction of recorded photon counts (PHCs) from SC (A) and IM (B) implantations of G·Luc-C57BL/6 cells implanted without scaffold (◆) or after seeding in RAD 16-I hydrogels (▲) or RAD 16-I/*biorubber* composites (□), PHCs were plotted *vs.* time post-implantation. To compensate for differences in the seeding of scaffolds, PHCs were normalized with respect to those at day 0 (C and D). Dots represent the average value at each time point. Bars represent standard deviation, * = statistical significance ($p < 0.05$).

RAD16-Ib/biorubber composites were implanted SC and IM in six BALB/c immunocompetent mice. Implants were harvested at days 15, 30 and 45 post-implantation. No macroscopic signs of inflammation or rejection were observed in either of the implantation sites through the test. Furthermore, lymphatic nodes had normal appearance and size in all animals. Paraffin sections from the IM implants were also stained with hematoxylin–eosin (Fig. 7), or probed with the ABC staining to localize biotin labeled RAD16-Ib. However, no signs of RAD16-Ib could be detected in the tissue sections from either early (15 days) or late (45 days) implants, indicating that the peptide scaffold had been degraded and eliminated. In contrast, the biorubber material was clearly detectable in the hematoxylin–eosin stained sections, and showed no signs of degradation while implanted in the muscular tissue (Fig. 7A–F) or in the SC cavity (data not shown). And although a fibrotic tissue layer was observed surrounding the biorubber (Fig. 7A–D) and some host cells appeared to have migrated into the scaffold (Fig. 7E and F), no signs of immune response based on lymphocytic infiltration or giant body cells were detected.

As was the case for normal mice, macroscopic evaluation of the implants from immunodeficient BALB/c nu/nu mice also failed to show signs of rejection or inflammatory reactions (Fig. 8H,I,K,L) and only the biorubber, but no RAD16-I, was detected at the IM and SC implantation sites. In this case, a layer of fibrotic tissue surrounding the implants was also detected.

3.7. Fluorescence analysis of implants from BALB/c nu/nu mice

Selected sections from nude mice IM implants of RAD16-I hydrogels and RAD16-I/biorubber composites seeded with G·Luc-C57BL/6 cells were deparaffined and stained by the Masson-trichrome method, to reduce the muscle autofluorescence, and examined by fluorescence emission microscopy to determine the contribution of G·Luc-C57BL/6 cells. Images (Fig. 8A–F,G,J) showed that implants generating high BLI signals also contained more G·Luc-C57BL/6 cell clusters and total cells than implants producing lower BLI signals. Occasionally, IM implants showing no BLI signal had also some G·Luc-C57BL/6 cells. Thus, there was a strong correlation between the number of cells in the implants and the amount of light produced. However, no quantification was possible due to the difficulty of estimating fluorescent cell numbers in cell clusters.

3.8. Cell migration

Measurement of luciferase activity in brain, liver, spleen, lungs, bone and lymph node, homogenates failed to show the presence of any significant number of luminescent cells, within the detection limit of the procedure (a minimum of 10 cells/lymph node or 50–100 cells for the rest of the tested organs), indicating that cell death rather than migration was responsible for the disappearance light from the implants.
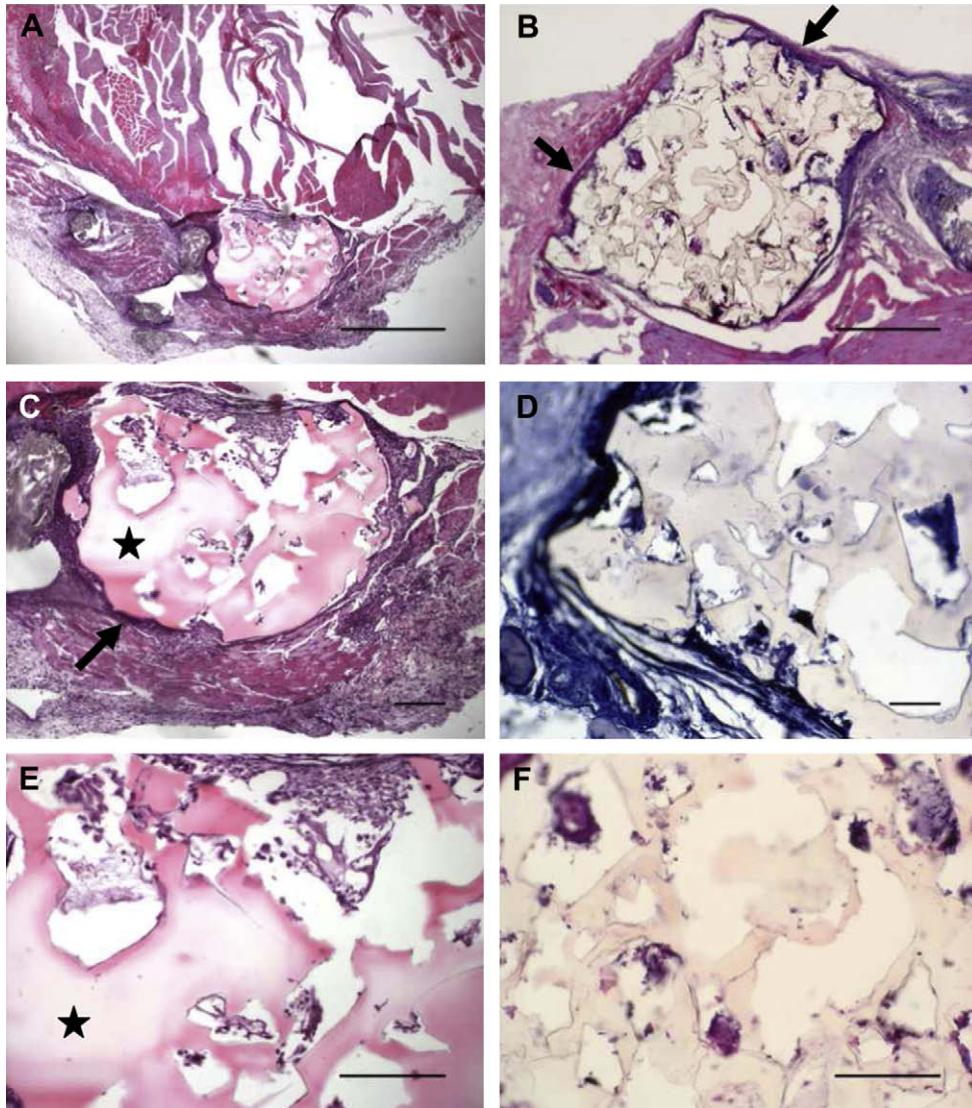
Fig. 7. Histology of balb/c mice implants. Tissue sections (10 μm) from IM implants at 15 days (A,C,E) or 45 days (B,D,F) post-implantation, stained with hematoxylin–eosin (A–C,E,F) or stained for biotin and counterstained with hematoxylin (D). RAD16-Ib was not detected while biorubber (star in C,D) was present in all sections of RAD16-I/biorubber implants. Arrow head (B,C) points to the fibrotic layer surrounding biorubber scaffolds. Bars: A, B = 500 μm; C,D,E,F = 100 μm.

4. Discussion

The aim of the current work was the use of a model system, based on non-invasive bioluminescence imaging (BLI) of luciferase expressing cells seeded in scaffold materials, to analyze the application of RAD16-I [12–18] scaffolds and RAD16-I/biorubber composites for tissue regeneration.

Mouse embryonic fibroblasts C57Bl/6 cells, capable of growing and *in vitro* differentiating to osteogenic cells in RAD16-I hydrogels [13,31], were used in these experiments as a model to analyze the capacity of the materials to sustain cell growth *in vivo*. In spite of their good capacity to sustain cell proliferation, the low shear stress resistance (9 Pa) of RAD16-I hydrogels could result in rapid scaffold degradation, an important restriction for their application in many tissues to overcome this limitation we combined RAD16-I with a biorubber elastomer having better shear-strain characteristics (25,000 Pa) within the range of animal tissues (Brain: 100–200 Pa, Disc Cartilage (nucleus pulposum): 300–400 Pa, Skeletal and cardiac muscle: 3000–4000 Pa, Joint cartilage: 1–10 MPa) and a relatively uniform (100–150 μm) pore size distribution.

In vitro, C57BL/6 cells, tagged by infection with lentiviral vectors for the expression of PLuc and EGFP (G·Luc-C57BL/6), produced 7.6 RLUs/cell stably throughout the duration of the experiments (90 days). Cells implanted *in vivo* were easily detectable, and analysis of BLI images, from predetermined numbers of G·Luc-C57BL/6 cells implanted in the thighs of BALB/c nu/nu mice, showed that, it was possible to detect a minimum of 1000 cells and that there was a linear correlation between the amount of light detected and the number of implanted cells, with a slope of 24.8 PHCs/cell.

The capacity of the RAD16-I hydrogels and RAD16-I/biorubber composite scaffolds to support G·Luc-C57BL/6 cell growth was first analyzed *in vitro* and then *in vivo* by BLI imaging of cells seeded in scaffolds and implanted, IM or SC, in BALB/c nu/nu mice. *In vitro*, G·Luc-C57BL/6 cells penetrated the RAD16-I hydrogels and grew on them forming clusters [13]. However, no cells could be observed within the biorubber material, suggesting that, although the biorubber was non-toxic for the cells, some of the scaffold characteristics, such as pore interconnectivity, material surface structure or composition limited cell penetration and colonization [32]. Survival of cells implanted in mice was conditioned by the implantation site. Thus, in SC implants, G·Luc-nC57BL/6 cells were unable to survive
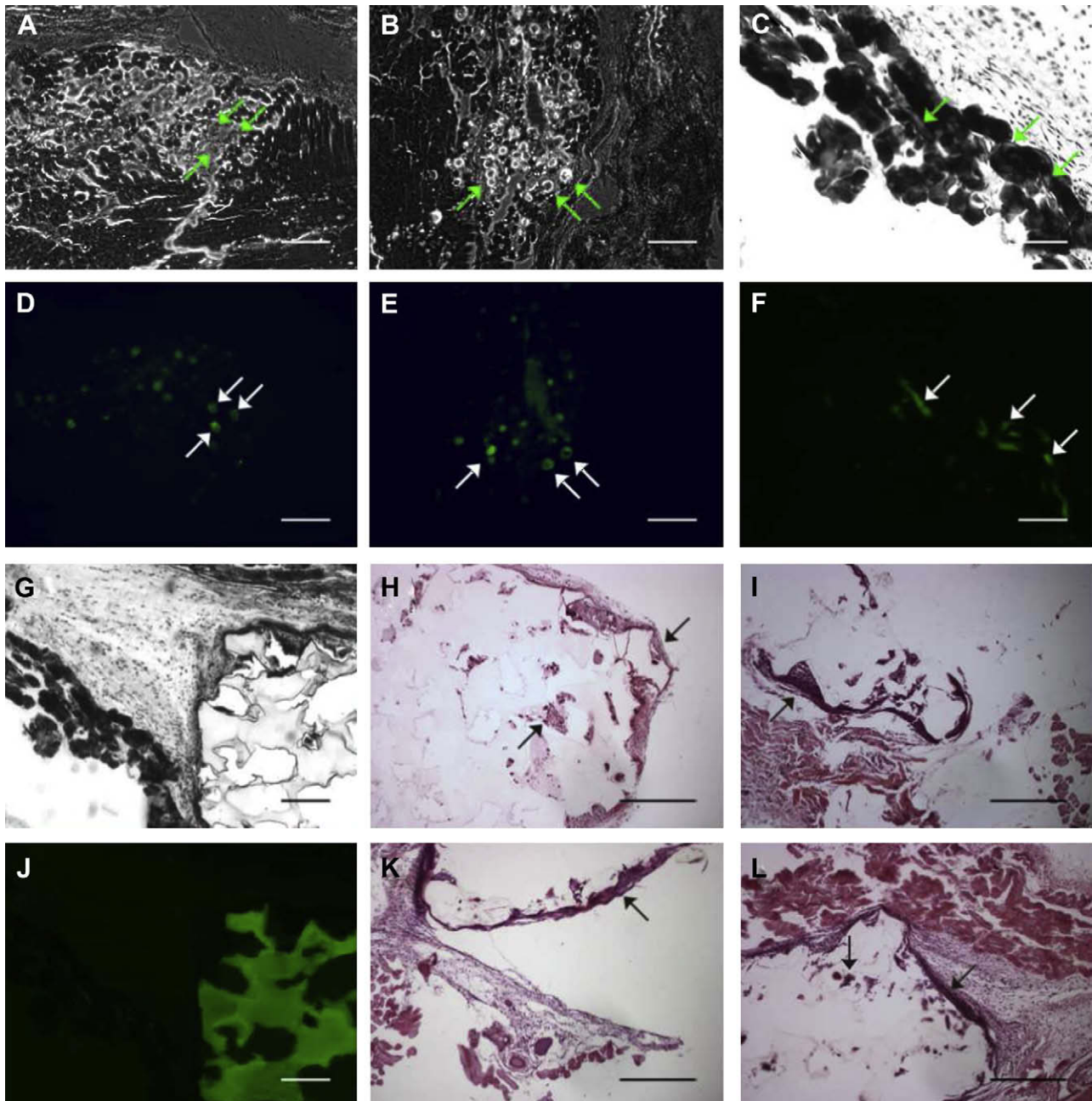
Fig. 8. Histology of BALB/c nu/nu mice implants. 10 μm sections from RAD16-I (A,B,D and E) and RAD16-I/biorubber (C,F,G–L) composites seeded with G·Luc-C57BL/6 cells and implanted IM in nude mice during a 90-day period, showing high BLI signal. White light (A–C,G) and fluorescence microscope images using the GFP channel (D–F,J) of Masson's trichrome stained sections. G·Luc-C57BL/6 cell detection at the IM implantation sites (white and green arrows in A–F) was higher in seeded RAD16-I implantations than in seeded RAD16-I/biorubber implantations. (J) Biorubber showed high autofluorescence when visualized using the GFP microscope channel. (H,I,K,L) Hematoxylin–eosin stained sections showed biorubber maintenance after 90 days, from mice implanted with RAD 16-I/biorubber scaffolds, and presence of fibrous tissue surrounding the implants (arrows). Bars = 200 μm.

until the end of the experiment, regardless of whether they had been seeded or not in scaffolds, as previously reported [27]. Conversely, growth of G·Luc-C57BL/6 cells implanted IM without scaffolds suffered a pronounced crisis within the first week after implantation but then tended to reach a steady state. In general, cells survived better at IM sites whether or not they had been seeded on scaffolds, and 9 of the 16 implants retained cells after 12 weeks. It is possible that the differential survival of cells at IM and SC sites could be related to their capacity to promote an adequate blood supply [33].

The materials tested had clearly different capacities to sustain cell growth. All the RAD16-I hydrogels were successfully colonized by the G·Luc-C57BL/6 cells *in vitro*, and when the cell seeded

materials were implanted IM, in all but one case, cells survived and proliferated until the end of the experiment. However, the biorubber material could not be colonized by cells *in vitro* and *in vivo* did not promote proliferation of seeded cells when combined with RAD16-I. This was possibly the result of biorubber having too small-interconnected pores to allow tissue ingrowth, vascularization and nutrient delivery [32]. Our results show that the use of the RAD16-I as a scaffold to implant cells in live animals has a boosting effect on their proliferation and survival, as compared to cells implanted without the scaffold.

Histological analysis of mouse implants from both types of materials showed that while biorubber persisted undegraded for long times, RAD16-I was biodegradable and could not be detected by

the end of the experiment *in vivo*, likely do to hydrolysis of the peptide linkers. None of the materials appeared to elicit an immune response in normal animals as judged by the absence of infiltrating lymphocytes or inflammation. However, implanted RAD16-I/biorubber composites were found surrounded by a layer of fibrotic tissue from the host as previously reported for other materials [34,35]. Together with the small-interconnected pores and the high stiffness (25 kPa), the observed tendency to become encapsulated could explain the failure of the material to sustain cell colonization and survival *in vivo*.

5. Conclusions

Our results illustrate the application of cell seeded RAD16-I hydrogels in tissue engineering due to their capacity to sustain cell growth *in vivo* and the lack of inflammation/immunologic responses. It is possible that the combination of RAD16-I hydrogels with other biomaterials showing higher mechanical properties could be useful in the reparation of many tissues. We thought that variations in pore size, surface and degradation characteristics of biorubber would improve RAD16-I/biorubber composites for tissue regeneration uses. Moreover, the combination of these seeded materials with other cell types such as endothelial and/or perivascular cells, which have shown to promote a vascular network formation when seeded in scaffolds and implanted *in vivo* [36], will also enhance RAD16-I and RAD16-I/biorubber applications.

Acknowledgements

## Appendix. Supplementary information

Supplementary information associated with this article can be found in the online version, at doi:10.1016/j.biomaterials.2008.11.021.

References

[1] Mikos AG, Herring SW, Ochareon P, Elisseeff J, Lu HH, Kandel R, et al. Engineering complex tissues. Tissue Eng 2006;12:3307–39.
[2] Ratner BD, Hoffman AS, Schoen FJ, Lemons JE. Biomaterials science. Part I: classes of materials used in medicine. Elsevier Academic Press; 2004.
[3] Cai Y, Liu Y, Yan W, Hu Q, Tao J, Zhang M, et al. Role of hydroxyapatite nanoparticle size in bone cell proliferation. J Mater Chem 2007;17:3780–7.
[4] LeGeros RZ. Biodegradation and bioresorption of calcium phosphate ceramics. Clin Mater 1993;14:65–88.
[5] van Blitterswijk CA, Hesseling SC, Grote JJ, Koerten HK, de Groot K. The biocompatibility of hydroxyapatite ceramic: a study of retrieved human middle ear implants. J Biomed Mater Res 1990;24:433–53.
[6] Oh S, Tobin E, Yang Y, Carnes Jr DL, Ong JL. In vivo evaluation of hydroxyapatite coatings of different crystallinities. Int J Oral Maxillofac Implants 2005;20:726–31.
[7] Xue W, Tao S, Liu X, Zheng, Ding C. In vivo evaluation of plasma sprayed hydroxyapatite coatings having different crystallinity. Biomaterials 2004;25:415–21.
[8] Burgeson RE, Nimni ME. Collagen types. Molecular structure and tissue distribution. Clin Orthop Relat Res 1992;282:250–72.
[9] Peggion E, Cosani A, Terbojevich M, Borin G. Conformational studies on polypeptides. The effect of sodium perchlorate on the conformation of poly-L-lysine and of random copolymers of L-lysine and L-phenylalanine in aqueous solution. Biopolymers 1972;11:633–43.
[10] Rippon WB, Chen HH, Walton AG. Spectroscopic characterization of poly(Glu-Ala). J Mol Biol 1973;75:369–75.
[11] Seipke G, Arfmann HA, Wagner KG. Synthesis and properties of alternating poly(Lys-Phe) and comparison with the random copolymer poly(Lys 51, Phe 49). Biopolymers 1974;13:1621–33.
[12] Zhang S, Holmes TC, DiPersio CM, Hynes RO, Su X, Rich A. Self-complementary oligopeptide matrices support mammalian cell attachment. Biomaterials 1995;16:1385–93.
[13] Garreta E, Genove E, Borros S, Semino CE. Osteogenic differentiation of mouse embryonic stem cells and mouse embryonic fibroblasts in a three-dimensional self-assembling peptide scaffold. Tissue Eng 2006;12:2215–27.
[14] Genove E, Shen C, Zhang S, Semino CE. The effect of functionalized self-assembling peptide scaffolds on human aortic endothelial cell function. Biomaterials 2005;26:3341–51.
[15] Kisiday J, Jin M, Kurz B, Hung H, Semino C, Zhang S, et al. Self-assembling peptide hydrogel fosters chondrocyte extracellular matrix production and cell division: implications for cartilage tissue repair. Proc Natl Acad Sci U S A 2002;99:9996–10001.
[16] Narmoneva DA, Oni O, Sieminski AL, Zhang S, Gertler JP, Kamm RD, et al. Self-assembling short oligopeptides and the promotion of angiogenesis. Biomaterials 2005;26:4837–46.
[17] Semino CE, Kasahara J, Hayashi Y, Zhang S. Entrapment of migrating hippocampal neural cells in three-dimensional peptide nanofiber scaffold. Tissue Eng 2004;10:643–55.
[18] Semino CE, Merok JR, Crane GG, Panagiotakos G, Zhang S. Functional differentiation of hepatocyte-like spheroid structures from putative liver progenitor cells in three-dimensional peptide scaffolds. Differentiation 2003;71:262–70.
[19] Holmes TC, de Lacalle S, Su X, Liu G, Rich A, Zhang S. Extensive neurite outgrowth and active synapse formation on self-assembling peptide scaffolds. Proc Natl Acad Sci U S A 2000;97:6728–33.
[20] Misawa H, Kobayashi N, Soto-Gutierrez A, Chen Y, Yoshida A, Rivas-Carrillo JD, et al. PuraMatrix facilitates bone regeneration in bone defects of calvaria in mice. Cell Transpl 2006;15:903–10.
[21] Sodian R, Sperling JS, Martin DP, Egozy A, Stock U, Mayer JEJ, et al. Fabrication of a trileaflet heart valve scaffold from a polyhydroxyalkanoate biopolyester for use in tissue engineering. Tissue Eng 2000;6:183–8.
[22] Webb AR, Yang J, Ameer GA. Biodegradable polyester elastomers in tissue engineering. Expert Opin Biol Ther 2004;4:801–12.
[23] Saditok RT, Blackwell TS. Bioluminescence imaging. Proc Am Thorac Soc 2005;2:537–40.
[24] Derose CM, De A, Loening AM, Ray P, Chatziioannou AF, Gambhir SS. Multi-modality imaging of tumour xenografts and metastases in mice with combined small-animal PET, small-animal CT, and bioluminescence imaging. J Nucl Med 2007;48:295–303.
[25] Román I, Vilalta M, Rodriguez J, Matthies AM, Srouji S, Livne E, et al. Analysis of progenitor cell-scaffold combinations by in vivo non-invasive photonic imaging. Biomaterials 2007;28:2718–28.
[26] Dégano IR, Vilalta M, Bagó JR, Matthies AM, Hubbell JA, Dimitriou H, et al. Bioluminescence imaging of calvarial bone repair using bone marrow and adipose tissue-derived mesenchymal stem cells. Biomaterials 2008;29:427–37.
[27] Lee H, Teng S, Chen H, Lo W, Sun Y, Lin T. Imaging human bone marrow stem cell morphogenesis in polyglycolic acid scaffolds by multiphoton microscopy. Tissue Eng 2006;12:2835–41.
[28] Rubio N, Villacampa MM, El Hilali N, Blanco J. Metastatic burden in nude mice organs measured using prostate tumor PC-3 cells expressing the luciferase gene as quantifiable tumor cell marker. Prostate 2000;44:133–43.
[29] Kim MS, Kim SK, Kim SH, Hyun H, Khang G, Lee HB. In vivo osteogenic differentiation of rat bone marrow stromal cells in thermosensitive MPEG–PCL diblocks copolymer gels. Tissue Eng 2006;12:2863–73.
[30] Garvey W. Modified elastic tissue-Masson trichrome stain. Stain Technol 1984;59:213–6.
[31] Quintana L, Fernández T, Genové E, Olmos MM, Borrós S, Semino CE. Early tissue patterning is recreated by mouse embryonic fibroblasts in a three-dimensional environment. Tissue Eng, in press, doi:10.1089/ten.tea.2007.0296.
[32] Polak J, Hench L. Gene therapy progress and prospects: in tissue engineering. Gene Ther 2005;12:1725–33.
[33] Rickert D, Moses MA, Lendlein A, Kelch S, Franke RP. The importance of angiogenesis in the interaction between polymeric biomaterials and surrounding tissue. Clin Hemorheol Microcirc 2003;28:175–81.
[34] Yoon SJ, Kim SH, Ha HJ, Ko YK, So JW, Kim MS, et al. Reduction of inflammatory reaction of poly(D,L-lactic-co-glycolic acid) using demineralized bone particles. Tissue Eng Part A 2008 Apr;14:539–47.
[35] Fellah BH, Josselin N, Chappard D, Weiss P, Layrolle P. Inflammatory reaction in rats muscle after implantation of biphasic calcium phosphate micro particles. J Mater Sci Mater Med 2007;18:287–94.
[36] Au P, Tam J, Fukumura D, Jain RK. Small blood vessel engineering. Methods Mol Med 2007;140:183–95.

Summary: The modification of hydroxyapatite powder using cold plasma is described. This modification can be used to improve hydroxyapatite water dispersability and to control calcium release. A downstream and a fluidized bed reactor have been successfully set-up to perform the surface treatment on hydroxyapatite. The advantages and drawbacks of both systems are presented.
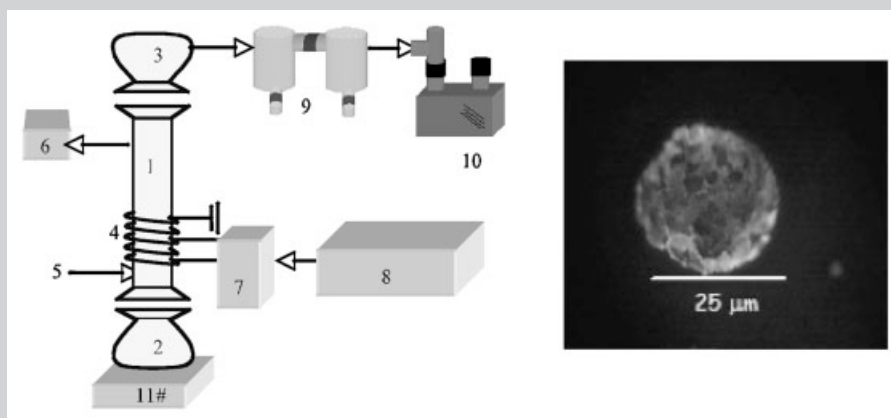
Schematic of the downstream reactor sued here and an optical microscope picture of spherical HA particles.

Plasma Polymerization on Hydroxyapatite Powders to Increase Water Dispersability for Biomedical Applications

Elena Garreta,[1] Núria Tricás,[1] Lluis Quintana,[1] Carlos E. Semino,[1,2] Salvador Borrós*[1]

[1] Grup d'Enginyeria de Materials, Barcelona Bioengineering Center, Institut Químic de Sarriá-Universitat Ramon Llull, Via Augusta 390, Barcelona 08017, Spain
 Fax: +34-93-205-6266; E-mail: s.borros@iqs.url.edu
[2] Center for Biomedical Engineering-Massachusetts Institute of Technology, Cambridge, MA 02139, USA

Introduction

Hydroxyapatite (HA) ceramics have been proven to be bioactive materials because of their ability to chemically bond with bone.[1,2] It is generally accepted that HA enhances bone adaptation and formation in HA-coated implants.[3] In addition, it has been reported that osteoblastic cells differentiate on HA and produce bone-like tissue.[4] However, to improve osteoconduction and osteoinduction, the interaction between cell and substrate plays an important role, since it will influence cell proliferation and differentiation.[5] Some recent reports have studied cell adhesion and proliferation on calcium phosphate materials with different surface characteristics.[6] However, a much more interesting approach for hard tissue regeneration is to try and combine the HA with natural or synthetic organic matrices in order to mimic the three-dimensional in-vivo cell environment. Even more attractive is the possibility to develop smart biocomposites that mediate specific cell responses through biomaterial–cell interactions. Plasma deposition techniques have recently attracted much interest in the field of biomaterials science, since they are able to modify the surface properties of biomaterials to confer reactivity in order to match specific applications.

In order to modify the HA surface, cold plasma techniques have been considered as one of the best options. This technique is well known to modify the surface properties without affecting the bulk of the material. The low temperature range in which this technique works prevents any phase structure modification, which would be critical in this application.[7] In addition, the porosity can be maintained without modification when plasma conditions are optimized.[8] This is a very important point in the present case as porosity in the HA is necessary to promote cell growth in the inner structure.

Although many studies have been performed to modify flat surfaces using cold plasma, systems that treat powders have not been so commonly described. The main utilized reactors are downstream, fluidized bed, and circulating reactors.[9–11] Some bell-jar types including vibrational systems in order to homogenize the treatment have also been described.[12] The most frequently used plasma gases include oxygen, nitrogen, ammonia, acrylic acid, and fluorinated monomers.[13–15] In our group deposition on the surface of carbon black using acrylic acid as well as methyl methacrylate has been performed to show a change in the absorptive properties of this material.[16]
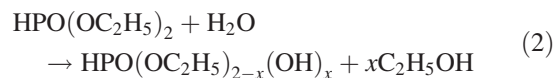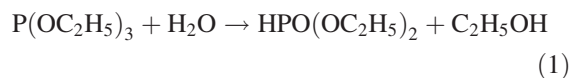
So far, plasma treatment on powders has been described mainly on polymer beads, carbon black, and some other pigments.[17–19] On the other hand, flat surfaces have been treated in order to promote cell growth and adherence. In this work, the modification of HA powder using cold plasma is described. A downstream and a fluidized bed reactor have been successfully set-up to perform the surface treatment on HA. The advantages and drawbacks of both systems are presented in this paper. The surface modification of HA powder can be tailored to obtain a good dispersability of this material in aqueous media. This property could be used to improve the compatibility of HA powder with organic matrices as well as control the calcium release from HA. This offers good possibilities to develop new biocomposite HA/organic biomimetic matrices with future applications in bone tissue engineering.

Experimental Part

Sol-Gel Synthesis of HA

The basic sol-gel procedure was adapted from elsewhere,[20] but included the use of different phosphorous and calcium precursors and a range of experimental conditions that allowed the fabrication of HA ceramics with tailored crystallinity and composition. Triethyl phosphite (cat. no. 538728, Aldrich) or triethyl phosphate (cat. no. T61204, Aldrich) were used as phosphorous precursors, and calcium nitrate tetrahydrate (cat. no. C1396, Aldrich) or calcium acetate (cat. no. 573973, Aldrich) were used as calcium precursors. Briefly, the phosphorous precursor was diluted in anhydrous ethanol and an amount of distilled water was added for hydrolysis (molar

ratio water/phosphorous precursor between 3 and 5). According to the literature, it is assumed that Reaction (1) and (2) are a representation of the typical chemical path during the hydrolysis of triethyl phosphite:

$$P(OC_2H_5)_3 + H_2O \rightarrow HPO(OC_2H_5)_2 + C_2H_5OH \tag{1}$$

$$\begin{aligned} HPO(OC_2H_5)_2 &+ H_2O \\ &\rightarrow HPO(OC_2H_5)_{2-x}(OH)_x + xC_2H_5OH \end{aligned} \tag{2}$$

The mixture was stirred in a closed vessel for 24 h until complete hydrolysis, when a clear and odorless solution was obtained. Immediately after hydrolysis of the phosphorous precursor, a stoichiometric amount (to maintain the calcium/phosphorous ratio of HA to 1.67) of 3 M calcium precursor dissolved in distilled water was added dropwise into the hydrolyzed phosphorous sol. Vigorous stirring was continued for an additional 25 min after the addition. A clear solution was obtained. The sol was then aged for 20 h at room temperature to allow the formation of Ca–P intermediates. The hydrolyzed phosphite interacts with Ca ions in aqueous solution through a condensation polymerization reaction to form a Ca–P intermediate:

$$\begin{aligned} HPO(OC_2H_5)_{2-x}(OH)_x &+ Ca^{2+} \\ &\rightarrow Ca-P\, intermediate + 2H^+ \end{aligned} \tag{3}$$
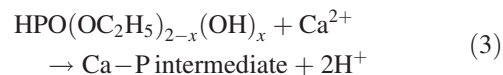
The highly acidic pH of the solution during the aging time is an indication of this reaction. Afterwards, approximately 80 vol.-% of the solvent was removed by heating the sol at 70 °C. A solid-like white gel was obtained upon cooling to room temperature. The wet gel was completely dried and submitted to different temperatures ranging from 100 to 1 000 °C in order to form the crystalline phase of HA. The crystallinity and the crystal size of the HA was controlled by changing the thermal treatment of the gel as well as the precursors used in the sol-gel procedure.

The HA powders were analyzed using X-ray diffractometry (XRD) (Bruker D-5005). Scanning parameters included a 2θ scan range of 4° to 60°, a step size of 0.05°, and a step time of 3 s. Identification of crystalline phases was done by comparing with Joint Committee on Powder Diffraction Standards (JCPDS) files.

Fabrication of Spherical HA

The method to produce porous granules was based on a liquid immiscibility effect.[3] A suspension of HA powder in a 10% aqueous solution of gelatin (cat. no. 48723, Fluka) was poured into a reaction flask with vegetal oil as a dispersion media at room temperature. By stirring the mixtures of these immiscible liquids, granules of 20–200 µm diameter could easily be produced. The resultant beads were filtered off, washed in acetone, and dried in air. The powder beads were then calcined at 200 °C to burn off the gelatin.

Plasma Deposition

Acrylic acid (anhydrous, 99%, cat. no. 147230, Aldrich) and octa-1,7-diene (98%, cat. no. 02501, Aldrich) were used as supplied. Commercial HA powders of 5 µm (Captal 60-5) and 45 µm (Captal 60-45) particle size were ordered from Plasma-Biotal. These commercial HAs and the sol-gel synthesized HA (particle size of 80 µm) were used as substrates for the plasma deposition assays. Acrylic acid was copolymerized with octa-1,7-diene as crosslinker The octadiene/acrylic acid ratio was fixed as 3:1, according to our experience in plasma codeposition of cross-linker/acrylic monomers.

Plasma Reactors

As already mentioned, two different types of plasma reactors were used. They were a downstream reactor in which the sample is located under the plasma generation zone, and a fluidized bed, where the powders are fluidized into the plasma region.

Downstream Reactor

As presented in Figure 1, the reactor is composed of three different glass parts. The central 10 cm wide glass tube (1) is where the plasma is generated by means of a copper coil (4), which is coupled to the plasma generator (8). The generator is inductively coupled through the match box (7) to the coil, which is composed of eight turns of an 8 mm copper tube. The lower round flask is where the powders are located for their modification (2). In order to have a good reproducibility and homogeneous treatment a magnetic stirrer is introduced in the powder container (11). The upper round flask is connected to the vacuum system that includes a double cold trap and the vacuum pump. A pirani gauge is used to measure the pressure inside the reactor (6). The plasma gas goes into the reactor (5) together with argon when necessary.

Fluidized Bed Reactor

The scheme shown in Figure 2 is representative of this type of reactor. The central part is a glass tube (30 mm wide). The
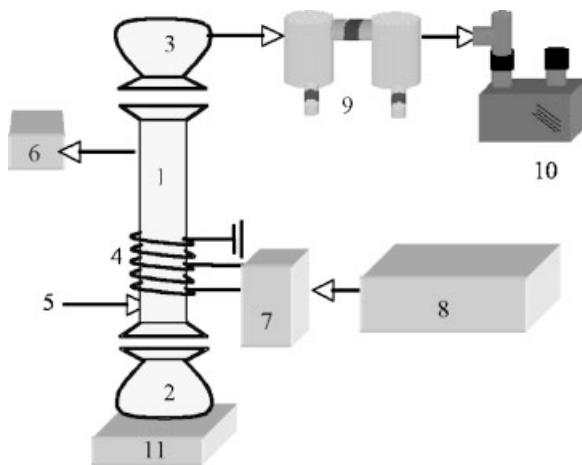

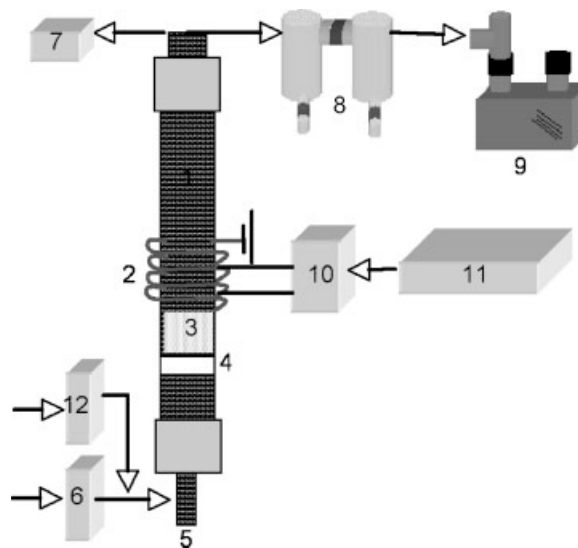Figure 1.   Downstream plasma reactor for powder modification.

Figure 2.   Fluidized bed reactor for powder modification.

sample is supported on a porous plate, the size of the porosity being determinant for its performance as will be shown later on. The copper coil in this case has a diameter of 2 mm and nine turns. The tube is connected at the upper part to the pressure gauge on one side and the cold trap and the vacuum pump on the other. A special design of the cold trap (8) allows prevention of the entrance of the powder in case this escapes from the reactor. The matching system is the same as that used in the reactor explained above. A flow of argon (6) is mixed with the monomer coming from an evaporation unit (12) and used to fluidize the material.

Reactors Set-Up

Both the downstream reactor and the fluidized bed were optimized in order to obtain the best results during modification. The main parameters that have been taken into account are the inlet position of the reactive gas in the downstream model and the position of the sample, hole size of the porous support, and flow of fluidization in the fluidization reactor.

Downstream Reactor

In order to promote the higher deposition activity near to the sample region the following experiment was performed. A string containing glasses at different heights was hung from the top to the bottom of the reactor (Figure 3). Afterwards, a deposition with pyrrole was carried out. The conditions used were: 0.4 mbar, 30 W, and 30 min.

The intensity degree of the yellow color of the plasma-deposited pyrrole film onto the small glass pieces allowed the most reactive zone in the reactor to be rapidly defined, without the need to further analyze the samples. The more intense the color, the greater the reaction between the plasma and the organic feed. The experiment was performed at three different positions for the monomer inlet. The results presented in Figure 3 show that when the monomer was introduced at
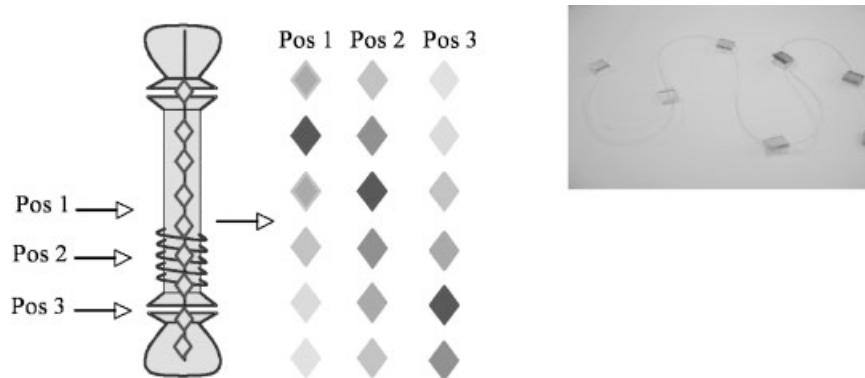
Figure 3. Glasses are located at different positions to determine the maximum deposition zones.

position 3 just below the copper coil the maximum activity was obtained at the powder treatment zone. It is clear that changing monomer and flow rate conditions would not lead to exactly the same deposition results. For this reason a rough method (changing in color) has been chosen to establish the inlet position that gives maximum plasma activity. Although the intensity would probably change under other conditions, a higher activity in the powder-containing vessel would be expected when using inlet position 3 than when using the two other inlets. As a result this position was used for the experiments performed on HA modification.

Fluidized Bed Reactor

In this case the number of parameters to be taken into account was higher. First of all the size of the porous plate supporting the powder had to be selected in order to achieve a good fluidization, which allowed the particles to circulate in the plasma zone. Table 1 shows the pore size that was successfully used to fluidize different particle sizes.

In order to check a good particle movement inside the reactor, particles that had the same size (90 µm) and density but differed in color (white and black) were introduced into the reactor. It was found that after the particles were completely mixed a homogeneous color was obtained.

A very important parameter closely related to the one described above is the flow introduced in the reactor in order to fluidize the powder. This parameter it is also described in Table 1.

Last but not least, the distance between the porous plate and the copper coil also had to be optimized. A position where only the upper part of the fluidized powder was in contact with the

plasma was determined after placing the porous plate in different positions and fluidizing the powder with an argon plasma under the conditions described in Table 1. For this system, it was established that an optimal position was located 35 mm below the end of the copper coil when the argon flow was 75 mL $\cdot$ min^{-1} (particle size 250 µm) and 32 mm when the fluidizing argon flow was 20 mL $\cdot$ min^{-1} (particle size of 20 µm). In both cases a continuous RF power of 20 W was used.

In Table 2 both the advantages and drawbacks of these two different types of reactors have been summarized.

For the downstream reactor, all depositions were performed under continuous plasma. Different settings of the RF power were tested (10, 25, 50, and 100 W), and different deposition times were also tried (10, 30, and 60 min). The monomer was preheated to reach the desired deposition pressure. The monomer flow rate was set so that the pressure within the reactor was 0.2 mbar.

For the fluidized bed reactor, the 90 µm commercial HA was used for fluidized bed experiments, as stated previously, for its homogeneity in terms of particle size. Fluidization was achieved with 20 mL $\cdot$ min^{-1} of argon. Acid acrylic/octa-1,7-diene were fed to the reactor within the fluidized argon in a ratio of 100/1 (Ar/monomers). Different settings of the RF power were tested (10, 25, 50, and 100 W), and different deposition times were also tried (5, 15, and 30 min). The deposition time was reduced in comparison to the times used with the downstream reactor because with the fluidized bed reactor the HA powder is in contact with the plasma, and a higher deposition ratio is expected.

Calcium Release from Modified HA Immersed in Simulated Body Fluid (SBF)

In order to determine the effect of the plasma coating on the interaction between the HA material and SBF, the calcium release of the different HA samples immersed in SBF was analyzed with time. Briefly, the SBF solution (142×10^{-3} M Na$^+$, 5×10^{-3} M K$^+$, 1.5×10^{-3} M Mg^{2+}, 2.5×10^{-3} M Ca^{2+}, 125×10^{-3} M Cl$^-$, 27×10^{-3} M HCO$_3^-$, 1.0×10^{-3} M HPO$_4^{2-}$, and 0.5×10^{-3} M SO$_4^{2-}$) was prepared by dissolution of high purity reagents in distilled water, and buffered at pH 7.4 with

Table 1. Flow used in the fluidized bed reactor regarding the powder size of the HA.

Particle size	Support porous size	Fluidization flow Ar
µm		mL $\cdot$ min^{-1}
250	type 3	70
90	type 2	25

Table 2. Advantages and disadvantages of both the downstream and fluidized bed reactor for HA powder modification.

Reactor	Advantages	Disadvantages
Downstream	Easier set up	Higher reactor volume
	More handy	Worse homogeneity
Fluidized bed	Very good homogeneity	More difficult set up
	Lower reactor volume for the same amount of sample	More difficult to manipulate

50×10^{-3} M trishydroxymethylaminoethane and 1 M hydrochloric acid. The experiments were carried out by soaking the modified HA powders in SBF and incubating them at 37 °C for periods up to 20 d. After different soaking periods, the samples were removed from the fluid and the calcium concentration of the solution was measured by atomic absorption spectrometry. The formation of apatite-like layers on the HA surface was determined by glancing angle incidence X-ray diffraction (GAXRD).

Particle Size Determination

A Saturrn Digisizer laser particle analyzer was used for particle size determinations (Micromeritics, GA, USA). The dispersing media was water. A run of three experiments for each sample was performed with sonication.

Results and Discussion

Sol-Gel Synthesis of HA

The sol-gel method presented here has previously been studied in our group. The experimental conditions of phosphorous precursor hydrolysis, aging time of the sol, gelation, and thermal treatment of the gel have been optimized using different phosphorous and calcium precursors.

It has been proven that the H_2O/P precursor ratio used during the hydrolysis of the P precursor determines the hydrolysis kinetics. A H_2O/P precursor molar ratio between 3 and 5 is the appropriate value to further promote the formation of HA and avoid the formation of secondary phases such as tricalcium phosphate (TCP). In addition, aging times higher than 20 h are needed to allow complete reaction of Ca and P precursors. All the combinations of precursors lead to the formation of HA between 300 and 400 °C (Table 3). HA formation is first seen at 300 °C (for an annealing time of 4 h) when using triethyl phosphite and calcium nitrate or calcium acetate. Nevertheless, the calcium acetate precursor promotes the formation of less crystalline HA in terms of peak sharpness than that formed using calcium nitrate at the same annealing temperature. In addition, TCP is developed at relatively low temperatures (600 °C) when calcium acetate is used as precursor, which suggests that this crystalline phase and the HA may be evolved from different initial amorphous Ca–P intermediates that could readily coexist in the dried gel. This system allows the formation of biphasic HA/TCP ceramics that are known to have good bioresorbability *in vivo*. On the other hand, the use of calcium nitrate results in the formation of pure HA from 300 to 1 000 °C (Table 3).

The use of triethyl phosphate as precursor always yields the formation of HA accompanied by impurities such as calcium carbonate, calcium hydroxide, and calcium oxide (Table 3), which suggests either an incomplete reaction of calcium acetate, which decomposes to calcium carbonate and subsequently to calcium oxide at high temperatures, or the incorporation of carbon dioxide from the air, which reacts with the calcium in the solution. The carbon dioxide incorporation is explained by the longer time periods needed to complete the hydrolysis of the triethyl phosphate.

Furthermore, the temperature and the time of the thermal treatment influences the crystallinity and the crystallite size of the HA. This can also be controlled to fabricate tailored HA. The crystallite size can influence the capacity of the HA to be resorbed by the body and its bioactivity. HA crystals in bone are plate-like apatite crystals and occur within the discrete spaces within the collagen fibrils, thereby limiting the possible primary growth of the mineral

Table 3. Minimum temperature of HA formation as a function of the phosphorous and calcium precursors used in the sol-gel synthesis. The HA precursor gels were submitted to different temperatures ranging from 100 to 1 000 °C for 4 h. Crystalline phases were observed by XRD analysis.

Phosphorous precursor	Calcium precursor	Annealing temperature	Crystalline phases
		°C	
Triethyl phosphite	Calcium nitrate	300	Pure HA stable from 300 to 1 000 °C
Triethyl phosphite	Calcium acetate	300	Pure HA, but TCP was developed at 600 °C
Triethyl phosphate	Calcium nitrate	300	HA accompanied by $CaCO_3$, $Ca(OH)_2$, and CaO
Triethyl phosphate	Calcium acetate	400	HA always accompanied by calcium carbonate

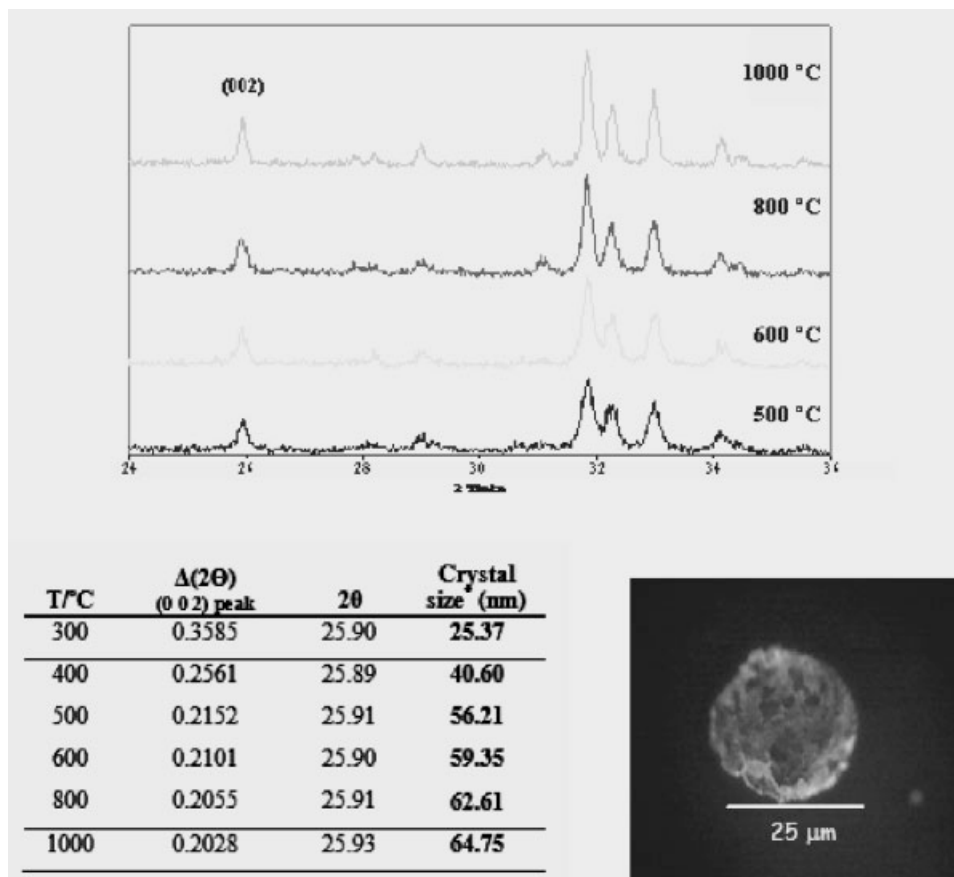| T/°C	Δ(2Θ) (0 0 2) peak	2θ	Crystal size (nm)
300	0.3585	25.90	25.37
400	0.2561	25.89	40.60
500	0.2152	25.91	56.21
600	0.2101	25.90	59.35
800	0.2055	25.91	62.61
1000	0.2028	25.93	64.75

Figure 4. A) XRD patterns of HA obtained using triethyl phosphite and calcium nitrate precursors after different annealing temperatures for 4 h. B) Crystal size of the HA synthesized by the sol-gel method as a function of the thermal treatment. *The crystallite size has been determined according to Equation (1), see text for details. C) Optical microscope picture of spherical HA particles.

crystals, and forcing the crystals to be discrete and discontinuous. They grow with a specific crystalline orientation - the c axes of the crystals are roughly parallel to the long axes of the collagen fibrils. The average lengths and widths of the plates are 50×25 nm^2 and crystal thickness is $2-3$ nm.[21,22] Hence, the crystal size of the synthesized HA for the triethyl phosphite/calcium nitrate sol-gel system has been determined by measuring the peak width at half-maximum intensity of the (002) reflection of the XRD patterns according to the Scherrer equation (Equation (1)):

$$\text{FWHM} = \frac{0.9\lambda}{L_c \cos(\theta_{002})} \quad (1)$$

where FWHM is the peak width at half-maximum intensity of the reflection (002) corrected to minimize the width error because of the instrument, λ is the wavelength for Cu K$_\alpha$ ($\lambda = 1.5406$ Å), and L_c is the crystal size in nm.

As shown in Figure 4A, HA crystals similar in size to that of bone are obtained with the triethyl phosphite/calcium nitrate sol-gel system with an annealing treatment of 4 h at $400-500\,^\circ$C (crystal size between $40.60-56.21$ nm). In

addition, spherical HA particles with controlled size have been fabricated in order to allow better fluidization in the fluidized bed reactor (Figure 4C).

Surface Modification of HA Particles by Plasma Deposition

The downstream reactor has been used to modify the surface of HA powder using the home-made spherical HA. Alternately, the commercial HA is used to optimize the conditions of the fluidized bed reactor because of their higher particle size homogeneity. Some preliminary results obtained with each type of reactor are presented.

Downstream Reactor Results

The biocompatibility of polymeric films of acrylic acid obtained by plasma has been well studied in previous papers.[23,24] However, the stability of the polymeric deposited films from this monomer versus aqueous media has been proven to be very low and in most cases the film is dissolved. For this reason, octa-1,7-diene monomer has

been used as a comonomer together with acrylic acid in order to enhance the film resistance to aqueous media without loosing the carboxylic functionalities.

HA particles have been modified with acrylic acid and acrylic acid-*co*-octa-1,7-diene (4/3) by downstream plasma polymerization. Different settings of the RF power (10, 25, 50, and 100 W) and deposition times have been used (10, 30, and 60 min). The monomer flow rate is set so that the pressure within the reactor is 0.2 mbar. Deposition times of 30 min at 25 W of RF power result in the highest amount of carboxylic functionalities on the HA surface, as determined by a conventional back-titration method. In brief, samples have been treated with an excess of 0.2 N NaOH solution for 2 h. The resultant solution is titrated with 0.4 N HCl solution. The carboxylic group content is expressed as moles of –COOH.[27]

Bioactive ceramics and glass ceramics induce the formation of a biological-like apatite layer when immersed in SBF.[25,26] This process takes place by dissolution–precipitation and ion interchange mechanisms between the material and the SBF, and indicates the bioactivity degree of the material. In order to determine the effect of the plasma coating on the interaction between the HA material and the SBF, the calcium release of the different HA samples immersed in SBF has been analyzed with time. The three samples initially experience an elevated calcium release to the SBF at day 1 of immersion (Figure 5A). After that, the amount of calcium in the SBF highly decreases until day 3, and at day 16 the calcium concentration reaches a stable value (Figure 5A). This calcium decrease suggests the formation of a biological apatite-like layer on the surface of the HA samples. HA modified with acrylic acid exhibits the greatest calcium dissolution, this is likely a result of the hydrophilic nature of the acrylic acid plasma coating, which promotes a higher interaction with the aqueous media. In addition, the acidic nature of the acrylic acid deposited film

produces a local acidic pH on the surface of the HA that also helps its dissolution. This local acidic pH could also explain the lower precipitation achieved at day 3 in comparison with the other two samples. On the other hand, the addition of a crosslinker such as octa-1,7-diene decreases the calcium release during the first day in contact with the SBF, which may be attributable to the higher reticulation degree of the deposited film. However, the precipitation degree achieved during the following two days is similar to that of non-modified HA.

Furthermore, acrylic acid and acrylic acid-*co*-octa-1,7-diene-modified HA powders are demonstrated to remain in suspension (self-dispersing capacity) in contact with an aqueous media (Figure 5B). This self-dispersing property could be controlled by adjusting the acrylic acid/octadiene proportion in the plasma coatings, to always maintain a compromise between the content of carboxylic groups and the degree of reticulation in order to allow the interaction of the ceramic with the SBF. In a previous work, advantage was taken of this self-dispersing property in order to develop a new composite composed of HA and a synthetic organic matrix, which was demonstrated to be a promising biomaterial for bone tissue engineering.[27]

Fluidized Bed Reactor Results

The 90 µm commercial HA is used for fluidized bed experiments, as stated before, for its homogeneity in terms of particle size. Fluidization is achieved with $20\ mL \cdot min^{-1}$ of argon. Acid acrylic/octa-1,7-diene are fed to the reactor within the fluidized argon in a ratio of 100/1 (Ar/monomers). As described in the experimental part, different settings of the RF power have been tested (10, 25, 50 W), and different deposition times have also been tried (5, 15, and 30 min). Samples have been characterized in terms of particle size modification, amount of carboxylic groups on

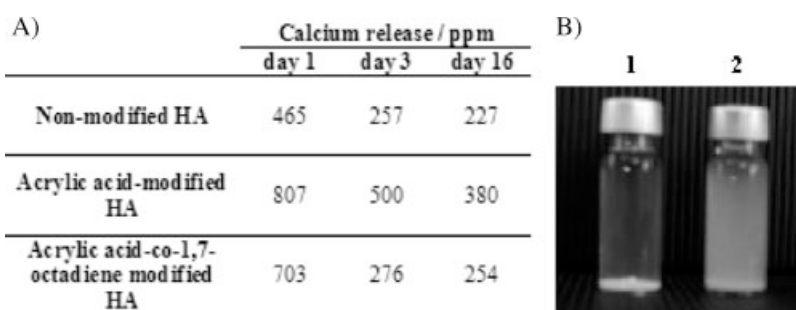| A)	Calcium release / ppm		
	day 1	day 3	day 16
Non-modified HA	465	257	227
Acrylic acid-modified HA	807	500	380
Acrylic acid-co-1,7-octadiene modified HA	703	276	254

Figure 5. A) Calcium release from plasma-modified HA samples using a downstream reactor with acrylic acid and acrylic acid/octadiene 4/3 (25 W, 30 min) at days 1, 3, and 16 after immersion in SBF. A non-modified HA sample was assayed as a control. The initial calcium concentration in the SBF was 100 ppm. B) Picture showing an aqueous suspension of 1) non-modified HA particles and 2) acrylic acid-modified HA particles. Plasma-modified HA particles with acrylic acid and acrylic acid-*co*-octa-1,7-diene presented a three-fold increase in their sedimentation time compared with the non-modified HA particles.

Table 4. Particle size modification (μm) after fluidized bed plasma reactor treatment of commercial HA samples.

Deposition time	RF Power[a]		
min	W		
	10	25	50
5	95	93	96
15	97	89	100
30	93	96	89

[a] The results are the mean of three determinations. The mean standard deviation for the whole determinations was 10 μm.

the surface, and water dispersibility. No experiments on calcium release have been performed.

The results of particle size for the different treatments are presented in Table 4. The results reveal that the plasma treatment does not affect the particle size significantly even after 30 min deposition time. However, the amount of carboxylic functionality is highly dependent both on power and treatment time. The results obtained show that the maximum carboxylic functionalization (2.3 moles) is achieved at 5 min and 25 W. Higher times lead to a drastic reduction in surface functionality, especially for 30 min (25 W) where the amount of carboxylic groups measured is 1.2 moles. An RF of 50 W provokes greater destruction of the acrylic monomer with little carboxylic group retention (1.0 moles at 5 min, 0.8 at 30 min).

It is clear that the fluidized bed reactor shows better efficiency in plasma deposition of the acrylic acid with shorter times and lower power requirements than the downstream reactor. Nevertheless, further experiments should be performed to optimize the plasma conditions for this reactor.

Water Dispersability

The water dispersibility of the HA (90 μm commercial HA) treated for 5 min at 25 W in the fluidized bed reactor has been determined and compared with bare 90 μm HA and home-made HA treated with the downstream reactor (around 20 μm particle size). The results are presented in Table 5. As it can be seen, the plasma treatment of commercial HA leads to a good self-dispersing behavior,

Table 5. Sedimentation times in water for HA treated with acrylic acid/octa-1,7-diene.

HA sample	Self dispersing behavior
	min
Bare HA (90 μm)	2
HA treated in fluidized bed reactor (90 μm)	25
HA treated in downstream reactor (20 μm)	30

although the particle size is much larger than the home-made HA. The preliminary results seem to indicate that the use of the fluidized bed reactor can lead to a reduction in deposition time of at least three times in comparison with the downstream reactor.

Conclusion

Two types of reactors have been set up for the modification of HA powders with acrylic acid by plasma polymerization. The films cross-linked with octa-1,7-diene have shown good stability in the presence of water. Moreover, modification of the HA surface has lead to a dramatic increase in its water dispersability. The results obtained also show the possibility of using such a treatment to tune the calcium release of HA powder in tissue engineering applications.

[1] M. Jarcho, *Dent. Clin. North Am.* **1986**, *30*, 25.
[2] L. L. Hench, J. Wilson, "*An Introduction to Bioceramics*", Vol. 1, World Scientific, Singapore 1993.
[3] V. S. Komlev, S. M. Barinov, E. Girardin, S. Oscarsson, Å. Rosengren, F. Rustichelli, V. P. Orlovskii, *Sci. Technol. Adv. Mater.* **2003**, *4*, 503.
[4] S. Ozawa, S. Kasugai, *Biomaterials* **1996**, *17*, 23.
[5] K. Anselme, *Biomaterials* **2000**, *21*, 667.
[6] D. D. Deligianni, N. D. Katsala, P. G. Koutsoukos, Y. F. Missirlis, *Biomaterials* **2001**, *22*, 87.
[7] C. J. Watson, D. Tinsley, A. R. Ogden, J. L. Russel, S. Mulay, E. M. Davidson, *Br. Dent. J.* **1999**, *187*, 90.
[8] M. L. Steen, W. C. Flory, N. E. Capps, E. R. Fisher, *Chem. Mater.* **2001**, *13*, 2749.
[9] E. Vidal-Escales, N. Agullo, S. Borros, W. J. Van Ooij, *Rubber World* **2003**, *228*, 21.
[10] M. Tatoulian, F. Bretagnol, F. Arefi-Khonsari, L. Amouroux, O. Bouloussa, *Plasma Process. Polym.* **2005**, *2*, 38.
[11] S. H. Jung, S. H. Park, D. H. Lee, S. D. Kim, *Polym. Bull.* **2001**, *47*, 199.
[12] S. J. Park, J. S. Kim, *J. Colloid Interface Sci.* **2001**, *244*, 336.
[13] T. Shirasaki, F. Moguet, L. Lozano, A. Tressaud, G. Nanse, E. Papirer, *Carbon* **1999**, *37*, 1891.
[14] P. Favia, N. De Vietro, R. Di Mundo, F. Fracassi, R. d'Agostino, *Plasma Process. Polym.* **2006**, *3*, 66.
[15] D. Shi, P. He, J. Lian, L. Wang, W. J. Van Ooij, *J. Mater. Res.* **2002**, *17*, 2555.
[16] J. Clotet, N. Tricás, N. Agulló, S. Borrós, poster presented at Kautschuk Herbst Kolloquium November 2004 Hannover, Germany.
[17] F. Bretagnol, M. Tatoulian, F. Arefi-Khonsari, G. Lorang, J. Amouroux, *React. Funct. Polym.* **2004**, *61*, 221.
[18] J. B. Leroy, N. Fatah, B. Mutel, J. Grimblot, *Plasmas Polym.* **2003**, *8*, 2003.
[19] G. Akovali, I. Ulkem, *Polymer* **1999**, *40*, 7417.

[20] D.-M. Liu, T. Troczynski, W. J. Tseng, *Biomaterials* **2001**, *22*, 1721.

[21] V. Ziv, S. Weiner, *Conn. Tissue Res.* **1994**, *30*, 165.

[22] W. J. Landis, *Bone* **1995**, *16*, 533.

[23] L. J. Ward, W. C. E. Schofield, J. P. S. Badyal, A. J. Goodwin, P. J. Merlin, *Chem. Mater.* **2003**, *15*, 1466.

[24] S. Fraser, R. D. Short, D. Barton, J. W. Bradley, *J. Phys. Chem. B* **2002**, *106*, 5596.

[25] L. L. Hench, ''Bioactive Ceramics: Theory and Clinical Applications'', in: *Bioceramics 7*, O. H. Andersson, A. Yli-Urpo, Eds., Butterworth-Heinemann Ltd., Oxford, England 1994, pp. 3–14.

[26] H.-M. Kim, T. Himeno, T. Kokubo, T. Nakamura, *Biomaterials* **2005**, *26*, 4366.

[27] E. Garreta, D. Gasset, C. Semino, S. Borrós, *Biomol. Eng.* **2006**, doi: 10.1016/j.bioeng.2006.05.017.